Enhanced Friction and Adhesion with Biologically Inspired Fiber Arrays

Carmel Majidi

Electrical Engineering and Computer Sciences
University of California at Berkeley

Technical Report No. UCB/EECS-2007-55
http://www.eecs.berkeley.edu/Pubs/TechRpts/2007/EECS-2007-55.html

May 15, 2007

Enhanced Friction and Adhesion with Biologically Inspired Fiber Arrays

by

Carmel Shamim Majidi

B.S. (Cornell University) 2001
M.S. (University of California, Berkeley) 2004

A thesis submitted in partial satisfaction
of the requirements for the degree of

Doctor of Philosophy

in

Engineering - Electrical Engineering and Computer Science

in the

GRADUATE DIVISION

of the

UNIVERSITY OF CALIFORNIA, BERKELEY

Committee in charge:

Professor Ronald S. Fearing, Chair
Professor Kyriakos Komvopoulos
Professor Ali Javey

Spring 2007

The thesis of Carmel Shamim Majidi is approved.

Chair	Date
	Date
	Date

University of California, Berkeley

Spring 2007

Enhanced Friction and Adhesion with Biologically Inspired Fiber Arrays

by

Carmel Shamim Majidi

Abstract

Enhanced Friction and Adhesion with Biologically Inspired Fiber Arrays

by

Carmel Shamim Majidi

Doctor of Philosophy in Engineering - Electrical Engineering and Computer Science

University of California, Berkeley

Professor Ronald S. Fearing, Chair

Controlling surface forces through nano/microstructure represents an important advancement in tribology. Primarily it suggests the possibility of fabricating adhesive and friction pads from a vast range of materials and processing methods, hence allowing for the production of tribological surfaces that are cheap, bio-compatible, durable, temperature resistant, and self-cleaning. Current research in this area draws inspiration from gecko lizards, which achieve rapid wall-climbing with arrays of keratinous, micron-sized fibers. This work explores the central role of the microfiber array in gecko wall-climbing and applies these insights to the development of adhesive and ultra-high friction surfaces from otherwise non-adhesive, low friction materials.

Professor Ronald S. Fearing
Thesis Committee Chair

Dedicated to my parents, Behnam Majidi and Azar Parvizi-Majidi.

Contents

Contents ii

List of Figures vi

List of Tables ix

Acknowledgements x

I Introduction and Background 1

1 Introduction 2

1.1 Overview of Gecko Adhesion 4

1.2 Introduction to Synthetic Fiber Arrays 5

1.3 Work of Adhesion 7

1.4 Contributions 9

2 Previous Work 11

2.1 Study of Natural Gecko Adhesion 11

2.2 Attempts at Synthetic Gecko Adhesion 13

II Natural Microfiber Array 15

3 Elastic Modulus of Gecko Setae 16

3.1 Experimental Overview 17

3.2 Theory 18

3.2.1 Kinematics 18

3.2.2 Constitutive Equations . . . 19
3.2.3 Linear and Angular Momentum Balance . . . 20
3.2.4 Analysis . . . 21
3.3 Results . . . 23

4 Effective Modulus of the Setal Array **24**
4.1 Elastic Rod Model . . . 25
4.2 Bending with Friction at the Tip . . . 27
4.3 Results . . . 29

III Synthetic Nano/Microfiber Arrays **31**

5 Adhesion of Nanofibers through Side Contact **32**
5.1 Overview of Elastica Theory . . . 33
5.1.1 Kinematics . . . 33
5.1.2 Governing Equations . . . 34
5.2 Side Contact . . . 35
5.2.1 Preliminaries . . . 35
5.2.2 Lagrangian Density . . . 36
5.2.3 Energy of Adhesion Per Contact Length, ω . . . 37
5.2.4 Natural Boundary Condition . . . 38
5.2.5 Solution . . . 39
5.2.6 Peel Strength . . . 41
5.3 Side Contact with Lateral Constraint . . . 42
5.3.1 Isoperimetric Constraint . . . 43
5.3.2 Governing Equations . . . 44
5.3.3 Peel Strength . . . 44
5.4 Adhesion Coefficient . . . 45
5.5 Comparison with Experimental Measurement . . . 46
5.6 Design Principles for Side Contact . . . 47

6 Ultrahigh Friction with Microfibers **51**
6.1 Experimental Work . . . 52
6.1.1 Fabrication . . . 52

6.1.2 Testing Procedure . . . 55
6.1.3 Results . . . 55
6.2 Theory of VAMF Friction . . . 56
6.2.1 Array Compliance . . . 58
6.2.2 Coefficient of Friction, $\hat{\mu}$ . . . 59
6.3 Comparison of Theoretical and Experimental Results . . . 60
6.4 Concluding Remarks . . . 62

7 Adhesion with Curved Microfibers 63
7.1 Biological Inspiration . . . 64
7.2 Experimental Work . . . 65
7.3 Tip-Substrate Interaction . . . 67
7.4 Stick-Slip Model . . . 69
7.4.1 Stick Phase . . . 70
7.4.2 Slip Phase . . . 72
7.4.3 Analysis . . . 73
7.5 Slip Model . . . 74
7.6 Results . . . 78
7.7 Design Maps . . . 79
7.7.1 Analysis . . . 81
7.7.2 Results . . . 82
7.8 Concluding Remarks . . . 86

8 Proposed Design for Permanent Adhesion 88
8.1 System Overview . . . 89
8.2 Governing Equations . . . 90
8.2.1 Kinematics . . . 92
8.2.2 Stress Tensors and Constitutive Law . . . 93
8.2.3 Membrane Approximation . . . 95
8.2.4 Variational Principles . . . 95
8.3 Application to Normal Pull-off . . . 97
8.3.1 General Solution at Equilibrium . . . 98
8.3.2 Boundary Conditions . . . 99
8.4 Shaft Rotation . . . 101

8.4.1 Upper Bound . . . 101
8.4.2 Lower Bound . . . 105
8.4.3 Approximate Solution at Equilibrium . . . 106
8.5 Numerical Results and Discussion . . . 108
8.5.1 Examples . . . 109
8.6 Concluding Remarks . . . 111

IV Conclusion **112**

9 Conclusion **113**
9.1 Overview of Contributions . . . 113
9.1.1 Natural Setal Arrays . . . 113
9.1.2 Side Contact with VANF Arrays . . . 114
9.1.3 Ultrahigh Friction with Microfiber Arrays . . . 115
9.1.4 Shear Adhesion with Curved Microfibers . . . 116
9.1.5 Permanent Adhesion with Spatulae . . . 117
9.2 Applications . . . 117
9.3 Future Work . . . 119

Bibliography **121**
References . . . 121

List of Figures

1.1 U.S. quarter suspended on an 82 degree glass incline with an array of 20 micron long, 0.6 micron diameter, polypropylene fibers (inset). From [67]. . 3

1.2 Images of the hierarchical system of the tokay gecko. From top left: gecko foot, lamellar plates, setal stalks, spatular branches, spatular plates. From [9], [36], and [61]. 5

3.1 Illustration of setal preparation for resonance testing. 17

3.2 Kinematic and free body diagrams of setal stalk of length L and spherical bead of radius c and mass m. 18

3.3 Time plots of $z_1 = \theta_L$ and $z_3 = x_L$. 21

3.4 Plot of E (in GPa) versus ω_1 (in rad/sec) for $L = 100\,um$, $R = 2\,um$, $c = 125\,um$, $g = 9.81\,m/s^2$ and $\rho = 2200\,kg/m^3$. 22

4.1 Force-displacement relationship of an elastic rod for $L = 100$ μm, $R = 2$ μm, and $E = 1.5$ GPa. 26

4.2 Tip subject to shear load V; $L = 100$ μm, $R = 2$ μm, $E = 1.5$ GPa, and $\phi = 45^o$; (solid) $V = 0$, (dashed) $V = \mu F$, (dash-dot) $V = -\mu F$. 26

4.3 Illustration of various loading conditions for setal array brought in contact with a fixed PTFE substrate. 28

5.1 Deformation of an elastic fiber, clamped vertically at its base, making contact with an adhering substrate over a length $L - \gamma$. 36

5.2 Peel strength of fiber in side contact; (solid) exact solution, (dashed) approximation valid for large $\omega L^2/EI$. 42

5.3 Loading cycle and qualitative fiber shapes for a fiber completely clamped to a laterally unconstrained and laterally constrained support. (a) Initial configuration (b) Fiber tip at angle $\pi/2$, side contact begins, tip no longer slides relative to opposing substrate (c) Maximum value of preload F_0 (d) Preload relaxed to a final load F, which can be negative. 49

5.4 Peel strength of fiber in side contact with lateral constraint. 50

5.5 Bond strength for optimally packed, non-clumping VANF array (N/cm^2); $W_{\text{ad}} = 30$ mJ/m^2 and $\nu = 1/3$. 50

6.1 Stacking order for fabrication of polypropylene VAMF array. 53

6.2 SEM of an array of 20 μm long, 0.6 μm diameter polypropylene fibers etched from a polycarbonate membrane; scale bar represents 10 μm. 53

6.3 Pulley apparatus for measuring coefficient of friction of a VAMF array. . . . 54

6.4 Plot of normal pressure versus shear resistance for polypropylene fiber arrays and controls; (▲) radius $R = 0.3$ μm, (•) $R = 0.6$ μm, (■) $R = 2.5$ μm, (○) unprocessed control, (□) processed control; (left) loading area = 1.27 cm^2, sample size = 15; (right) loading area = 0.033 cm^2, sample size = 5; error bars represent one standard deviation in the data; solid lines represent theoretical predictions from equations (6.6), (6.7), and (6.12) for $R_t = 3R$. . 57

6.5 Mechanical response of $R = 0.3\mu$m fiber array indented by a spherical probe (radius = 5.17 cm); greater compliance at low Δ may be a result of fiber sparsity near the top of the array due to length variation; (−−) theoretical predictions based on ideal column buckling for various buckling modes; arrows indicate loading direction. 58

7.1 SEM image of the setal array for *Anolis Equestris*. 64

7.2 SEM image of curved, 0.4 μm radius, 20 μm polypropylene fibers. Estimated density $D = 50\times10^6\text{cm}^{-2}$. 65

7.3 Force response to indentation with 5.17 cm sphere. Curved polypropylene fibers of radius, $R = 0.4$ μm and length $L = 20$ μm. Estimated density $D = 50\times10^6\text{cm}^{-2}$ 66

7.4 Free body diagram of curved fiber in stick and slip phases. 68

7.5 Force response during loading; gray line represents the detachment strength during slip, αp; $F > 0$ corresponds to tension; (top) stick-slip model, detachment occurs in circled region; (bottom) elastica model with slip only; $R = 0.4$ μm, $R_t = R$, $L = 20$ μm, $\rho = L$, E = 1 GPa, $\nu = 0.4$, $W_{ad} = 30$ mJ m^{-2}, $\tau = 10$ MPa and $\alpha = 0.75$. 75

7.6 Detachment resistance of an array as a function of substrate roughness; (top) stick-slip model; (bottom) elastica model with slip only; $R = 0.4$ μm, $R_t = R$, $L = 20$ μm, $\rho = L$, E = 1 GPa, $\nu = 0.4$, $W_{ad} = 30$ mJ m^{-2}, $\tau = 10$ MPa and $\alpha = 0.75$, $D = 50\times10^6$ cm^2. 76

7.7 Force response to indentation of 5.17 cm sphere; positive load corresponds to compression; (top) stick-slip model, discontinuity caused by hysteresis in force-displacement relationship (see Figure 7.5(a)); (bottom) elastica model with slip only; $R = 0.4$ μm, $R_t = R$, $L = 20$ μm, $\rho = L$, E = 1 GPa, $\nu = 0.4$, $W_{ad} = 30$ mJ m^{-2}, $\tau = 10$ MPa and $\alpha = 0.75$, $D = 50\times10^6$ cm^2. . . . 77

7.8 Fiber array in contact with a nominally flat surface with uniform roughness. 80

7.9 Bond strength in N/cm^2 for an array of curved fibers: $E = 1$ GPa, $W_{\text{ad}} = 30$ mJ/m^2, $\nu = 0.3$, $\rho = L$, $R_t = R$. Surface has roughness of $z_0 = 1$ μm. (top) normal pull-off, σ; (bottom) shear, s. 83

7.10 Bond strength in N/cm^2 for an array of curved fibers: $E = 1$ GPa, $W_{\text{ad}} = 30$ mJ/m^2, $\nu = 0.3$, $\rho = L$, $R_t = R$. Surface has roughness of $z_0 = 0.1$ μm. (top) normal pull-off, σ; (bottom) shear, s. 84

7.11 Bond strength in N/cm^2 for an array of curved fibers: $E = 1$ GPa, $W_{\text{ad}} = 30$ mJ/m^2, $\nu = 0.3$, $\rho = L$, $R_t = R$. Surface has roughness of $z_0 = 0.01$ μm. (top) normal pull-off, σ; (bottom) shear, s. 85

8.1 Illustration of shaft loaded membrane; (a) reference configuration, (b) delamination under normal translation, (c) delamination under rotation. . . . 89

8.2 Local coordinate system in reference and deformed configurations 91

8.3 Profile of membrane for non-dimensional work of adhesion $W_{ad}/ER = 10^{-5}$, non-dimensional thickness $H/R = 0.01$ and various shaft heights. 99

8.4 Non-dimensional normal load versus normalized shaft height for non-dimensional work of adhesion $W_{ad}/ER = 10^{-5}$ and non-dimensional thickness $H/R = 0.01$. 100

8.5 Delamination of membrane under shaft rotation of $\psi = 0.05$ radians; non-dimensional work of adhesion $W_{ad}/ER = 10^{-5}$ and non-dimensional thickness $H/R = 0.01$. 102

8.6 Plot of delamination zone for non-dimensional work of adhesion $W_{ad}/ER = 10^{-5}$, non-dimensional thickness $H/R = 0.01$, and various angles of rotation. 102

8.7 Plot of energy versus angle of rotation for non-dimensional work of adhesion $W_{ad}/ER = 10^{-5}$ and non-dimensional thickness $H/R = 0.01$. 103

8.8 Plot of non-dimensional moment M/ER^3 versus angle of rotation for non-dimensional work of adhesion $W_{ad}/ER = 10^{-5}$ and non-dimensional thickness $H/R = 0.01$. 104

9.1 Shear adhesion with a MWCNT array [83]; scale bar equals 2 μm. 114

9.2 An array of 20 μm long, 200 nm diameter polypropylene nanofibers suspending a 200 gram weight in pure shear [69]. 115

9.3 Stickybot robot developed at Stanford University [6]. 117

List of Tables

4.1 Elastic modulus of a tokay setal array; ($\hat{E}_{\text{th}}$) theory, ($\hat{E}_{\text{exp}}$) experimental; theoretical predictions based on $L = 100$ μm, $R = 2$ μm, $E = 1.5$ GPa, and $\phi = 45^o$; 30

6.1 Estimated contact areas for polypropylene fiber arrays; ρ is the fiber density, f is the estimated fraction of fibers buckled in the clamped-free mode (K = 1/4). 60

Acknowledgements

I wish to thank my family and friends for their love and support.

In addition, I would like to thank my past and present colleagues in the Biomimetic Milli Systems Laboratory at UC Berkeley: Rick Groff, Stan Baek, Bryan Schubert, Yohei Maeno, Steven Jones, Eric Steltz, Aaron Hoover, Ranjana Sahai, Robert Wood, Srinath Avadhanula, and Fernando Garcia Bermudez. I am also grateful to my collaborators in Chemical Engineering and Integrative Biology: Brian Bush, Anne Peattie, Victor Chan, and Alisyn Nedoma.

Lastly, I wish to thank my professors Oliver O'Reilly, Kyriakos Komvopoulos, and David Steigmann, first-year advisors Roger Howe, Steve Glaser, and Ken Goldberg, research collaborators Bob Full, Nitash Balsara, and Kellar Autumn (Lewis & Clark College), and research advisor Ron Fearing. I am particularly thankful for their continual support and guidance and feel honored for the opportunities I've had to work with and learn from them.

Part I

Introduction and Background

Chapter 1

Introduction

This works presents mechanical principles that govern the friction and adhesion of natural and synthetic gecko fiber arrays. The adhesive systems utilized by gecko lizards for wall climbing are exceptional for their high strength, durability, controllability, and ability to self-clean and have inspired researchers to develop a new class of dry adhesive and high friction surfaces. An example of a recent gecko-inspired surface is shown in Figure 1.1.

The nascent field of gecko-inspired adhesion is part of a larger endeavor to improve the tribological and wetting properties of surfaces with nano/microstructure. The geometry of these structures are based on design principles derived from bulk and interfacial mechanics.

The central role of geometry suggests that adhesive and high friction surfaces can be fabricated from a vast range of materials and processing methods, hence allowing them to be cheap, bio-compatible, wear resistant, temperature resistant, and self-cleaning. In this respect, gecko-inspired fiber arrays present an exciting alternative to traditional pressure sensitive adhesives (PSAs), which are limited to soft polymers (elastic modulus $\leq$ 100 kPa) that lack many important properties such as wear and temperature resistance.

Figure 1.1. U.S. quarter suspended on an 82 degree glass incline with an array of 20 micron long, 0.6 micron diameter, polypropylene fibers (inset). From [67].

1.1 Overview of Gecko Adhesion

The design of fiber arrays is aided by insights into the mechanics of gecko adhesion. This work includes study of key mechanical aspects of the natural microfiber array. Of primary concern are the micron-sized fibers, *setae*, that cover each digit of the gecko. Each setal stalk branches into hundreds of nano-sized fibers, called *spatulae*, which end in thin, terminal flaps. These flaps, sometimes called spatular plates, adhere to the wall through weak surface forces and are responsible for the attachment of the gecko lizard during wall-climbing. The nature of these forces remains a topic of open research, although recent studies have suggested various forms of van der Waals attraction, such as dispersion forces [10] and hydrogen bonding [37]. Lastly, the setal stalks form aligned arrays that are supported by flaps of skin called *lamellae* that protrude from soft sinus tissue. Images of the hierarchical system are presented in Figure 1.2.

Collaborative efforts with scientists in integrative biology reveal that although the gecko adhesive behaves like a soft surface, it is composed of stiff, keratinous material with an elastic modulus of 1.5 GPa. These results are important since they demonstrate that adhesion is possible with materials that are beyond the scope of traditional PSAs.

The elastic properties of an individual seta are determined by resonance testing. The analysis and results of this experiment are presented in Chapter 3. The effective elasticity of an entire setal array is measured directly with *Robotoe*, an automated force sensing apparatus at Lewis & Clark College. A theoretical study of setal deformation under loadings in Robotoe are presented in Chapter 4.

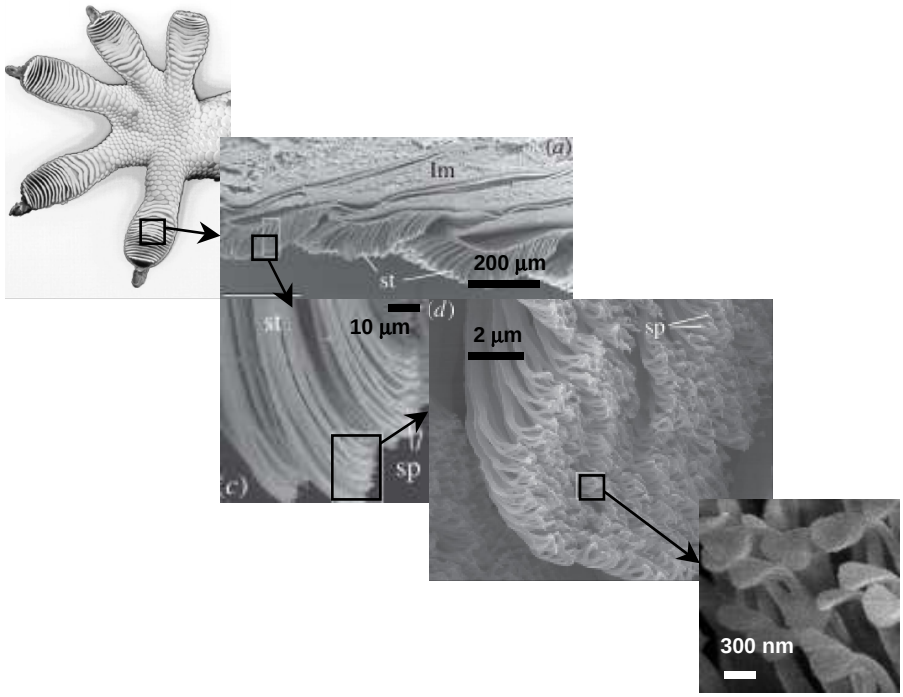

Figure 1.2. Images of the hierarchical system of the tokay gecko. From top left: gecko foot, lamellar plates, setal stalks, spatular branches, spatular plates. From [9], [36], and [61].

1.2 Introduction to Synthetic Fiber Arrays

The remarkable performance of natural setal arrays has encouraged researchers to explore alternatives to PSAs that exhibit many of the useful properties found in gecko adhesion. This work explores designs for dry adhesion and high friction with stiff materials that, like natural setae, have an elastic modulus greater than 1 GPa. Unlike softer materials, such as rubber and low molecular weight polymers, stiff materials have the advantage of wear resistance and represent a wide range of polymers, metals, and ceramics that include materials that are also temperature resistant and biocompatible.

The simplest structure that exhibits adhesion with a stiff material is an array of high-aspect ratio, vertically aligned nanofibers. Unlike gecko setae, these fibers are slender enough to bend over and, under the influence of surface forces, make stable contact with

an opposing substrate along their side. Theoretical models and design principles for side contact are presented in Chapter 5.

Although nanofibers can achieve strong adhesion through side contact, they have the propensity to adhere to their neighbors, forming large clumps. These clumps occur after only a few loading cycles and preclude further adhesion. Theoretical and experimental investigations demonstrate that clumping is a function of fiber geometry, elasticity, surface energy, and spacing [53].

Microfibers have less of a tendency to clump since their elastic restoring forces often exceed the surface forces necessary to adhere to neighbors. This property, however, implies that microfibers are unlikely to adhere to an opposing substrate through side contact. Nonetheless, microfiber arrays can exhibit high friction, with a friction coefficient several orders of magnitude greater than that of the smooth material under pressures ranging from 0 to $\sim$10 kPa. This phenomenon is explained with a fiber buckling model that is experimentally validated for various fiber geometries and loading conditions. Theory, fabrication, and experimental details for high friction microfiber arrays are presented in Chapter 6.

Adhesion with a microfiber array is not possible when the fibers are vertically aligned. This is because vertical microfibers must stretch in order to accommodate displacement under a purely tensile load. While this property does not effect the bond strength of an individual fiber, it greatly inhibits the ability of adjacent fibers to share tensile load when contacting a microrough surface or when the fiber lengths are slightly varied.

Tensile compliance in microfiber arrays is introduced by angling or curving the fibers such that they can bend under tension. This geometry expands the range of configurations that a fiber can support prior to detachment. Theoretical models and design principles for

microfiber adhesion are presented in Chapter 7 along with some preliminary experimental results. Interfacial bonds can be strengthened by terminating each fiber with a *spatula-like* plate. A spatular plate geometry for permanent adhesion is proposed in Chapter 8.

1.3 Work of Adhesion

A critical factor in the friction and adhesion of synthetic fiber arrays is the *work of adhesion*, W_{ad}. This is defined as the work (change in free energy) per unit area necessary to completely separate two initially contacting surfaces [41]. As with natural spatulae, synthetic fibers are assumed to adhere through van der Waals forces. Since van der Waals forces typically act over a very short range ($\sim$ 1 nm), surfaces are regarded as completely separated when they are not in intimate contact.

It is important to distinguish W_{ad} from the *surface energy* γ. Typically, γ is defined as the difference in free energy between unit areas of bulk and surface. For homogenous, isotropic materials, γ is invariant to position or orientation. Let γ^d denote the portion of γ associated with van der Waals force. For distinct media 1 and 2, Fowkes estimates [21]

$$W_{\text{ad}} = 2\sqrt{\gamma_1^d \gamma_2^d}. \tag{1.1}$$

Equation (1.1) applies to ternary interactions: media 1, media 2, and air. In practice, however, surfaces are coated with condensed layers of water, oil, oxides and contaminants that significantly alter W_{ad} [66]. Moreover, (1.1) ignores other contributions to work of adhesion such as plastic or viscoelastic energy dissipation [27] and nanoscale roughness.

A popular method for estimating W_{ad} is to calculate the pull off force F_{ad} of a spherical

probe of known radius R. Following from linear elastic fracture mechanics [44],

$$W_{\text{ad}} = \frac{F_{\text{ad}}}{1.5\pi R}. \tag{1.2}$$

Pull-off measurements performed with a silicon nitride AFM tip (R = 20 to 50 nm) in contact with polypropylene and high density polyethylene correspond to $W_{\text{ad}} = 32$ mJ/m^2 [32].

Alternatively, W_{ad} may be estimated by analyzing the profile of a liquid drop on a smooth substrate. This is known as the *sessile drop* method, and is used to measure W_{ad} for a variety of low and high density polyethylenes on stainless steel [3]. At a temperature of 200^{o}C, W_{ad} was found to range from 22 to 37 mJ/m^2. Since W_{ad} varies with temperature and state, such values provide only a rough estimate for the work of adhesion of solid polymer at room temperature.

According to these measurements, the work of adhesion in air between polymer and crystalline, inorganic surfaces is approximately 30 mJ/m^2. Henceforth this will be assumed as the work of adhesion for polymer on glass. Such a value neglects the effects of roughness and deformation and represents the *true* work of adhesion. Including roughness and deformation leads to an *effective* work of adhesion. For example, polymers that are pressure sensitive adhesives exhibit 1 J/m^2 of adhesion, several orders of magnitude greater than the true work of adhesion for polymers. This enhancement is due to energy dissipations generated by elastic stretching and fibrillation near the crack tip during pull-off. Similarly, microfiber arrays will exhibit an effective work of adhesion other than 30 mJ/m^2, since the area fraction is small and energy is dissipated to bend fibers. Following detachment, an individual fiber cannot transfer its elastic bending energy to promote further crack growth.

In the case of synthetic fiber arrays, the true work of adhesion $W_{\text{ad}} = 30$ mJ/m^2 is used locally to study the contact of individual fiber tips.

1.4 Contributions

This work builds upon previous accomplishments in the fields of natural and synthetic adhesion. Specific contributions are summarized in the list below:

- *Elastic Modulus of Gecko Setae* - The natural frequency of a setal stalk is measured with resonance testing. Dynamical analysis performed on a theoretical model of the system yields a non-linear relationship that maps natural frequency to the elastic modulus of the setal material.

- *Effective Modulus of the Setal Array* - Compliance of the setal array is predicted by studying the deformation of individual setae with an elastica model. These results are compared with experimental measurements obtained by collaborators at Lewis & Clark College.

- *Predictive Model for "Side Contact"* - Utilizing elastica theory and stationary principles, a model is introduced to explain the remarkable adhesion of high-aspect ratio arrays of stiff fibers. Unlike gecko *setal* stalks, these fibers are slender enough to bend over and, under the influence of surface forces, make stable contact with an opposing substrate along their side.

- *Ultra-High Friction Microfiber Arrays* - Microfiber arrays are shown to exhibit a coefficient of friction that is over ten times greater than that of the smooth (unstructured)

material. This phenomenon is explained with a fiber buckling model, which is experimentally validated for various fiber geometries and loading conditions.

- *Adhesion with Curved Microfiber Arrays* - Preliminary results suggest adhesion with arrays of curved microfibers. These designs are based on mechanical insights gained from elastic rod theory and contact mechanics and are inspired by the natural geometry of setae in tokay lizards.

- *Design of Terminal Membranes for Fiber Tip Attachment* - Finite elasticity and stationary principles are employed to demonstrate that normal and shear adhesion are significantly enhanced when fibers are tipped with a center-supported membrane. These structures are proposed for permanent adhesion.

Chapter 2

Previous Work

The exceptional wall-climbing ability of gecko lizards has long been the source of curiosity and scientific attention. Descriptions of the gecko's nanoscopic adhesive system can be found in the popular literature [5], [45]. Experimental measurements have been reported in scientific journals and range from testing on whole animals [39] and isolated lamellae [35] to high resolution force measurements on single setae [7] and spatulae [36].

Parallel to recent investigations on natural gecko adhesion are efforts to create synthetic gecko systems. Such research ranges from whole animal robotic geckos [71] to the synthetic setal and spatular arrays described in this work. Previous work on natural and synthetic gecko adhesion at the setal and spatular levels are discussed in the following two sections.

2.1 Study of Natural Gecko Adhesion

Using novel experimental techniques, researchers have measured surface forces generated by gecko setae and spatulae. Autumn et al. [7] has reported a shear strength of 200 μN for an individual setal stalk of a tokay gecko. This suggests that a tokay gecko can support

130 kilograms when all of its 6.5 million setae are simultaneously engaged! Interestingly, the normal strength of a seta is less than one tenth of its shear strength. Measurements performed on individual spatulae indicate a normal bond strength of about 10 nN [36]. Noting that setae contain several hundred to a thousand spatulae, this result is roughly consistent with the value of 13.6 μN reported by Autumn et al. [7] for the normal component of the pull-off force of a setal stalk.

While the extraordinary adhesion of tokay setae is well established, the mechanics and physics of setal and spatular engagement remain open areas of research. Two competing theories for spatular adhesion are dispersion forces [10] and hydrogen bonding [37], both of which are under the canopy of van der Waals interactions. These forces are only significant at distances up to a few nanometers and so adhesion through van der Waals attraction requires intimate contact between the setal array and substrate.

Mechanisms for setal compliance are discussed in Chapter 4 and motivate the design of curved microfiber arrays presented in Chapter 7. The compliance of individual setae are based on results of resonance testing presented in Chapter 3. Despite the importance of contact mechanics in van der Waals controlled adhesion, little experimental work had been done previously to characterize the elasticity of individual setae and setal arrays. Nonetheless, there have been several theoretical studies of setal compliance. Most treat the setae as cantilever beams [4], [30], [38], [70], [72]. Alternative models are the column buckling model presented in [42], the curved elastic rod model of [60], and the stretching column model in [80]. None of the theoretical treatments consider the tapered region at the base of each setal stalk, which is observed to behave like a flexible hinge. This latter mechanism for setal compliance is briefly discussed at the end of Chapter 4.

Theoretical studies of spatular adhesion have also been presented in the scientific literature. Persson & Gorb [61] and Carbone et al. [16] use plate theory to study the bending of the spatular tip as it conforms to surface roughness on a contacting substrate. [73] treat the tip as an elastic tape and use Kendall adhesion theory [46] to predict the peel strength. Treatments of the spatular tip as a flat punch are found in [80], [25], and [24]. The latter work also presents a computational analysis of setal detachment.

2.2 Attempts at Synthetic Gecko Adhesion

As evident in Figure 1.2, the adhesive system of a gecko is a complex hierarchy of structures that range in size from the macro to nano scales. Creating a complete, synthetic replica of the adhesive system is prohibitive due to current limitations in nanocasting and nanofabrication. Nonetheless, researchers have attempted to produce dry adhesives by imitating some of the more salient and replicable features of the hierarchy.

Previous attempts at synthetic gecko adhesion are too numerous to discuss in great detail. Among the first structures were the polymer nano and micro bumps developed by [70]. The adhesive force for each bump closely matched Johnson, Kendall, Roberts (JKR) theory for an elastic sphere in contact with a rigid flat [44]. However, adhesion over multiple bumps is not possible due to poor load sharing, as discussed in [38]. Without uniform load sharing, stress concentrations form, allowing cracks to propagate through an interface, resulting in premature bond failure.

As discussed at the beginning of Chapter 7, poor load sharing is also expected to occur with vertically aligned microfibers, which must stretch in order to support tension in the presence of interfacial roughness. Nonetheless, [26] demonstrate a high pull-off strength of 3

N/cm^2 for an array of vertically aligned polyimide microfibers in contact with a glass slide. This extraordinary adhesion requires a PSA backing — replacing the PSA backing with a silicon wafer reduces the strength to approximately 0.01 N/cm^2, which is similar to that of a smooth (unstructured) polyimide surface. It is important to note that subsequent groups have failed to replicate this result. Experimental discrepancies are reported in [38] and the matter remains unresolved.

Apart from the work by [26], the only other array of stiff fibers (elastic modulus, $E \geq 1$ GPa) demonstrating adhesion over a significant area (≥ 1 cm) are the vertically aligned carbon nanotubes (VACNT) presented in [83] and the silicon nanowires in [20]. The mechanism for adhesion of a VACNT array is postulated by the side contact model presented in Chapter 5. Other attempts at adhesion with VACNT arrays have been reported in [82] and [76], although these involve contact areas of less than a few square microns — too small to address important concerns such as load sharing and flaw/roughness tolerance.

A hierarchical approach to synthetic gecko adhesion is presented in [57]. In these structures, vertically aligned microfibers (photoresist, $E \sim 4$ GPa) are supported by flexible SiO_2 platforms that simulate lamellae. Measurements performed with a microrough, 3 mm radius probe yield a pull-off strength of several hundred micro-Newtons. Adhesion of these hierarchical structures over significant contact areas remains a topic of open research.

Lastly, there have been numerous attempts at synthetic gecko adhesion with soft polymers. The most recent involves an array of vertically aligned, polyvinylsiloxane (PVS, $E = 3$ MPa) microfibers presented in [31]. By exploiting principles of contact splitting (see also [29]), these structures exhibit a pull-off strength of 1 N/cm^2 over a 0.26 cm^2 area.

Part II

Natural Microfiber Array

Chapter 3

Elastic Modulus of Gecko Setae

Perhaps the most remarkable aspect of natural gecko adhesion is the use of stiff β-keratin to achieve a sticky interface. This is in contrast to conventional pressure sensitive adhesives (PSAs), which incorporate soft, viscoelastic polymers. These materials satisfy Dahlquist's criterion for tack, which requires an elastic modulus E $\leq$ 300 kPa for 1 Hz loading cycles [64].

The mechanical properties of β-keratin are constant over most organisms. Bonser & Purslow [15] approximate a tensile modulus of 2.5 GPa in bird feathers and [14] measure 1.3—1.8 GPa in bird claws. Hence, researchers have estimated that β-keratin in gecko lizards are between 1 and 3 GPa [8]. In designing a synthetic gecko adhesive, it is important to experimentally verify this estimate. Otherwise, efforts to achieve adhesion with stiff materials may be misguided.

Approximate values for the elastic modulus of gecko setae are obtained from resonance tests performed in collaboration with biologist Anne Peattie in the Department of Integrative Biology at the University of California, Berkeley. The biologist obtained the natural

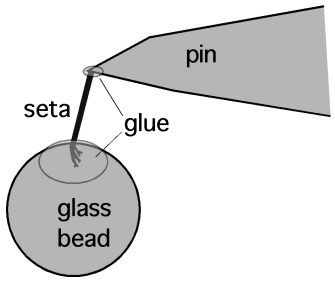

Figure 3.1. Illustration of setal preparation for resonance testing.

frequency of isolated setae under gravitational loading. This work focuses on the dynamical analysis used to map natural frequency to elastic modulus.

3.1 Experimental Overview

As illustrated in Figure 3.1, an isolated setal stalk is oriented vertically with the top end fixed to a stationary insect pin. The bottom end is rigidly glued to a 125 μm radius glass bead. At the beginning of the experiment, the bead is displaced horizontally. After release, the bead swings back and forth. The setal motions are captured with a high speed video camera at 500 or 1000 frames per second.

By counting the number of frames between swinging cycles, it is possible to determine the natural frequency of the system. The elastic modulus is obtained by mapping the natural frequency using equation (3.16), which is derived in the following section. Further details on the experimental set-up and setal harvesting are provided in [59].

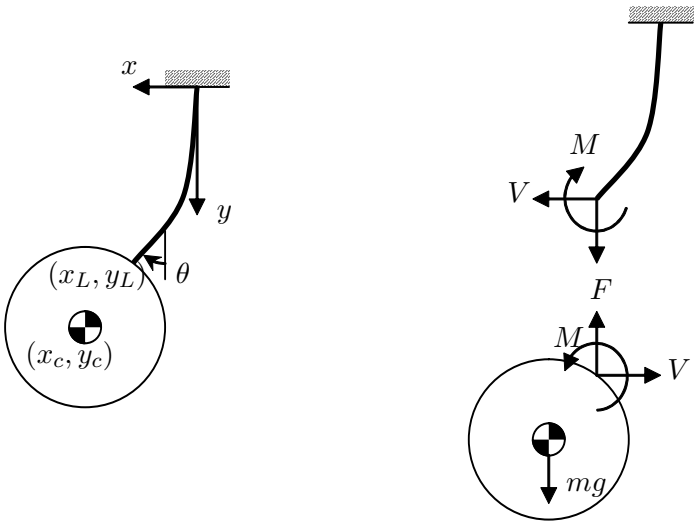

Figure 3.2. Kinematic and free body diagrams of setal stalk of length L and spherical bead of radius c and mass m.

3.2 Theory

The setal preparation is modeled in two dimensions as a planar elastic rod (representing the setal stalk) supporting a rigid sphere (glass bead). Let L denote the length of the seta and define the arclength ξ such that $\xi = 0$ at the top support. At each end, the seta is assumed to be "built-in" to the contacting substrate and is thus subject to both a point force and moment at $\xi = 0$ and $\xi = L$.

3.2.1 Kinematics

Let $x = x(\xi)$ and $\theta = \theta(\xi)$ represent the lateral displacement and slope of the fiber, respectively. Assuming small deflections (i.e. $\theta < \pi/12$) θ is approximately equal to x', where the prime denotes a derivative with respect to ξ.

For an elastic rod subject only to point loads at its ends, $x = x(\xi)$ is a solution to the

differential equation

$$x''''(\xi) = 0 \qquad \forall\, \xi \in [0, L]. \tag{3.1}$$

Applying the boundary conditions $x(0) = \theta(0) = 0$ and defining $\theta_L := \theta(L)$ and $x_L := x(L)$, it follows from (3.1) that

$$\begin{aligned} x(\xi) &= (\theta_L L - 2x_L)\left(\frac{\xi}{L}\right)^3 - (\theta_L L - 3x_L)\left(\frac{\xi}{L}\right)^2 \\ \theta(\xi) &= 3\left(\theta_L - 2\frac{x_L}{L}\right)\left(\frac{\xi}{L}\right)^2 - 2\left(\theta_L - 3\frac{x_L}{L}\right)\left(\frac{\xi}{L}\right). \end{aligned} \tag{3.2}$$

Referring to Figure 3.2, define $\{x_c, y_c\}$ to be the position of the bead's center of mass. Noting that the bead has radius c, it follows that

$$x_c = x_L + c\sin\theta_L \qquad \text{and} \qquad y_c = \int_0^L \cos\theta\, d\xi + c\cos\theta_L. \tag{3.3}$$

Since the bead swings back and forth during resonance, it is also important to establish the acceleration of the bead in terms of x_L, θ_L and their time derivatives. Letting a dot represent the time derivative, it follows from (3.3) that

$$\ddot{x}_c = \ddot{x}_L + c\ddot{\theta}_L - c\theta_L\dot{\theta}_L^2 \tag{3.4}$$

and

$$\begin{aligned} \ddot{y}_c &= -\int_0^L \{\theta\ddot{\theta} + \dot{\theta}^2\}\, d\xi - c\theta_L\ddot{\theta}_L - c\dot{\theta}_L^2 \\ &= -\frac{6}{5L}\dot{x}_L^2 + \frac{1}{5}\dot{x}_L\dot{\theta}_L - \frac{6}{5L}x_L\ddot{x}_L + \frac{1}{10}\theta_L\ddot{x}_L + \frac{1}{10}x_L\ddot{\theta}_L \\ &\quad - \left(c + \frac{2}{15}L\right)\left(\dot{\theta}_L^2 + \theta_L\ddot{\theta}_L\right). \end{aligned} \tag{3.5}$$

Noting that θ is small, it has been assumed here that $\sin\theta \approx \theta$ and $\cos\theta \approx 1$.

3.2.2 Constitutive Equations

The tip configuration $\{x_L, \theta_L\}$ is determined by the shear force V and moment M imparted by the glass bead at $\xi = L$. These loads are defined in the free body diagram of

Figure 3.2. Specifically, the rod kinematics $\{x_L, \theta_L\}$ and forces $\{V, M\}$ are related through the constitutive law

$$EI\theta'(\xi) = M + V\xi. \tag{3.6}$$

Taking the derivative of (3.2) and comparing this with (3.6) implies

$$V = \frac{6EI}{L^2}\left(\theta_L - 2\frac{x_L}{L}\right) \qquad \text{and} \qquad M = -\frac{2EI}{L}\left(\theta_L - 3\frac{x_L}{L}\right). \tag{3.7}$$

Solving for x_L and θ_L yields

$$x_L = \frac{VL^3}{3EI} + \frac{ML^2}{2EI} \qquad \text{and} \qquad \theta_L = \frac{VL^2}{2EI} + \frac{ML}{EI}. \tag{3.8}$$

3.2.3 Linear and Angular Momentum Balance

In addition to the constitutive law, $\{x_L, \theta_L\}$ and $\{V, M\}$ are related through the balance laws for linear and angular momentum. First, consider the linear momentum balance of the glass bead in the horizontal direction. Again referring to the free body diagram in Figure 3.2, it follows that $-V = m\ddot{x}_c$. Substituting (3.4) for $\ddot{x}_c$ then implies

$$V = -m(\ddot{x}_L + c\ddot{\theta}_L - c\theta_L\dot{\theta}_L^2). \tag{3.9}$$

Similarly, balancing the linear momentum in the vertical directions yields $mg - F = m\ddot{y}_c$, which implies

$$F = m(g - \ddot{y}_c). \tag{3.10}$$

The moment M is obtained by performing the angular momentum balance about the bead center of mass. This implies

$$Vc\cos\theta_L - M - Fc\sin\theta_L = J\ddot{\theta}_L \tag{3.11}$$

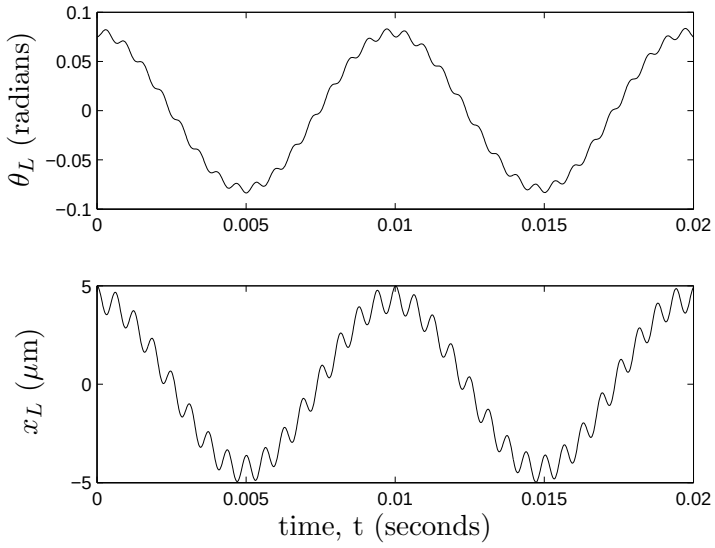

Figure 3.3. Time plots of $z_1 = \theta_L$ and $z_3 = x_L$.

where, for a sphere of radius c, the mass moment of inertia is

$$J = \frac{2}{5}mc^2 \tag{3.12}$$

and $g = 9.81$ m/s^2 is the constant of gravitational acceleration. Solving for M and substituting the expressions for $\ddot{x}_c$ and $\ddot{y}_c$,

$$\begin{aligned} M &\approx c(V - F\theta_L) - J\ddot{\theta}_L = mc\{-\ddot{x}_c - (g - \ddot{y}_c)\theta_L\} - J\ddot{\theta}_L \\ &= mc\Bigg\{ -\ddot{x}_L - (1+\theta_L^2)c\ddot{\theta}_L - g\theta_L - \frac{6}{5L}\theta_L\dot{x}_L^2 + \frac{1}{5}\theta_L\dot{x}_L\dot{\theta}_L - \frac{6}{5L}x_L\theta_L\ddot{x}_L \\ &\qquad + \frac{1}{10}\theta_L^2\ddot{x}_L + \frac{1}{10}x_L\theta_L\ddot{\theta}_L - \frac{2}{15}L\theta_L\dot{\theta}_L^2 + \frac{2}{15}L\theta_L^2\ddot{\theta}_L \Bigg\} - J\ddot{\theta}_L. \end{aligned} \tag{3.13}$$

3.2.4 Analysis

Substituting the expressions (3.9) and (3.13) into (3.8) and solving for $\ddot{\theta}_L$ and $\ddot{x}_L$ yields a system of equations of the form

$$\ddot{\theta}_L = u(\theta_L, \dot{\theta}_L, x_L, \dot{x}_L) \qquad \text{and} \qquad \ddot{x}_L = v(\theta_L, \dot{\theta}_L, x_L, \dot{x}_L) \tag{3.14}$$

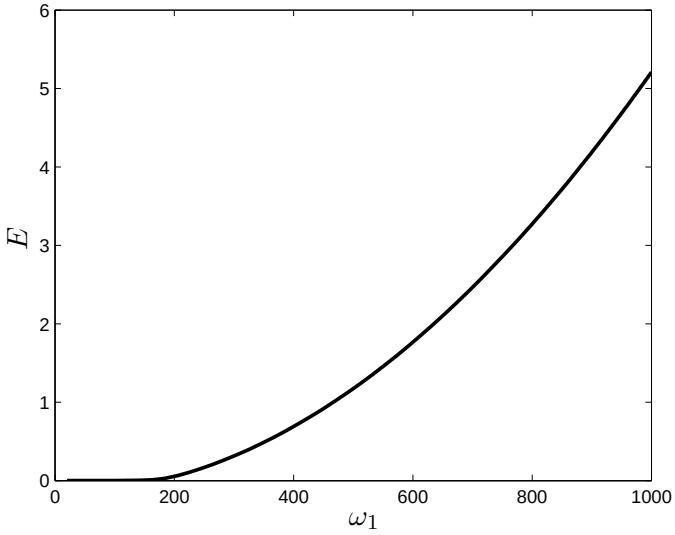

Figure 3.4. Plot of E (in GPa) versus ω_1 (in rad/sec) for $L = 100\,um$, $R = 2\,um$, $c = 125\,um$, $g = 9.81\,m/s^2$ and $\rho = 2200\,kg/m^3$.

Defining the state variable $\mathbf{z} = (\theta_L\ \dot{\theta}_L\ x_L\ \dot{x}_L)^\top$, it follows that

$$\dot{\mathbf{z}} = \mathbf{f}(\theta_L, \dot{\theta}_L, x_L, \dot{x}_L)$$

where $\mathbf{f} = (z_2\ u(\mathbf{z})\ z_4\ v(\mathbf{z}))^\top$.

For example, let L=100 μm, R=2 μm, $I = \pi R^4/4$, $c = 125$ μm, $g = 9.81$ m/s^2, $\rho = 2200$ kg/m^3, $m = (4/3)\pi\rho c^3$, and $E = 2$ GPa. Also, assume an initial displacement $x_0 = L/20$, which corresponds to a slope $\theta_0 = (3x_0)/(2L)$ at the tip. The corresponding time plots for $z_1 = \theta_L$ and $z_3 = x_L$ are displayed in Figure 3.3. It is evident that x_L and θ_L have similar frequencies and are in phase. Let ω_1 and ω_2 denote the low and high natural frequencies, respectively. The period associated with each frequency is $2\pi/\omega$ and is measured from the plots to be T$_1$=0.01 s and T$_2$ = 0.0006 s for the low and high frequencies. Hence, $\omega_1 = 628$ rad/sec and $\omega_2 = 10500$ rad/sec.

The natural frequencies can be represented mathematically by linearizing the system $\dot{\mathbf{z}} = \mathbf{f}(\mathbf{z})$ and taking the eigenvalues of the corresponding Jacobian $\mathbf{H}$ at the equilibrium

point $\mathbf{z} = (0\ 0\ 0\ 0)^\top$. Performing the necessary manipulations in *Mathematica* 5.1 (Wolfram Research, Inc.)

$$\mathbf{H} = \begin{bmatrix} 0 & 1 & 0 & 0 \\ -\frac{6EIc+4EIL+mgL^2c}{JL^2} & 0 & \frac{6EI(L+2c)}{JL^3} & 0 \\ 0 & 0 & 0 & 1 \\ \frac{90EI(J+mc^2)+60EImLc+15m^2gL^2c^2}{15mJL^2} & 0 & -\frac{6EI(2J+mc*(L+2c)}{mJL^3} & 0 \end{bmatrix}. \tag{3.15}$$

From the eigenvalue corresponding to ω_1, it follows that

$$\begin{aligned} E &= \frac{1}{6I}\omega_1^2 \Bigg\{ 3L(J+mc^2) + mL^3 + 3mcL\left(L - \frac{g}{\omega_1^2}\right) \\ &\quad + L\sqrt{3mL^2\left(\frac{mgc}{\omega_1^2} - J\right) + \left[3(J+mc^2) + mL^2 + 3mc\left(L - \frac{g}{\omega_1^2}\right)\right]^2} \Bigg\}. \end{aligned} \tag{3.16}$$

3.3 Results

Figure 3.4 is a plot of E versus ω_1 for $c = 125$ μm, $g = 9.81$ m/s^2, mass density $\rho = 2200$ kg/m^3, $L = 100$ μm, and $R = 2$ μm. For natural setae, ω_1 is typically close to 600 rad/sec, and so Figure 3.4 predicts an elastic modulus between 1 and 2 GPa.

Applying equation (3.16) to measured values of L, R, and ω_1, [59] determined that setae harvested from *Gekko* and *Ptyodactylus* lizards exhibit a similar elastic modulus of 1.53 GPa ($\pm$ 0.063 SE, n = 165) and 1.42 GPa ($\pm$ 0.058, n = 194), respectively. This is close to values for β-keratin measured in other species and suggests that biologists have been correct in their assumptions about the stiffness of gecko setae.

Chapter 4

Effective Modulus of the Setal Array

As discussed in the previous chapter, gecko setae are made of β-keratin with an elastic modulus (E) of approximately 1.5 GPa. This seemingly contradicts Dahlquist's criterion for pressure sensitive adhesion, which requires E $\leq$ 300 kPa. Indeed, adhesion is only possible when the elastic restoring forces are small compared to the strength of interfacial bonds formed with an opposing surface. For a material of modulus E $\sim$ 1 GPa in contact with a typical microrough surface, elastic restoring forces far exceed the strength of van der Waals bonds, leading to spontaneous detachment as the material springs off the surface. How, then, is the gecko able to achieve adhesion with such a vast range of substrates?

The competition between elastic restoring forces and surface forces, primarily those achieved through van der Waals interactions, is a governing principle in natural and synthetic gecko adhesion. Since van der Waals forces vary modestly over most polymeric and oxidized materials [41], designs should emphasize minimization of the elastic restoring forces. This demands a *compliant* interface, i.e. a structure that requires little force to

accommodate displacements due to misalignments, fiber height variation, rough surfaces and any other geometric irregularities. Determining the mechanism by which the setal array achieves compliance is essential towards understanding gecko adhesion. Moreover, this insight can aid in designing a synthetic fiber array with similar properties.

This chapter presents a model for the compliance of an array of tokay setae. This model is supported experimentally with tests performed by biologists in the Department of Biology at Lewis & Clark College. The biologists obtain an *effective* elastic modulus for the setal array that is consistent with Dahlquist's criterion for tack.

4.1 Elastic Rod Model

As in previous studies of setal deformation [4], [30], [38], [42], [60], [70], [72], a single seta is modeled as an elastic, cylindrical rod of modulus E, length L, radius R and area moment of inertia $I = \pi R^4/4$. In its natural configuration, the seta is assumed to be straight and oriented at an angle ϕ from the direction normal to its support. Under pure compression, the tip of the seta is subject to a normal force F. This results in a normal displacement Δ towards the supporting plane.

If the rod is naturally perpendicular to the substrate (i.e. $\phi = 0$), then Δ is only significant after a critical buckling load is exceeded. For this special case, the seta is studied by a buckling column model [42]. Microscopic images of the setal array, however, show that setae are naturally deflected from the perpendicular axis (see Figure 1.2). When $\phi > 0$, a more general model is used to study setal deformation. This is furnished by elastica theory [22], which, in the present case, yields the concise solution

$$\Delta = L\cos(\phi) - \{\mathrm{F}(p,m) - \mathrm{F}(p,n) + 2\mathrm{E}(p,n) - 2\mathrm{E}(p,m)\}/k \tag{4.1}$$

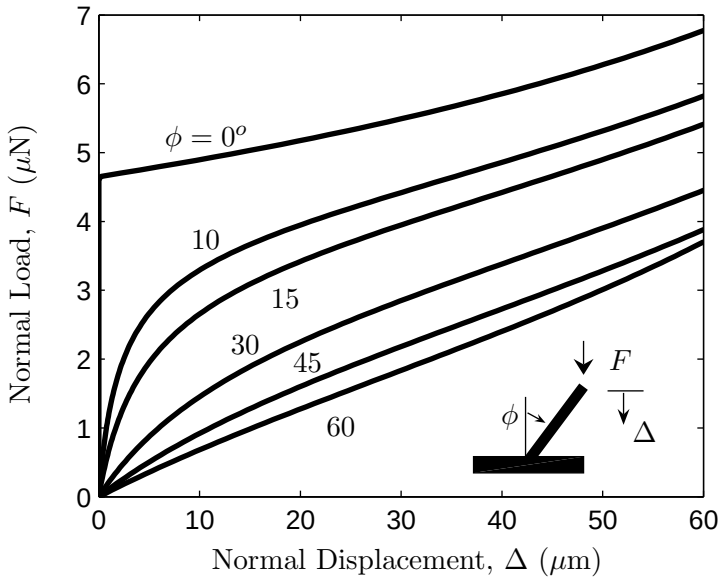

Figure 4.1. Force-displacement relationship of an elastic rod for $L = 100$ μm, $R = 2$ μm, and $E = 1.5$ GPa.

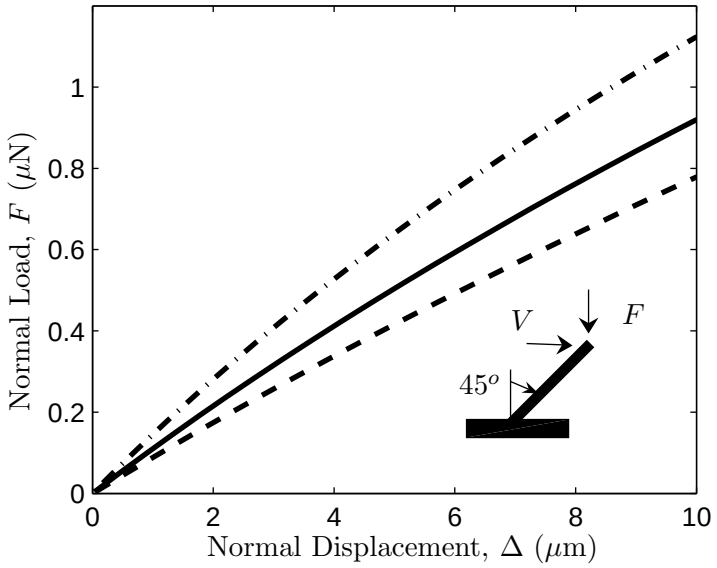

Figure 4.2. Tip subject to shear load V; $L = 100$ μm, $R = 2$ μm, $E = 1.5$ GPa, and $\phi = 45^o$; (solid) $V = 0$, (dashed) $V = \mu F$, (dash-dot) $V = -\mu F$.

where F$(\bullet,\bullet)$ and E$(\bullet,\bullet)$ are the elliptic integrals of the first and second kind, respectively, $n = \pi/2$, $k = \sqrt{F/EI}$, $m = \arcsin(\sin(\phi/2)/p)$, and the modulus p is the solution to

$$kL = F(p,n) - F(p,m). \tag{4.2}$$

The modulus p is determined numerically over the domain $\sin(\pi/4-\phi/2)$ to $\sin(3\pi/4-\phi/2)$ by solving (4.2) with a nonlinear equation solver in Matlab 7 (The Mathworks Inc., 2004). Substituting the solution for p into (4.1) yields a relationship between the applied load F and the tip displacement Δ. Plots of F vs. Δ for various values of ϕ are given in Figure 4.1. The figure shows a smooth transition from cantilever bending to column buckling as ϕ decreases.

4.2 Bending with Friction at the Tip

Following arguments in [22], equation (4.1) can be modified to admit an additional shear load V that acts on the tip in the direction parallel to the plane of the supporting substrate. Defining

$$\alpha = \phi + \arctan(F/V), \tag{4.3}$$

it follows that

$$\Delta = L\cos(\phi) - \frac{1}{k}\{[\mathrm{F}(p,m) - \mathrm{F}(p,n) + 2\mathrm{E}(p,n) - 2\mathrm{E}(p,m)]\cos(\alpha-\phi) + 2p\cos(m)\sin(\alpha-\phi)\}, \tag{4.4}$$

where now $m = \arcsin(\sin(\alpha/2)/p)$.

The force V is generated when the setal array is dragged along the surface during compressive loading. The magnitude is limited by Coulomb friction and so in general

$$|V| = \mu F + S \tag{4.5}$$

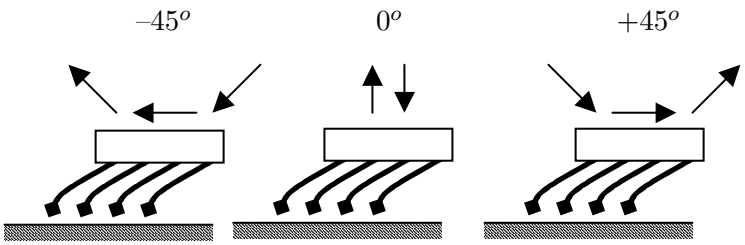

Figure 4.3. Illustration of various loading conditions for setal array brought in contact with a fixed PTFE substrate.

where the friction coefficient μ is typically 0.25 and S is the shear strength due to interfacial adhesion. Since measurements are performed on a PTFE (Teflon$^{\text{TM}}$) substrate with relatively large compressive loads, the contribution of adhesion to the shear force is negligible and so (4.5) is assumed to reduce to $|V| = \mu F$.

Referring to Figure 4.2, it is apparent that for a rod with a natural deflection of $\theta = \pi/4$, shearing in the direction of its natural orientation (i.e. $V = \mu F$) effectively *softens* the rod. That is, the mechanical response to compressive displacements is reduced. Conversely, dragging the rod against its natural orientation ($V = -\mu F$), causes the rod to *stiffen*, resulting in a larger compressive force necessary to achieve a prescribed displacement. (Also shown for cantilever by Sitti & Fearing [70]).

Lastly, it is interesting to note that using the full expression in equation (4.5) leads to a prediction of an effective friction coefficient that is compatible with experimental measurements. The effective friction coefficient $\hat{\mu}$ is defined as the ratio of the measured shear force to the applied compressive load. Mathematically, this may be represented as

$$\hat{\mu} = V/F = \mu + S/F. \tag{4.6}$$

Since the setal array is more compliant under $+45^o$ compression, a smaller load F is necessary to achieve a prescribed normal displacement. Hence, by (4.6), the effective friction coefficient is expected to by larger than for -45^o compression. This trend is consistent with the values of 0.24 and 0.29 measured for the -45^o and $+45^o$ trials, respectively [8]. The loading conditions for these two cases are illustrated in Figure 4.3.

4.3 Results

In predicting the effective elastic modulus $\hat{E}$ of a setal array, it is assumed that $\phi = 45^o$. This is close to the estimate of 47^o obtained by comparing setal height (68 μm) with length ($\approx$ 100 μm) [8]. From Figure 4.2 it follows that 0.92 μN of compression is required to displace a setal tip by 10 microns. If friction is simultaneously applied, then the necessary compressive force becomes 0.78 or 1.1 μN depending on whether the friction is applied along or against the natural orientation, respectively. Treating the seta as a linear spring, the spring constants corresponding to these three loading conditions are $k_0 = 0.092$, $k_+ = 0.078$, and $k_- = 0.11$ N/m. Lastly, the effective elastic modulus is related to the setal spring constant through the relationship

$$\hat{E} = DLk, \tag{4.7}$$

where D is the setal density.

The density of a tokay setal array is approximately $D = 1.44 \times 10^{10}$ mm^{-2} [68]. Hence, it follows from (4.7) that $\hat{E}_0 = 130$ kPa, $\hat{E}_+ = 110$ kPa, and $\hat{E}_- = 160$ kPa. These correspond to the effective elastic modulus for the 0^o, $+45^o$, and -45^o loading conditions, respectively (see Figure 4.3).

Experimental values for $\hat{E}$ are obtained with a motorized force platform prepared by

Loading Direction	$\hat{E}_{\text{th}}$ (kPa)	$\hat{E}_{\text{exp}}$, Loading (kPa)	$\hat{E}_{\text{exp}}$, Unloading (kPa)
0^o	130	83 ± 4.0 SE	89 ± 3.8 SE
$+45^o$	110	86 ± 4.4 SE	78 ± 3.8 SE
-45^o	160	110 ± 4.7 SE	113 ± 4.7 SE

Table 4.1. Elastic modulus of a tokay setal array; ($\hat{E}_{\text{th}}$) theory, ($\hat{E}_{\text{exp}}$) experimental; theoretical predictions based on $L = 100$ μm, $R = 2$ μm, $E = 1.5$ GPa, and $\phi = 45^o$;

biologists at Lewis & Clark College. See [8] for further details on the experimental methods. Table 4.1 compares the theoretical and experimental values for the effective modulus. As shown in the last column, the theoretical predictions overestimate the experimental measurements by as much as 57%. This discrepancy implies that the setae deform in ways other than elastica bending. One current hypothesis is that the setae also rotate at their base, where, due to slight tapering, the stalk diameter is at its minimum [59]. Rotation at the base is most apparent in force measurements performed on isolated setae.

Both theory and experiment suggest that the setal array approximately satisfies Dahlquist's criterion for tack. Moreover, the experiments confirm that the fiber array *stiffens* when dragged against its natural orientation. In conclusion, these results demonstrate the PSA level compliance of the setal array and emphasize the important role of elastic bending in setal deformation. Such insights will guide designs for synthetic fiber arrays presented in the following chapters.

Part III

Synthetic Nano/Microfiber Arrays

Chapter 5

Adhesion of Nanofibers through Side Contact

Inspired by the remarkable adhesion properties of the natural gecko, researchers have endeavored to develop fiber array adhesives from stiff (E > 1 GPa), otherwise non-sticky materials. Among the most successful such structures are arrays of vertically aligned nanofibers (VANF). Unlike with the polyimide micropillars tested by [26], multiple researchers have independently verified adhesion with various VANF arrays. Recent successes include 10 N/cm^2 tensile strength with vertically aligned multi-walled carbon nanotubes (VACNT) [83], 2 N/cm^2 shear strength with silicon wires [20], and an estimated 0.5 N/cm^2 pull-off strength for a spherical probe in contact with polyimide nanofibers [69].

A novel model for nanofiber deformation under tension is presented in Section 5.2. This model postulates that fibers contact a surface by bending over and adhering along their side. For sufficiently slender fibers, the interfacial forces (eg. van der Waals bonds) exceed the elastic restoring forces, making the *side contact* stable even as the fiber is pulled from

the substrate. In this case, the tensile compliance is high compared to the end contact and proportional to the peel length of the fiber.

VANF arrays exhibit exceptional adhesion, exceeding the tensile strength of the natural gecko. However, the same mechanism that leads to side contact also causes fibers to stick to their neighbors and form large clumps. These clumps may form after only a few loading cycles and thus prevent the array from exhibiting repeatable adhesion. Clumping is thus an important consideration in formulating the design principles for VANF adhesion, which are presented in Section 5.6.

5.1 Overview of Elastica Theory

As with natural setae (Chapter 4), it is convenient to study the mechanical deformation of synthetic fibers using elastica theory. The elastica is a planar elastic rod that deforms only by elastic bending. As in the previous chapters, the rod is a cylinder with radius R, length L, area moment of inertia $I = \pi R^4/4$, and elastic modulus E.

5.1.1 Kinematics

The configuration of the rod is represented by a one-dimensional curve Ω embedded in $\mathbb{R}^2$. The space $\mathbb{R}^2$ is spanned by unit vectors $\mathbf{e}_1$ and $\mathbf{e}_2$, which are normal and parallel to the tangent plane of the supporting surface, respectively. Letting $\mathbf{e}_3 = \mathbf{e}_1 \times \mathbf{e}_2$, it follows that $\{\mathbf{e}_1, \mathbf{e}_2, \mathbf{e}_3\}$ forms a right-handed orthonormal triad. Ω is parameterized by the coordinate ξ, which convects with the curve.

The position of a point on Ω is defined by the vector $\mathbf{r} = \mathbf{r}(\xi)$, which maps $\xi \in [0, L]$ to the fixed frame $\{\mathbf{e}_1, \mathbf{e}_2\}$. Similarly, points in the natural (undeformed) configuration, Ω_0,

are defined by $\mathbf{R} = \mathbf{R}(\xi)$. For an elastica,

$$\mathbf{r}' = \cos\theta \mathbf{e}_1 + \sin\theta \mathbf{e}_2, \tag{5.1}$$

where the slope $\theta = \theta(\xi)$ is defined as the angular deflection of the curve from the $\mathbf{e}_1$ axis and the prime denotes a derivative with respect to ξ. In the natural configuration, $\mathbf{r}$ and θ are replaced with $\mathbf{R}$ and θ_0, respectively.

5.1.2 Governing Equations

The balance laws pertaining to the internal force $\mathbf{n} = \mathbf{n}(\xi)$ and internal moment $\mathbf{m} = \mathbf{m}(\xi)$ are

$$\mathbf{n}' = \mathbf{0} \qquad \text{and} \qquad \mathbf{m}' + \mathbf{r}' \times \mathbf{n} = \mathbf{0}. \tag{5.2}$$

The constitutive equation is

$$\mathbf{m} = EI\theta' \mathbf{e}_3. \tag{5.3}$$

It is important to remark that elastica theory only concerns rod bending — stretching, shearing, and (for three dimensional analysis) torsion are neglected. This is reasonable since bending stiffness is on the order of ER^4/L^3 whereas stretching and shearing have a stiffness of order ER^2/L. Hence, bending will result in a tip displacement that is typically $(L/R)^2$ times greater than that from stretching or shearing. For natural and synthetic gecko fibers, $L \gg R$, and so this ratio will be quite large. One exception is when the rod is subject to pure axial tension. In this case, displacement will be dominated by stretching. However, for the geometries of interest, the absolute tip displacement will only be on the order of several nanometers and hence may be neglected.

Consider an axial load $\mathbf{F} = -F\mathbf{e}_1$ acting on the tip of a vertical fiber. Combining (5.2)

and (5.3) yields the second order differential equation

$$EI\theta'' + F\sin\theta = 0. \tag{5.4}$$

Since the fiber is naturally vertical and has no moment acting on its tip, it follows that

$$\theta(0) = \theta'(L) = 0. \tag{5.5}$$

5.2 Side Contact

The tensile compliance of fibers in a VANF array is explained with the *side contact* model. According to this theory, a fiber contacts an opposing surface by bending over and adhering along its side. Adhesion results in a two-phase state in which the rod is either free or contacting the opposing surface. Classical beam theories are not sufficient as they do not furnish the additional balance law needed to locate the phase interface.

Three formulations for studying elastica problems of this type are presented in [52]. These include stationary principles, the surface integral of Eshelby's energy-momentum tensor, and the material (configuration) force balance. Only the method involving stationary principles will be studied here.

5.2.1 Preliminaries

The rod is treated as a two phase elastica composed of a non-contacting and contacting portion, denoted by Ω_α and Ω_β, respectively. Following the convention of [33], these two portions are assumed to be closed complementary subregions of Ω that share an interface $\mathcal{I} = \Omega_\alpha \cap \Omega_\beta$. Furthermore, it is assumed that Ω_α, Ω_β, and $\mathcal{I}$ are identified with the coordinates $[0, \gamma]$, $[\gamma, L]$, and $\{\gamma\}$, respectively, where L is the rod length and γ is generally unknown.

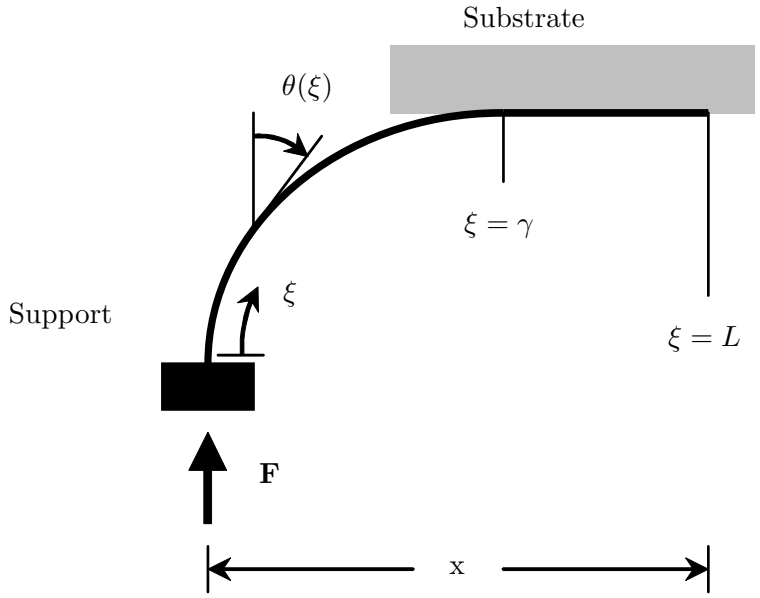

Figure 5.1. Deformation of an elastic fiber, clamped vertically at its base, making contact with an adhering substrate over a length $L - \gamma$.

This analysis concerns functions of the form $\chi : \Omega \to \mathbb{R}$, some of them having a discontinuity at $\xi = \gamma$. It is convenient to decompose χ into continuous functions χ_α and χ_β on the domains Ω_α and Ω_β, respectively. In general, $\chi_\alpha = \chi_\alpha(\xi, \theta, \theta')$ and since $\theta(\xi)$ is prescribed on Ω_β, $\chi_\beta = \chi_\beta(\xi)$. At the phase interface $\xi = \gamma$, these functions are defined explicitly as their limit points. Lastly, the jump in χ is denoted by $[\![\chi]\!] = \chi_\beta(\gamma) - \chi_\alpha(\gamma)$.

5.2.2 Lagrangian Density

When contacting a surface, the rod is subject to an external point force $\mathbf{F} = F\mathbf{e}_1$ at $\xi = 0$ (See Figure 5.1). Since $\mathbf{n}' = \mathbf{0}$, this implies that $\mathbf{n} = -F\mathbf{e}_1$ on Ω_α. Noting that $\mathbf{r}(L)$ is fixed, the potential energy associated with the external loads is

$$\mathbf{F} \cdot (\mathbf{r}(0) - \mathbf{r}(L)) = \int_0^L F \cos\theta \, d\xi. \tag{5.6}$$

Another contributions to the potential energy of the system is the elastic strain energy per unit length of ξ:

$$\psi(\theta') = \frac{1}{2}EI(\theta')^2. \tag{5.7}$$

Lastly, the rod is subject to an external potential energy $u = u(\xi)$ associated with adhesion. Here, $u = 0$ on Ω_α and $u = -\omega$ on Ω_β, where ω is the energy of adhesion per unit length of contact. In general, both u and ψ will have a discontinuity at the phase interface. Hence, the Lagrangian density for a static rod,

$$f(\xi, \theta(\xi), \theta'(\xi)) = F\cos\theta + \psi + u, \tag{5.8}$$

will be a piecewise continuous function with a jump at $\xi = \gamma$.

5.2.3 Energy of Adhesion Per Contact Length, ω

The energy of adhesion per unit length of contact between a cylindrical rod and a flat is denoted by the parameter ω. When a cylinder lies on a flat surface, interfacial forces between the fiber and substrate will cause the fiber cross-section to deform and make contact over a width $2c$ [18], [30]. Assuming linear elasticity, the corresponding strain energy release rate is found to be

$$G = \pi E c^3/32(1-\nu^2)R^2, \tag{5.9}$$

where ν is Poisson's ratio for the cylinder. Integrating G to obtain the strain energy and adding the energy of adhesion, the total potential energy per unit length of contact is

$$U(c) = \frac{\pi E c^4}{128(1-\nu^2)R^2} - 2cW_{\text{ad}}. \tag{5.10}$$

where W_{ad} is the work of adhesion between the two surfaces.

At equilibrium, $\partial U/\partial c = 0$ and $c > 0$, which gives

$$c = 4\left[\frac{W_{\text{ad}}(1-\nu^2)R^2}{\pi E}\right]^{1/3} =: c^*. \tag{5.11}$$

The energy of adhesion per unit length of contact is thus

$$\omega := -U(c^*) = 6\left[\frac{(1-\nu^2)R^2{W_{\text{ad}}}^4}{\pi E}\right]^{1/3}. \tag{5.12}$$

5.2.4 Natural Boundary Condition

Classical elastica theory yields the governing equations (5.2,5.3), which must be solved to determine $\theta_\alpha(\xi)$ at static equilibrium for a given γ. Since such a solution is unique, the problem reduces to a one-dimensional search for the value of γ at equilibrium, denoted by γ^*. This equilibrium value is obtained from a natural boundary condition at the phase interface that is derived using the principle of stationary potential energy.

The total potential energy of the system is computed as

$$\Phi(\theta,\gamma) = \int_0^\gamma f_\alpha(\xi,\theta,\theta')\,d\xi + \int_\gamma^L f_\beta(\xi)\,d\xi. \tag{5.13}$$

According to the principle of stationary potential energy, the rod assumes a configuration $\{\theta^*(\xi),\gamma^*\}$ such that the action Φ is extremized. Since θ_β is prescribed, a necessary condition for Φ to be extremized is the Euler-Lagrange differential equation on Ω_α:

$$\frac{\partial f_\alpha}{\partial \theta_\alpha} - \frac{\partial}{\partial \xi}\left(\frac{\partial f_\alpha}{\partial \theta'_\alpha}\right) = 0. \tag{5.14}$$

Substituting the expression for f into (5.14) yields the governing equation (5.4).

A natural boundary condition at $\xi = \gamma$ is obtained by applying the Kendall theory of adhesion, which states that at equilibrium, $d\Phi/d\gamma = 0$ [46], [62], [63]. By the Leibniz rule,

$$\frac{d\Phi}{d\gamma} = -[\![\, f \,]\!] + \int_0^\gamma \left\{\frac{\partial f_\alpha}{\partial \theta_\alpha}\frac{\partial \theta_\alpha}{\partial \gamma} + \frac{\partial f_\alpha}{\partial \theta'_\alpha}\frac{\partial \theta'_\alpha}{\partial \gamma}\right\} d\xi. \tag{5.15}$$

For a stationary function θ_α satisfying (5.14), the integrand is the derivative of $(\partial f_\alpha/\partial\theta'_\alpha)(\partial\theta_\alpha/\partial\gamma)$. Also noting that $(\partial\theta_\alpha/\partial\gamma)_0 = 0$ and $(\partial\theta_\alpha/\partial\gamma)_\gamma = -\theta'_\alpha(\gamma)$, it follows that the condition $d\Phi/d\gamma = 0$ reduces to

$$[\![f]\!] + \theta'_\alpha(\gamma)\left(\frac{\partial f_\alpha}{\partial\theta'_\alpha}\right)_\gamma = 0. \tag{5.16}$$

at $\xi = \gamma$. It is interesting to note that despite the discontinuity of f at $\xi = \gamma$, this result is equivalent to the second Weierstrass-Erdmann corner condition. The first Weierstrass-Erdmann corner condition, however, doesn't apply since $\theta(\gamma)$ is prescribed.

Lastly, substituting the expression (5.8) for the Lagrangian density into (5.16), yields the natural boundary condition

$$\frac{1}{2}EI(\theta'_\alpha(\gamma))^2 = \omega. \tag{5.17}$$

In addition to this are the kinematic boundary conditions:

$$\theta_\alpha(0) = 0 \qquad \text{and} \qquad \theta_\alpha(\xi) = \frac{\pi}{2} \quad \forall\, \xi \in [\gamma, L] \tag{5.18}$$

5.2.5 Solution

The equilibrium configuration $\{\theta^*(\xi), \gamma^*\}$ is the solution of the Euler-Lagrange differential equation (5.4), the kinematic boundary conditions (5.18) and the natural boundary condition (5.17). First, consider the general solution to (5.4). Defining $\kappa = \sqrt{F/EI}$, it follows that

$$\theta_\alpha(\xi) = 2\,\mathrm{am}\left(\frac{1}{2}\sqrt{(2\kappa^2 + C_1)(\xi + C_2)^2}\,,\ \frac{4\kappa^2}{2\kappa^2 + C_1}\right), \tag{5.19}$$

where $\mathrm{am}(u, m)$ is the Jacobi amplitude, m is the modulus, and C_1 and C_2 are the constants of integration.

The boundary condition $\theta(0) = 0$ implies that the first argument in the Jacobi amplitude

is zero (i.e. $\mathrm{am}(u,m) = 0 \Leftrightarrow u = 0$). Hence,

$$\frac{1}{2}\sqrt{(2\kappa^2 + C_1)C_2^2} = 0. \tag{5.20}$$

Since $2\kappa^2 + C_1 = 0$ would imply an infinite modulus m, (5.20) implies $C_2 = 0$. Defining

$$C = \sqrt{\frac{4\kappa^2}{2\kappa^2 + C_1}}, \tag{5.21}$$

it follows from (5.19) that

$$\theta_\alpha(\xi) = 2\,\mathrm{am}\left(\frac{\kappa\xi}{C}\,,\,C^2\right). \tag{5.22}$$

Next, consider the boundary condition $\theta(\gamma) = \pi/2$. This implies,

$$2\,\mathrm{am}\left(\frac{\kappa\gamma}{C}\,,\,C^2\right) = \frac{\pi}{2}. \tag{5.23}$$

Solving for γ yields

$$\gamma = \frac{C}{\kappa}\mathrm{F}\left(\frac{\pi}{4}\,,\,C^2\right), \tag{5.24}$$

where $\mathrm{F}(\phi, m)$ is the elliptic integral of the first kind. The functions $\phi = \mathrm{am}(u,m)$ and $\mathrm{F}(\phi,m)$ are related through the identity

$$u = \mathrm{F}(\phi, m) = \int_0^\phi \frac{dt}{\sqrt{1 - m\sin^2 t}}. \tag{5.25}$$

Substituting (5.22) into the boundary condition (5.17) implies

$$\frac{2\kappa}{C}\,\mathrm{dn}\left(\frac{\kappa\gamma}{C}\,,\,C^2\right) = \sqrt{\frac{2\omega}{EI}}. \tag{5.26}$$

where the elliptic function $\mathrm{dn}(u,m)$ is defined as

$$\mathrm{dn}(u,m) = \sqrt{1 - m\sin^2\phi} \tag{5.27}$$

Hence, substituting (5.24) into (5.26),

$$\sqrt{\frac{2\omega}{EI}} \equiv \frac{2\kappa}{C}\,\mathrm{dn}\left(\mathrm{F}\left(\frac{\pi}{4}\,,\,C^2\right)\,,\,C^2\right) = \frac{2\kappa}{C}\sqrt{1 - C^2\sin^2\frac{\pi}{4}}. \tag{5.28}$$

Solving for C yields

$$C = \sqrt{\frac{2}{1+\omega/EI\kappa^2}}. \tag{5.29}$$

Lastly, substituting the expression for C into (5.22) and (5.24) and recalling that $\kappa^2 = F/EI$:

$$\theta_\alpha^*(\xi) = 2\,\mathrm{am}\left(\xi\sqrt{\frac{F+\omega}{2EI}}, \frac{2}{1+\omega/F}\right), \tag{5.30}$$

and

$$\gamma^* = \mathrm{F}\left(\frac{\pi}{4}, \frac{2}{1+\omega/F}\right)\sqrt{\frac{2EI}{F+\omega}}. \tag{5.31}$$

5.2.6 Peel Strength

It is important to note that the solutions (5.30) and (5.31) are independent of the fiber length L but are only valid so long as $\gamma^* \leq L$. The largest value of $-F$ for which $\gamma^* \leq L$ is defined as the peel strength P of the fiber. This is the solution to

$$L = \mathrm{F}\left(\frac{\pi}{4}, \frac{2}{1-\omega/P}\right)\sqrt{\frac{2EI}{\omega-P}}. \tag{5.32}$$

Consider the limiting case when $P = 0$. According to (5.32), this occurs when

$$L \equiv \mathrm{F}\left(\frac{\pi}{4}, 0\right)\sqrt{\frac{2EI}{\omega}} = \frac{\pi}{2}\sqrt{\frac{EI}{2\omega}} =: L_{\mathrm{cr}}. \tag{5.33}$$

Hence, in order for a fiber to demonstrate adhesion under side contact (i.e. $\gamma^* \leq L$ for $F < 0$), its length must exceed the critical value L_{cr}.

When $L \gg L_{\mathrm{cr}}$, the elastic restoring forces become insignificant relative to ω. In this case, it follows from the Kendall peel model that the peel strength is approximately ω [46]. A plot of the normalized peel strength $\hat{P} := PL^2/EI$ versus normal work of adhesion $\hat{\omega} := \omega L^2/EI$ is presented in Figure 5.2. Also plotted is the limiting case $\hat{P} \approx \hat{\omega}$. This

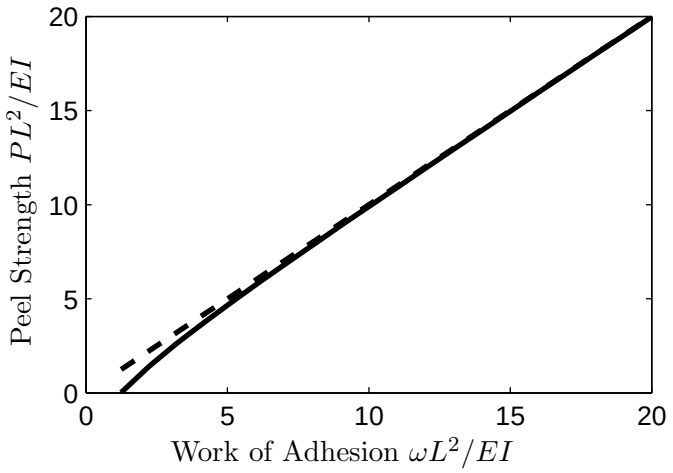

Figure 5.2. Peel strength of fiber in side contact; (solid) exact solution, (dashed) approximation valid for large $\omega L^2/EI$.

approximation appears to be accurate for $\hat{\omega} > 5$, which corresponds to a fiber length $L > 2L_{\rm cr}$.

In summary, the peel strength may be approximated as

$$P = \begin{cases} \omega & \text{if } L > L_{\rm cr} \\ 0 & \text{otherwise} \end{cases} \tag{5.34}$$

where $L_{\rm cr} = (\pi/2)\sqrt{EI/2\omega}$.

5.3 Side Contact with Lateral Constraint

The solutions (5.30) and (5.31) are based on the assumption that the base of the fiber is free to displace in the lateral, $\mathbf{e}_2$, direction. This assumption is valid if all the fibers have identical geometry and are in contact with a perfectly smooth and aligned flat.

In practice, however, different fibers will require a slightly different displacement at the base in order to accommodate side contact. Since fibers are mechanically coupled through a common support, they will be restricted to a single lateral displacement that

best accommodates average motions. This displacement is bounded by the extreme cases of a laterally unconstrained and a laterally constrained base, which are illustrated in Figure 5.3 [54].

5.3.1 Isoperimetric Constraint

For the case of a laterally constrained base, the fiber is subject to an isoperimetric constraint:

$$x = \int_0^L \sin\theta \, d\xi, \tag{5.35}$$

where the constant x is prescribed as the distance from the fiber tip to the base along $\mathbf{e}_2$. Initially, $x = 0$ but grows steadily as the fiber tip slides freely along the contacting substrate during preload (see Figure 5.3). When $\theta(L) = \pi/2$, the fiber begins to engage in side contact. At this point,

$$x = \frac{L\sqrt{2}}{\mathrm{K}\left(1/\sqrt{2}\right)} \approx 0.763L. \tag{5.36}$$

where $\mathrm{K}(\bullet)$ is the complete elliptic integral of the second kind [75].

During side contact, the interfacial forces are large and prevent the fiber tip from further sliding. Hence, the parameter x remains fixed at $0.763L$ for the remainder of loading. Therefore, (5.35) becomes

$$0.763L \equiv \int_0^L \sin\theta \, d\xi = \int_0^\gamma \sin\theta_\alpha \, d\xi + \int_\gamma^L \sin\theta_\beta \, d\xi \tag{5.37}$$

$\Rightarrow$

$$\int_0^\gamma \sin\theta_\alpha \, d\xi + 0.237L - \gamma = 0. \tag{5.38}$$

5.3.2 Governing Equations

The work necessary to maintain the isoperimetric constraint is calculated as

$$\int_0^L \lambda \sin\theta \, d\theta, \tag{5.39}$$

where the constant λ is an undetermined (Lagrange) multiplier. Following the method of Lagrange multipliers [50], the integrand is subsumed into the Lagrangian. Hence,

$$f_\alpha = F\cos\theta_\alpha + \frac{1}{2}EI(\theta_\alpha')^2 + \lambda\sin\theta_\alpha \qquad \text{and} \qquad f_\beta = -\omega + \lambda\sin\theta_\beta. \tag{5.40}$$

Substituting the Lagrangian density (5.40) into the Euler-Lagrange differential equation (5.14) implies

$$EI\theta_\alpha'' + F\sin\theta_\alpha - \lambda\cos\theta_\alpha = 0. \tag{5.41}$$

Similarly, substituting (5.40) into (5.16) yields the natural boundary condition (5.17). The boundary value problem (5.41,5.18) is solved numerically in *Matlab R2006a* (The MathWorks, Inc.) using a finite difference package. This yields a solution $\theta_\alpha = \theta_\alpha(\xi\,;\,\gamma,\lambda)$. Next, γ and λ are determined by simultaneously solving the boundary conditions (5.17) and (5.38).

5.3.3 Peel Strength

Let P denote the maximum allowable value of $-F$, which corresponds to $\gamma = L$. The normalized peel strength $\hat{P} = PL^2/EI$ is plotted versus $\hat{\omega} = \omega L^2/EI$ in Figure 5.4. Interestingly, the peel strength is about three times larger than for the unconstrained case. This is reasonable since the lateral constraint results in a smaller peel angle. The difference between the two cases is analogous to peeling a piece of sticky tape from its end (laterally

unconstrained) versus its center (laterally constrained). When peeled from its center, the peel angle is much smaller, resulting in a much larger peel resistance.

Another difference between the constrained and unconstrained case is that the laterally constrained rod exhibits side contact for $\hat{\omega}$ as low as 0.29. This corresponds to $L \approx L_{\text{cr}}/2$.

The values plotted in Figure 5.4 represent an upper bound on the true peel strength of individual fibers. A more accurate prediction for $\hat{P}$ is expected to lie somewhere in between this upper bound and the lower bound plotted in Figure 5.2.

5.4 Adhesion Coefficient

The coefficient of adhesion, μ', is defined as the ratio of pull-off strength P to preload W [12]:

$$\mu' = P/W. \tag{5.42}$$

The preload necessary to achieve side contact is $W = 1.3F_{\text{cr}}$, where

$$F_{\text{cr}} = \frac{\pi^2 EI}{4L^2} \tag{5.43}$$

is the critical buckling load for a cantilevered rod. This is equivalent to the axial force necessary to bend an elastica $pi/2$ radians. Hence, μ' is approximately $0.77\omega/F_{\text{cr}}$ and $2.3\omega/F_{\text{cr}}$ for the laterally unconstrained and constrained cases, respectively.

In the case of a laterally unconstrained base, side contact requires $L \geq L_{\text{cr}} = (\pi/2)\sqrt{EI/2\omega}$. Hence, F_{cr} will be on the order of 2ω and $\mu' \approx 0.4$. For the constrained base, L can be as small as $L_{\text{cr}}/2$, which corresponds to a much stiffer fiber and greater buckling load $F_{\text{cr}} \approx 8\omega$. This implies that $\mu' \approx 0.3$. So, despite the higher pull-off strength, the laterally constrained fiber can have a slightly lower coefficient of adhesion.

In contrast, isolated tokay setae exhibit values of μ' between 8 and 16 [4]. By this measure, natural setae will outperform nanofibers engaged in side contact by over a factor of twenty. This suggests that the side contact mechanism is less desirable for applications requiring *pressure sensitive* adhesion, in which bonding occurs through self-wetting or a light preload.

5.5 Comparison with Experimental Measurement

Consider an array of vertically aligned multiwalled carbon nanotubes of radius $R = 12.5$ nm, length $L = 40$ μm, elastic modulus $E = 200$ GPa, and density $D = 10^{14}$ m^{-2}. Assuming a Poisson's ratio of $\nu = 0.3$ and noting that $W_{\text{ad}} = 330$ mJ/m^2 [81], it follows from (5.12) that $\omega = 0.83$ nN. From Figures 5.2 and 5.4, the peel strength is approximated as ω and 3ω for the laterally unconstrained and constrained cases, respectively. Hence, 0.83 nN $\leq P \leq$ 2.5 nN and the total pull-off strength of the array, $\sigma := DP$, is in the range of 8.3 to 25 N/cm^2. [83] experimentally measure a normal strength of 10 N/cm^2, well within the theoretical range.

While the experimental results of [83] are consistent with theory, they measure a dramatic reduction in pull-off strength as the number of loading cycles increases. After seven cycles, the bond strength falls to 3 N/cm^2. This may be due to clumping and entanglement, which increase as the fibers contact each other during each loading cycle. As discussed in [53], clumping can be avoided by setting the fiber density below a critical value D_{cr}. This is considered in formulating the design principles for VANF arrays.

Another disadvantage of the MWCNT arrays is the high preload required for attachment. Samples ranging in area from 4 to 8 mm^2 required close to 2 kg of preload. This

corresponds to values of μ' between 0.02 and 0.04, a factor of ten less than is theoretically expected. One explanation is that the samples were preload more than necessary to achieve adhesion. Another possibility is that because the fiber density exceeded $D_{\rm cr}$, a greater amount of preload was necessary to break apart fiber clumps.

5.6 Design Principles for Side Contact

In the preceding sections it has been shown that side contact is only possible when L is at least on the order of $L_{\rm cr}$. Moreover, the peel strength is on the order of ω. Hence, for fiber density D, the strength of the fiber array is approximately

$$\sigma = D\omega. \tag{5.44}$$

However, according to the theory and experimental results presented in [53], D is limited by the critical value

$$D_{\rm cr} = \frac{1}{(2R + \Delta_{\rm cr})^2} \tag{5.45}$$

where

$$\Delta_{\rm cr} := \frac{{L_{\rm cr}}^2}{3}\sqrt{\frac{2\omega}{EI}} = \frac{\pi^2}{12}\sqrt{\frac{EI}{2\omega}}. \tag{5.46}$$

This assumes that the fibers are square packed with an outer-wall spacing of $\Delta_{\rm cr}$. If D is greater than $D_{\rm cr}$, then the bond strength will degrade over loading cycles due to fiber clumping, as demonstrated in [83]. An exception is the case of rough fibers, which have a lower effective work of adhesion on account of nanosized surface asperities and reduced interfacial contact. Such roughness allows for closer spacing but decreases peel strength and necessitates more slender fibers for side contact. From equations (5.12) and (5.44-5.46) it follows that the total bond strength will decrease with reduced effective $W_{\rm ad}$, as caused by roughness on the fiber surface.

For a typical polymer, $W_{\text{ad}} = 30$ mJ/m^2 and $\nu = 1/3$. The maximum bond strength, $\sigma = D_{\text{cr}}\omega$ is plotted in Figure 5.5 for various values of R and E. For stiff polymers ($E \geq 1$ GPa), $\sigma > 1$ N/cm^2 only for $R < 10$ nm. Nonetheless, adhesion on the order of 1 N/cm^2 has been observed with an array of 200 nm diameter, 60 μm long polyimide ($E = 3$ GPa) fibers. However, adhesion is limited to only one loading cycle, after which the fibers collapse into large clumps.

For VACNT arrays ($E = 200$ GPa, $\nu = 0.3$, $W_{\text{ad}} = 330$ mJ/m^2), the radius ranges from 5 to 15 nm. Following from Figure 5.5, σ is between 0.6 and 0.03 N/cm^2, much lower than for the structure studied by [83]. These estimates correspond to densities of $D_{\text{cr}} = 1.3\times10^{13}\text{m}^{-2}$ and $3.4\times10^{11}\text{m}^{-2}$, respectively. Unlike the higher density structures of [83] ($D = 10^{14}\text{m}^{-2}$), these arrays are unlikely to clump and will thus maintain their adhesion over multiple loading cycles.

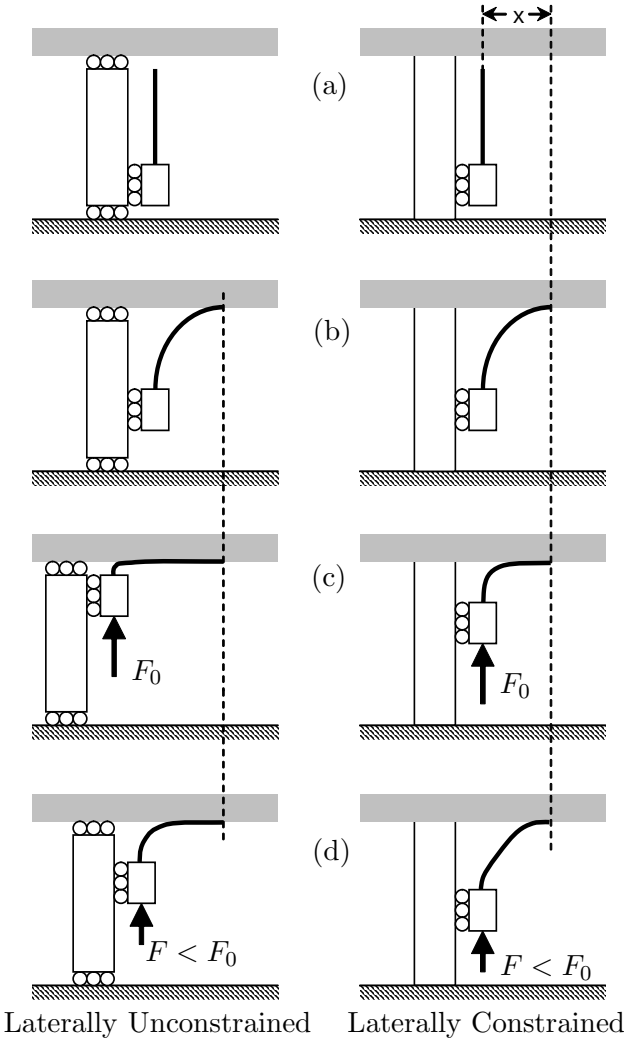

Figure 5.3. Loading cycle and qualitative fiber shapes for a fiber completely clamped to a laterally unconstrained and laterally constrained support. (a) Initial configuration (b) Fiber tip at angle $\pi/2$, side contact begins, tip no longer slides relative to opposing substrate (c) Maximum value of preload F_0 (d) Preload relaxed to a final load F, which can be negative.

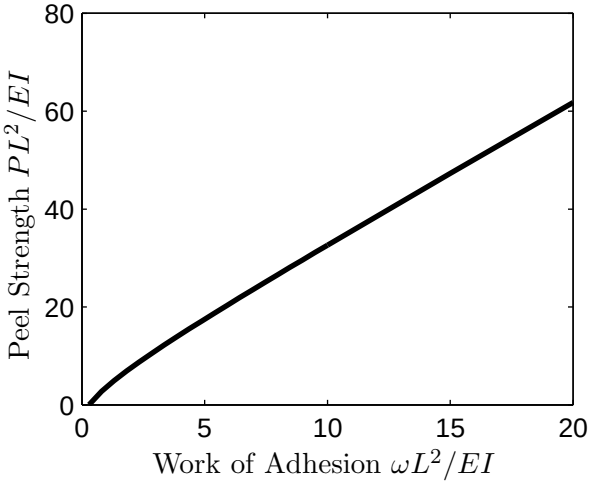

Figure 5.4. Peel strength of fiber in side contact with lateral constraint.

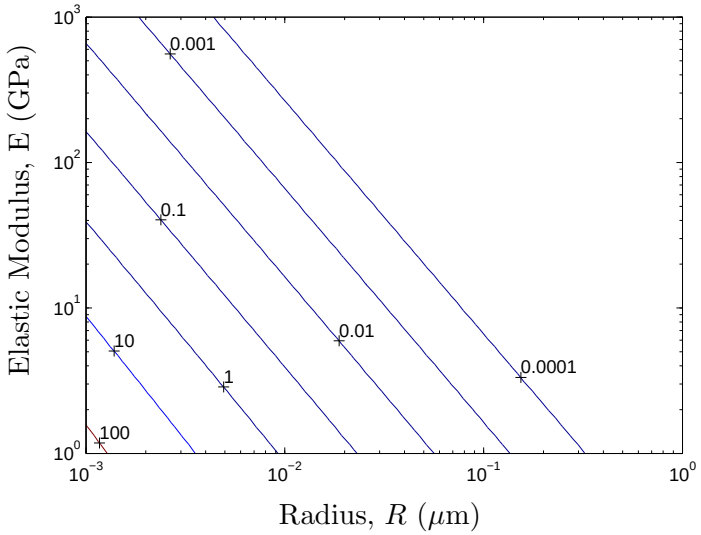

Figure 5.5. Bond strength for optimally packed, non-clumping VANF array (N/cm^2); W_{ad} = 30 mJ/m^2 and $\nu = 1/3$.

Chapter 6

Ultrahigh Friction with Microfibers

In addition to adhesion, synthetic fiber arrays are capable of high friction. This was recently demonstrated with arrays of vertically aligned microfibers (VAMF) made from polypropylene [56]. As shown in Figure 1.1, an array of 0.3 μm radius fibers is capable of suspending a U.S. quarter dollar on an 82 degree glass incline.

Although these structure exhibit incredible friction, several orders of magnitude higher than for a smooth material, they do not adhere under pure tensile loading. This property can be advantageous since adhesion results in energy loss and the formation of wear particles. Specific applications for high friction / low adhesion materials include transmission systems, brakes, tires, and shoes.

Let the coefficients μ and $\hat{\mu}$ denote the ratio of shear resistance to applied load for smooth surfaces and fiber arrays, respectively. For most materials, $\mu < 1$ and is typically close to 0.3. Recent work with VACNT arrays has shown $\hat{\mu} = 0.795$ on glass [19] and $\hat{\mu} =$

2.2 on a 20 μm radius gold sphere [47]. As presented in this work and in [56], polypropylene VAMF arrays can exhibit a coefficient of friction $\hat{\mu} > 10$.

6.1 Experimental Work

VAMF arrays were fabricated and tested in the Biomimetic Milli-Systems Laboratory at the University of California, Berkeley. Below are descriptions of the fabrication process, experimental procedure, and results. These details are also presented in [56].

6.1.1 Fabrication

Arrays of polypropylene microfibers were synthesized by casting one layer of 25.4 μm thick polypropylene film (TF-225-4, Premier Lab Supply Inc.) into a 20 μm thick polycarbonate filter (ISOPORE, Millipore Inc.) of 0.3, 0.6, or 2.5 μm pore radius. The film and filter were placed in a stack along with a 5 $\times$ 7.6 cm glass slide, a 5 $\times$ 7.6 cm slab of silicone rubber, a 0.6 $\times$ 3.8 $\times$ 8.3 cm brass plate (167 grams), and a 3.8 cm diameter, 5.1 cm long brass cylinder (492 grams). These were stacked in the order shown in Figure 6.1.

The stack was placed in a vacuum oven for 25 minutes at 200 ^{o}C. To dissolve the embedded polycarbonate filter, the polypropylene sheet was immersed in a beaker of methylene chloride on a spin plate. After five minutes of agitation, the sheet was transferred to a second beaker, which was agitated on the spin plate for an additional ten minutes. Next, the sheet was rinsed in isopropyl alcohol and air dried.

As shown in Figure 6.2, an array of 0.3 μm radius fibers exhibits several microns of fiber length variation and only a slight amount of clumping. Clumping is absent in the 0.6 μm and 2.5 μm radius samples that were tested.

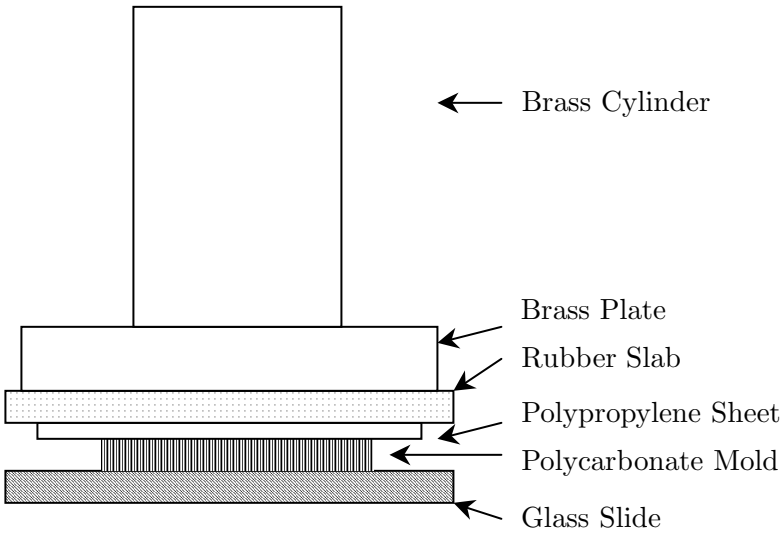

Figure 6.1. Stacking order for fabrication of polypropylene VAMF array.

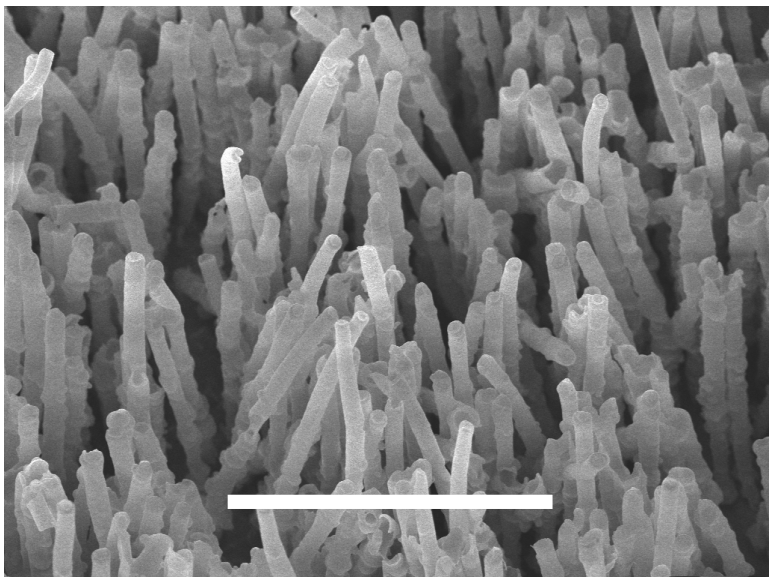

Figure 6.2. SEM of an array of 20 μm long, 0.6 μm diameter polypropylene fibers etched from a polycarbonate membrane; scale bar represents 10 μm.

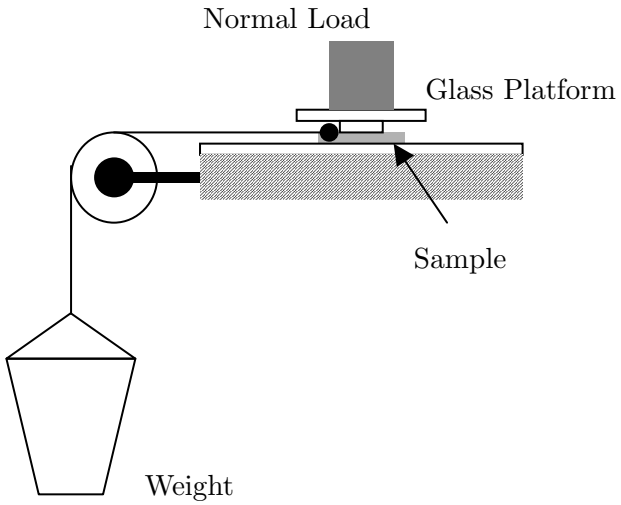

Figure 6.3. Pulley apparatus for measuring coefficient of friction of a VAMF array.

6.1.2 Testing Procedure

Static friction measurements were performed on a traditional pulley apparatus, where the sample was loaded in shear by a string run over a pulley to a hanging weight. The polypropylene sample was placed on an acetone-cleaned glass slide and subject to a constant normal load by a brass weight on a rigid flat platform. The shear load was increased until first sliding was observed. An illustration of the testing apparatus is presented in Figure 6.3.

Experiments were performed on arrays of 0.3, 0.6, and 2.5 μm radius polypropylene fibers as well as two types of controls. One control was the unprocessed 25.4 μm thick polypropylene film and the other was processed film that underwent the same fabrication steps as the fiber arrays with the exception that no polycarbonate mold was included in the vacuum bake.

Normal pressures of 0.17 to 0.79 N/cm^2 were obtained by placing 20, 50 and 100 grams weights on a 1.3 cm diameter glass platform. Five measurements were performed on three distinct samples for each load and array type. Higher pressures of up to 16.5 N/cm^2 were obtained by placing weights on a platform with three legs attached to squares of glass coverslip. The combined area of the three squares was 0.033 cm^2. In this case five measurements were performed on a single sample for each load and array type.

6.1.3 Results

As shown in Fig. 6.4, high friction was observed in arrays of 0.3 μm radius polypropylene fibers over pressures of 0.17 to 0.79 N/cm^2. Under 0.79 N/cm^2 normal stress, the 0.3 μm radius polypropylene fiber arrays had an average friction coefficient of $\hat{\mu} = 5.3$ (sample

size = 15). The friction coefficient $\mu = 0.3$ for the processed control was similar to that measured in other experiments of polypropylene on smooth glass [32], [65].

The experimental results suggest that altering the surface geometry of polypropylene can increase the coefficient of friction by an order of magnitude. This phenomenon is consistent with an adhesion theory of friction, in which shear resistance V has an affine relationship with the real area of contact A_r [66]. Due to the high elastic modulus of polypropylene (E = 1 GPa), the real area of contact for a nominally smooth control will be negligible. A fiber array, however, will exhibit high compliance due to fiber buckling and bending, thus enabling substantial interfacial contact even under low normal loads.

The adhesion theory may also explain why, under high pressure, shear resistance is greatest with the $R = 0.6$ μm arrays. This is evident in Fig. 6.4 for a compression of 16.5 N/cm^2. Based on image processing of the polycarbonate filters, these arrays were found to have a higher area fraction (25%) than the $R = 0.3$ μm (12%) or $R = 2.5$ μm (6%) arrays. That is, for higher loads when all fibers are in contact, the $R = 0.6$ μm arrays achieve a larger contact area and thus exhibit a greater shear resistance.

6.2 Theory of VAMF Friction

For a micro-rough substrate and/or small variations in fiber length, only a fraction of the fibers will be in contact under a small total normal load F. Fiber compliance is modeled using an ideal elastic column with a critical buckling load [42]. The fiber compliance is highly dependent on the slip condition at the contact [8]. For non-slip contact, the fiber is constrained to deform in a clamped-pinned or clamped-clamped mode and will be several times more stiff than a fiber under clamped-free loading.

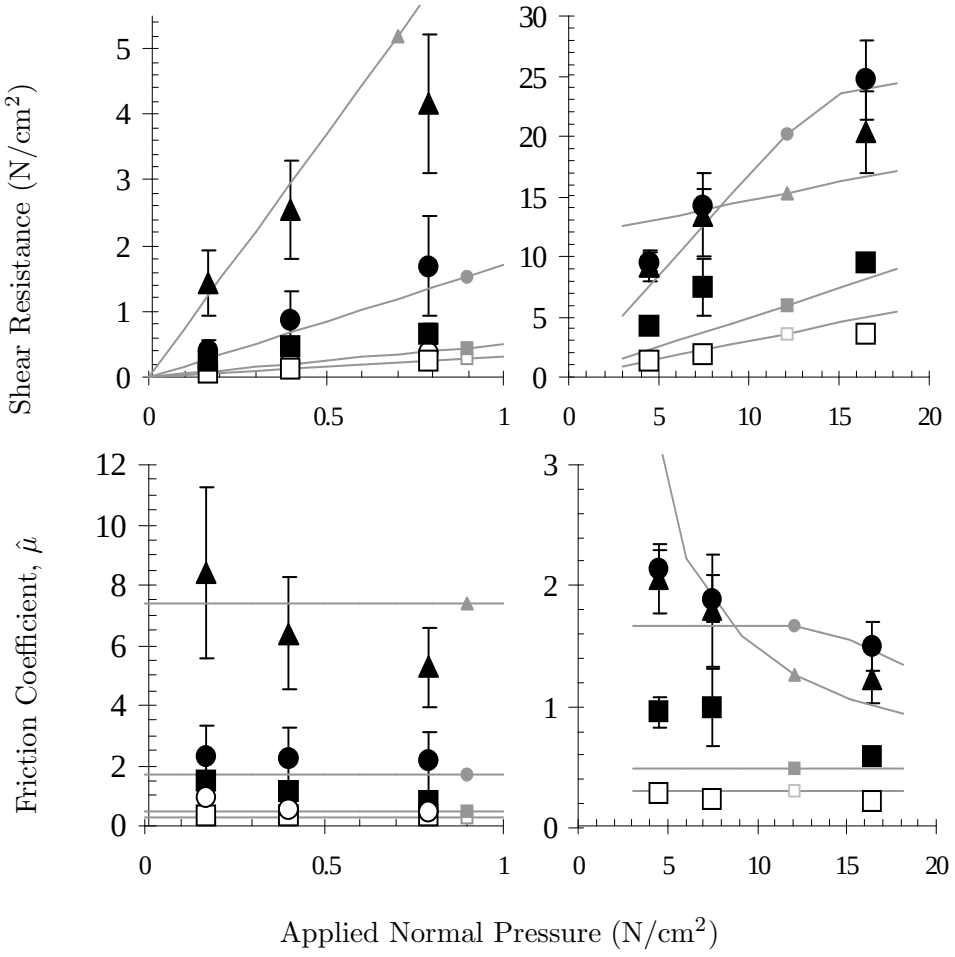

Figure 6.4. Plot of normal pressure versus shear resistance for polypropylene fiber arrays and controls; (▲) radius $R = 0.3$ μm, (●) $R = 0.6$ μm, (■) $R = 2.5$ μm, (○) unprocessed control, (□) processed control; (left) loading area = 1.27 cm^2, sample size = 15; (right) loading area = 0.033 cm^2, sample size = 5; error bars represent one standard deviation in the data; solid lines represent theoretical predictions from equations (6.6), (6.7), and (6.12) for $R_t = 3R$.

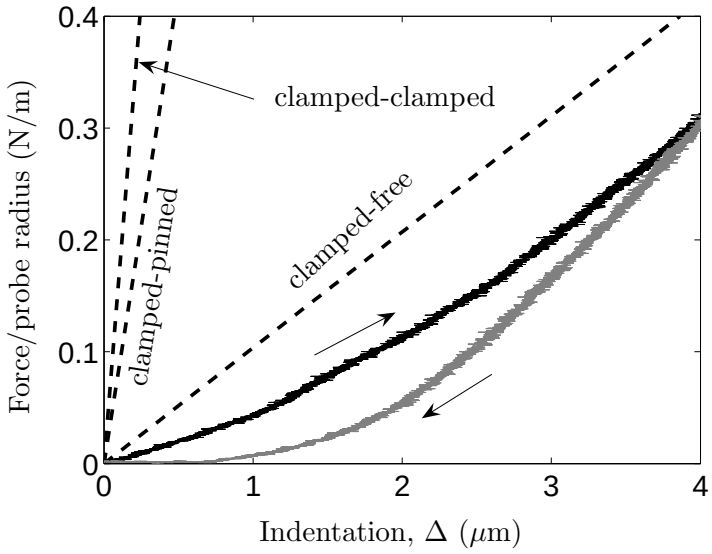

Figure 6.5. Mechanical response of $R = 0.3\mu$m fiber array indented by a spherical probe (radius = 5.17 cm); greater compliance at low Δ may be a result of fiber sparsity near the top of the array due to length variation; $(--)$ theoretical predictions based on ideal column buckling for various buckling modes; arrows indicate loading direction.

6.2.1 Array Compliance

A comparison of the theoretical force response for the various deformation modes of an $R = 0.3\mu$m fiber array is presented in Figure 6.5. Here, a 5.17 cm radius probe is pressed into the array by a distance Δ. Noting that the radius of contact is small relative to the probe radius, the force response is approximately

$$F = 2\pi p \rho F_{\text{cr}} \Delta, \tag{6.1}$$

where p is the probe radius, $\rho = 42 \times 10^6 \text{cm}^{-2}$ is the fiber density, and F_{cr} is the critical buckling load. In general [28],

$$F_{\text{cr}} = K \frac{\pi^2 EI}{L^2} \tag{6.2}$$

where K is a geometric factor that depends on the buckling mode, $E = 1$ GPa is the elastic modulus, $I = \pi R^4/4$ is the area moment of inertia, and $L = 20$ μm is the fiber length. For

clamped-free loading, in which the fiber tip can slide freely with respect to the contacting substrate, $K = 1/4$ and so $F_{cr} = 39$nN.

Also plotted in Figure 6.5 is a typical force response obtained experimentally using an optical force sensor. Among the various column buckling models, the clamped free mode most closely matches the measured response. At lower indentations, however, it overestimates the stiffness. This may be a result of fiber length variation, which causes the array to be more sparse at heights close to 20μm. Regardless, the clamped-free buckling model will be adopted for the remaining analysis, as it produces the best estimate for the mechanical response.

6.2.2 Coefficient of Friction, $\hat{\mu}$

Under a light normal load F, it follows that for an array of ideal elastic columns, the number of contacts will be approximately

$$N = \frac{F}{F_{\text{cr}}}\,. \tag{6.3}$$

With the addition of shear load, N should be slightly greater due to the enhanced compliance of columns under compound loading, but this difference is assumed to be negligible.

By Coulomb's law, the shear resistance from each contact will be

$$V_f = \mu F_{\text{cr}} + \tau A_f, \tag{6.4}$$

where $\tau \approx 10$ MPa [65] [32] is the interfacial shear strength per unit area and A_f is the real area of contact for the fiber. Since the applied load F_{cr} is constant with respect to F, A_f is also likely to be constant. The shear resistance of an entire array is

$$V = V_f N, \tag{6.5}$$

Load (N/cm^2)	Radius (μm)	ρ (cm^{-2})	$\hat{\mu}$	A_r (mm^2)	A_f (μm^2)	A_{JKR} (μm^2)	f
0.79	0.3	42×10^6	5.3	0.5	0.02	0.028	0.48
	0.6	22×10^6	2.1	0.18	0.11	0.086	0.057
	2.5	0.42×10^6	0.81	0.05	9.7	3.6	0.001
16.5	0.3	42×10^6	1.2	0.049	0.035	0.028	1.0
	0.6	22×10^6	1.5	0.065	0.089	0.086	1.0
	2.5	0.42×10^6	0.58	0.015	5.3	3.6	0.20

Table 6.1. Estimated contact areas for polypropylene fiber arrays; ρ is the fiber density, f is the estimated fraction of fibers buckled in the clamped-free mode (K = 1/4).

and so substituting the expressions for N and V_f, it follows that

$$V = \hat{\mu}F \quad \text{and} \quad \hat{\mu} = \mu + \tau A_f/F_{\text{cr}}. \tag{6.6}$$

Interestingly, $(6.6)_1$ resembles Amontons' law with $\hat{\mu}$ as an effective coefficient of friction.

The ideal column model implies complete contact when the applied load exceeds $F_{\text{cr}}N_0$, where N_0 is the total number of fibers inside the contact area. In this case,

$$\hat{\mu} = \mu + \tau N_0 A_f/F, \quad (F > F_{\text{cr}}N_0) \tag{6.7}$$

and A_f can no longer be approximated as constant. Since N_0A_f is bounded above by the apparent area of contact, (6.7) implies that $\hat{\mu}$ should asymptotically approach μ with increasing load F. The reduction in $\hat{\mu}$ with increasing F is apparent in Figure 6.4 and Table 6.1.

6.3 Comparison of Theoretical and Experimental Results

Table 6.1 compares the response of various structures to two different compressive loads: 0.79 N/cm^2 over 1.27cm^2 and 16.5 N/cm^2 over 0.033 cm^2. Based on the model, the real area of contact A_r is given by

$$A_r = F(\hat{\mu} - \mu)/\tau. \tag{6.8}$$

The fraction of fibers that are buckled (and in contact) is evaluated as

$$f = \frac{N}{N_0}, \tag{6.9}$$

where

$$N = \min\{\, F/F_{\rm cr}\,,\, N_0\,\}, \tag{6.10}$$

and the average contact area per fiber is

$$A_f = A_r/N. \tag{6.11}$$

Under 0.79 N/cm^2 compression, only a minority of fibers are buckled in each of the three fiber arrays. The effective coefficient of friction $\hat{\mu}$ is highest when operating in this regime. With a higher compressive load of 16.5 N/cm^2, all fibers in the R = 0.3 μm and R = 0.6 μm arrays buckle under a force of approximately F/N_0. In this case, the load controlled friction, $\mu(F/N_0)$ is expected to overshadow the adhesion term $\tau A_f/F_{\rm cr}$, leading to the observed drop in $\hat{\mu}$.

The estimates for A_f are compared to JKR theory [44], which predicts a contact area of

$$\begin{aligned} A_{\rm JKR} \;=\; & \pi\Big[\frac{3(1-\nu^2)R_t}{4E}\Big(F_{\rm cr} + 3\pi W_{\rm ad} R_t \\ & + \sqrt{6\pi W_{\rm ad} F_{\rm cr} R_t + (3\pi W_{\rm ad} R_t)^2}\Big)\Big]^{2/3}, \end{aligned} \tag{6.12}$$

where R_t is the fiber tip radius of curvature, ν is Poisson's ratio and W_{ad} is the interfacial work of adhesion. It is assumed that $\nu = 0.3$ and $W_{\rm ad} = 75$ mJ/m^2 [56].

Table 6.1 presents values for $A_{\rm JKR}$ based on the assumption $R_t = 3R$, as this provides a reasonable fit to the data and approximates the blunted shape of the tips. When $f = 1$, $F_{\rm cr}$ is replaced by F/N_0 in evaluating (6.12). Theoretical predictions for $\hat{\mu}$ based on (6.6),

(6.7), and (6.12) for $R_t = 3R$ are plotted along with the experimental results in Fig. 6.4. It is important to note that observations under SEM clearly indicate that the fiber tips are not rounded and so JKR theory may not be applicable.

6.4 Concluding Remarks

In summary, a microcasting process has been shown to transform a low friction material ($\mu = 0.3$) into a high friction structure ($\hat{\mu} > 5$). This property is achieved by molding polypropylene into an array of microfibers, resulting in a compliant structure that allows significant interfacial contact even under light pressure. Friction enhancement through increased compliance is consistent with an adhesion theory of friction. A quantitative prediction for the enhanced coefficient of friction $\hat{\mu}$ is obtained by treating the fibers as ideal elastic columns subject to Coulomb's friction law.

While VAMF arrays exhibit high friction, they are not capable of adhesion. In order to accommodate displacements in the tensile directions, fibers must *stretch*. Such a deformation mode is energetically costly and results in poor tensile compliance and thus poor load sharing among fibers during array detachment. Tensile compliance can be introduced by angling or curving the fibers such that they can bend under tension. Adhesion of curved fibers is studied in the next chapter (Chapter 7).

Chapter 7

Adhesion with Curved Microfibers

With the exception of an isolated measurement presented in [26], normal adhesion has yet to be reliably observed over large contact area with an array of stiff (E $\geq$ 1 GPa), vertically aligned, micro fibers (VAMF). As discussed in the previous chapter (Chapter 6), this is partly due to poor tensile compliance since under tension the fibers must stretch in order to overcome surface roughness and/or fiber length variation. For displacements that are typically on the order of microns or several hundred nanometers, the elastic restoring force caused by stretching far exceeds the bond strength of the tip-substrate interface. Thus, during normal pull-off, fibers will detach one-by-one, resulting in a cascade of bond failures.

Tensile compliance is introduced by curving the fibers into an arc. In this way, fibers will *bend* rather than stretch out of their natural configuration. Because the elastic restoring forces associated with bending are low, multiple fibers can remain in contact as they are pulled from a microrough surface. The combined tensile resistance leads to a significant strength of adhesion. Moreover, because the fibers are composed of stiff materials, such as large elastic modulus polymer and metals, it has the potential for high wear and temperature resistance and possibly even self-cleaning.

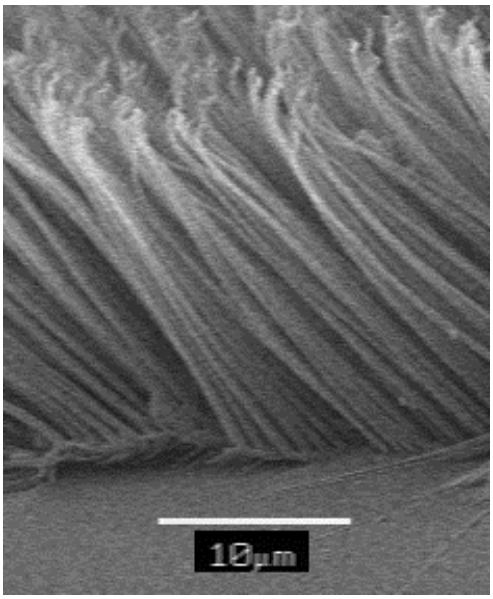

Figure 7.1. SEM image of the setal array for *Anolis Equestris*.

This chapter introduces design principles and fabrication methods for developing an array of naturally curved fibers. Adhesion is experimentally measured with a spherical probe apparatus and preliminary results are compared to theoretical predictions.

7.1 Biological Inspiration

Interestingly, curved microfibers resemble the setal array on the digits of *Anolis* lizards. As shown in Figure 7.1, each setal stalk is approximately 20 μm long, 0.6 μm in diameter, and terminates into a single spatular flap. As is typical among wall-climbing lizards, the spatulae have thickness $\sim$ 10 nm, and a length and width of roughly 0.3 μm.

Due to its lack of spatular branching, the adhesive system of the Anolis lizard is simpler for engineers to mimic. However, as discussed in Section 7.7, spatular branching may actually be necessary for robust adhesion. Indeed, current experimental work on Anolis "adhesion" has been limited to friction tests on an inclined surface [39] [40] [78] [13]. [39]

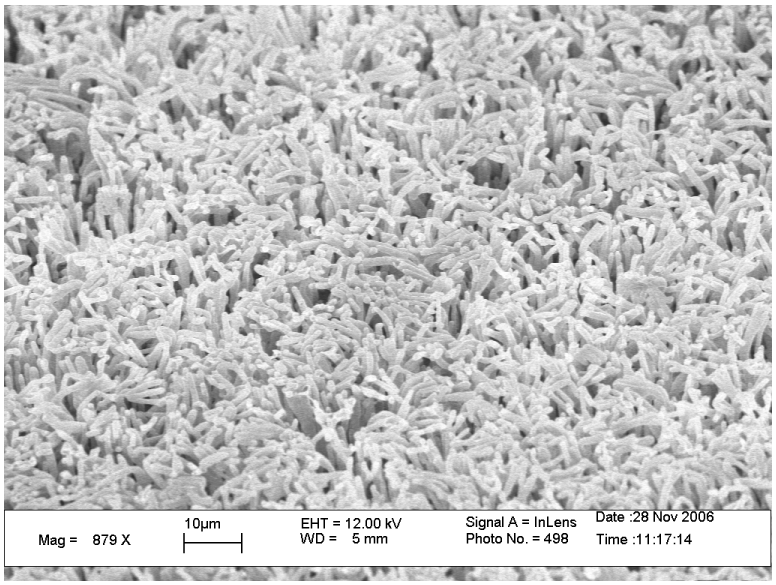

Figure 7.2. SEM image of curved, 0.4 μm radius, 20 μm polypropylene fibers. Estimated density $D = 50{\times}10^6\text{cm}^{-2}$.

and [13] measured the sliding resistance of a whole lizard on a smooth sheet of acetate transparency inclined at 85^o. Despite the smoothness of the substrate, the claws accounted for most of the resistance – clipping the claws of two digits on each forelimb resulted in a dramatic 60 % reduction in sliding friction [13].

Further study of anolis wall-climbing will be important towards the progress of synthetic setal arrays for adhesion. Of particular interest is the clinging ability of lizards to purely vertical surfaces. Other helpful studies include adhesion measurements on smooth, rigid surfaces such as glass. Anolis lizards struggle on vertical glass although this may be caused by a poor choice of locomotion strategy rather than the inability of their setae to adhere.

7.2 Experimental Work

Arrays of polypropylene microfibers were synthesized by casting one layer of 25.4 μm thick polypropylene film (TF-225-4, Premier Lab Supply Inc.) into a 20 μm thick polycar-

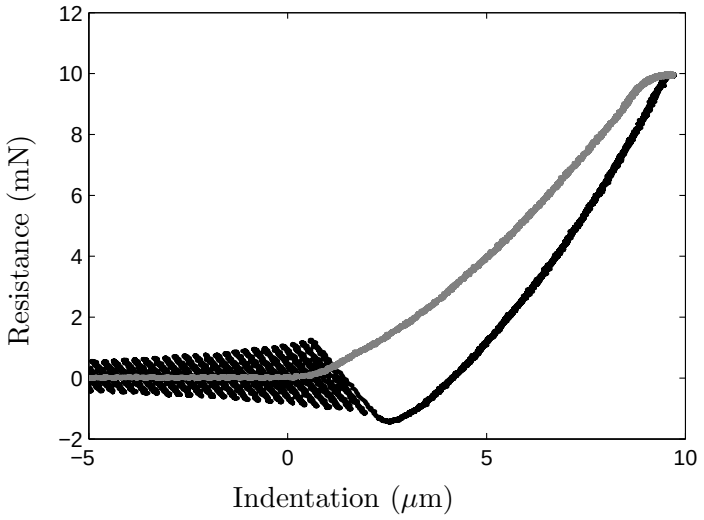

Figure 7.3. Force response to indentation with 5.17 cm sphere. Curved polypropylene fibers of radius, $R = 0.4$ μm and length $L = 20$ μm. Estimated density $D = 50{\times}10^6 \mathrm{cm}^{-2}$

bonate filter (ISOPORE, Millipore Inc.) of 0.4 μm pore radius. Prior to casting, however, the filter was capped on one side with a film of polystyrene. First, a solution of polystyrene and toluene prepared by researchers in the Maboudian Group (Department of Chemical Engineering, UC Berkeley) was spun coat onto a clean, 5 $\times$ 7.6 cm glass slide. The first spin cycle was for 6 seconds at 2000 rpm followed by a second cycle for 20 seconds at 3500 rpm. Next, the coated slide was left to air dry for several minutes. A polycarbonate filter was then placed onto the coated slide and wetted with toluene using a cotton swab. Care was taken not to allow the swab to directly contact the polystyrene coating.

Leaving the filter on the coated slide, the filter was next covered with the polypropylene sheet, a 5 $\times$ 7.6 cm slab of silicone rubber, two 0.6 $\times$ 5 $\times$ 8.3 cm brass plates (225 grams), and two side-by-side 3.8 cm diameter, 6.5 cm long brass cylinders (615 grams). These were stacked in the order shown in Figure 6.1.

The stack was placed in a vacuum oven for 25 minutes at 200 ^{o}C. To dissolve the embed-

ded polycarbonate filter, the polypropylene sheet was immersed in a beaker of methylene chloride on a spin plate. After five minutes of agitation, the sheet was transferred to a second beaker, which was agitated on the spin plate for an additional ten minutes. Next, the sheet was rinsed in isopropyl alcohol and air dried.

To curve the fibers, the filter was cut into a 1 cm wide slice. The slice was then placed between two 1 mil sheets of steel shim and passed through a laminator (Catena 35, General Binding Corporation) at 180 ^{o}F and speed setting 1. This last step was repeated for 250 ^{o}F.

As shown in Figure 7.2, the fibers do not appear significantly clumped. Moreover, they are curved over with a radius of curvature on the order of the fiber length. This natural curvature allows the fibers to exhibit tensile compliance and hence greater load sharing during pull-off. The mechanical response to indentation with a spherical probe of radius 5.17 cm is plotted in Figure 7.3. Unlike for the VAMF array (Figure 6.5), the curved fibers exhibit adhesion. Adhesion corresponds to negative values for the indentation force and is shown to be as large as 1.5 mN.

7.3 Tip-Substrate Interaction

As discussed in Chapters 4 and 6, friction between the fiber tip and substrate can influence the force-displacement relationship. In the case of inclined setal stalks (Chapter 4), it was determined both theoretically and experimentally that friction against the natural orientation resulted in a "stiffening" of the array. Likewise, it was demonstrated in Figure 6.5 that "pinning" the tip to the substrate increases the stiffness by over a factor of eight.

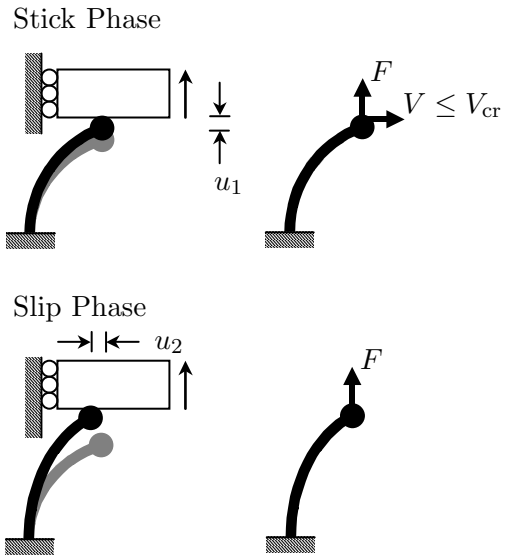

Figure 7.4. Free body diagram of curved fiber in stick and slip phases.

In studying the mechanics of curved microfibers it is important to consider the possible role of sliding resistance at the tip-substrate interface.

The most tractable model for tip-substrate interaction is *stick-slip*. Under low shear loads, V, the tip remains fixed, i.e. *sticks*, with respect to the substrate. When the elastic restoring force exceeds the shear strength V_{cr} of the tip-substrate interface, the tip slides freely, i.e. *slips*, along the surface. After the fiber deforms to its equilibrium configuration under zero shear load, the tip sticks again to the substrate. This process is illustrated in Figure 7.4. Fiber mechanics during the stick and slip phases are studied in Sections 7.4.1 and 7.4.2 respectively. The complete model for stick-slip contact is presented in Section 7.4.3.

Under tension, the fiber typically enters a slip phase as the normal load f approaches the JKR pull-off strength p. During slip, however, it has been shown that detachment occurs at a critical load $f_0 < p$ [43]. This critical load may be expressed as $f_0 = \alpha p$, where the

constant $\alpha \in [0, 1]$. Linear elastic fracture mechanics suggests that $\alpha = 0.75$ [43], although there is empirical evidence that α may be as large as 0.89 [17].

7.4 Stick-Slip Model

Adopting the same Euclidean coordinate system as in the previous chapters, let

$$\mathbf{F} = F\mathbf{e}_1 + V\mathbf{e}_2. \tag{7.1}$$

denote the interfacial load acting on the tip of the fiber. Treating the fiber as an elastica,

$$\theta''(\xi) = \frac{F}{EI}\sin\theta - \frac{V}{EI}\cos\theta, \tag{7.2}$$

where the arc length ξ convects with the fiber and the slope $\theta = \theta(\xi; F, V)$ is defined with respect to $\mathbf{e}_1$. The configuration θ is subject to the boundary conditions

$$\theta(0) = \theta_0(0) \qquad \text{and} \qquad \theta'(L) = 0, \tag{7.3}$$

where L is the fiber length and $\theta_0 = \theta_0(\xi)$ is the natural (undeformed) slope of the fiber.

For a naturally curved fiber,

$$\theta_0 = \frac{\xi}{\rho}, \tag{7.4}$$

where ρ is the radius of curvature. Let

$$\delta\theta := \theta - \theta_0 \tag{7.5}$$

be the change in slope from the reference configuration. Following from the boundary conditions (7.3)

$$\delta\theta(0) = 0 \qquad \text{and} \qquad \delta\theta'(L) = 0. \tag{7.6}$$

For $|\delta\theta| < \pi/12$, the vertical and horizontal positions of the fiber tip are approximately

$$x_1 = \int_0^L \{\cos\theta_0 - \delta\theta\sin\theta_0\}\, d\xi \qquad \text{and} \qquad x_2 = \int_0^L \{\sin\theta_0 + \delta\theta\cos\theta_0\}\, d\xi. \tag{7.7}$$

Prior to loading, the natural positions are

$$X_1 = \int_0^L \cos\theta_0 \, d\xi \qquad \text{and} \qquad X_2 = \int_0^L \sin\theta_0 \, d\xi. \tag{7.8}$$

7.4.1 Stick Phase

During the stick phase, both x_1 and x_2 are prescribed. Thus, $\delta\theta$ must satisfy the four equations in (7.6) and (7.7). It is convenient to assume that such a solution is *unique*. Thus $\delta\theta = \delta\theta(\xi)$ may be represented by the polynomial

$$\delta\theta = \alpha + \beta\xi + \kappa\xi^2 + \lambda\xi^3 \tag{7.9}$$

where the constants α, β, κ, and λ are determined by solving the equations in (7.6) and (7.7).

Following from (7.6),

$$\alpha = 0 \qquad \text{and} \qquad \beta = -2\kappa L - 3\lambda L^2. \tag{7.10}$$

Thus, $\delta\theta$ becomes

$$\delta\theta = \kappa(\xi^2 - 2\xi L) + \lambda(\xi^3 - 3\xi L^2). \tag{7.11}$$

Solving (7.7) for κ and λ reduces to solving the system of linear equations,

$$\begin{aligned} u_1 &= a_1\kappa + b_1\lambda \\ u_2 &= a_2\kappa + b_2\lambda \end{aligned} \tag{7.12}$$

where

$$\begin{aligned} a_1 &= -\int_0^L (\xi^2 - 2\xi L)\sin\left(\frac{\xi}{\rho}\right) d\xi = -\rho\left(L^2 + 2\rho^2\right)\cos\left(\frac{L}{\rho}\right) + 2\rho^3 \\ a_2 &= \int_0^L (\xi^2 - 2\xi L)\cos\left(\frac{\xi}{\rho}\right) d\xi = -\rho\left(L^2 + 2\rho^2\right)\sin\left(\frac{L}{\rho}\right) + 2L\rho^2 \end{aligned}$$

$$
\begin{aligned}
b_1 &= -\int_0^L (\xi^3 - 3\xi L^2)\sin\left(\frac{\xi}{\rho}\right)\, d\xi \\
&= -2L\rho\left(L^2+3\rho^2\right)\cos\left(\frac{L}{\rho}\right) + 6\rho^4\sin\left(\frac{L}{\rho}\right) \\
b_2 &= \int_0^L (\xi^3 - 3\xi L^2)\cos\left(\frac{\xi}{\rho}\right)\, d\xi \\
&= -6\rho^4\cos\left(\frac{L}{\rho}\right) + 3\rho^2\left(L^2+2\rho^2\right) - 2\rho L\left(L^2+3\rho^2\right)\sin\left(\frac{L}{\rho}\right) \\
u_1 &= x_1 - \int_0^L \cos\left(\frac{\xi}{\rho}\right)\, d\xi = x_2 - \rho\sin\left(\frac{L}{\rho}\right) \\
u_2 &= x_1 - \int_0^L \sin\left(\frac{\xi}{\rho}\right)\, d\xi = x_1 - \rho + \rho\cos\left(\frac{L}{\rho}\right). \qquad (7.13)
\end{aligned}
$$

This yields

$$
\kappa = \frac{b_2u_1 - b_1u_2}{a_1b_2 - a_2b_1} \qquad \text{and} \qquad \lambda = \frac{a_2u_1 - a_1u_2}{a_2b_1 - a_1b_2}. \qquad (7.14)
$$

The total elastic strain energy in the rod is

$$
\begin{aligned}
U_{el} = \hat{U}(x_1,x_2) &= \int_0^L \frac{1}{2}EI\left(\delta\theta'\right)^2\, d\xi \\
&= \frac{1}{30}EIL^3\left(20\kappa^2 + 75\kappa\lambda + 72l^2\lambda^2\right), \qquad (7.15)
\end{aligned}
$$

where E is the elastic modulus, $I = \pi R^4/4$ is the area moment of inertia, and R is the fiber radius. The elastic restoring forces V and F are related to the elastic strain energy through the constitutive laws:

$$
\begin{aligned}
F &= \frac{\partial\hat{U}}{\partial x_1} = \frac{1}{6}EIL^3(8\kappa + 15L\lambda)\frac{\partial\kappa}{\partial x_1} + \frac{1}{10}EIL^4(25\kappa + 48L\lambda)\frac{\partial\lambda}{\partial x_1}, \qquad (7.16) \\
V &= \frac{\partial\hat{U}}{\partial x_2} = \frac{1}{6}EIL^3(8\kappa + 15L\lambda)\frac{\partial\kappa}{\partial x_2} + \frac{1}{10}EIL^4(25\kappa + 48L\lambda)\frac{\partial\lambda}{\partial x_2} \qquad (7.17)
\end{aligned}
$$

where

$$
\begin{aligned}
\frac{\partial\kappa}{\partial x_1} &= \frac{1}{\rho^2 d}\left\{2L(L^2+3\rho^2)\cos(L/\rho) - 6\rho^3\sin(L/\rho)\right\} \\
\frac{\partial\kappa}{\partial x_2} &= \frac{1}{\rho^2 d}\left\{3\rho(L^2+2\rho^2) - 6\rho^3\cos(L/\rho) - 2L(L^2+3\rho^2)\sin(L/\rho)\right\} \\
\frac{\partial\lambda}{\partial x_1} &= \frac{1}{\rho^2 d}\left\{2\rho^2 - (L^2+2\rho^2)\cos(L/\rho)\right\}
\end{aligned}
$$

$$\begin{aligned}\frac{\partial\lambda}{\partial x_2} &= \frac{1}{\rho^2 d}\left\{-2L\rho + (L^2+2\rho^2)\sin(L/\rho)\right\} \\ d &= -(L^4-24\rho^4)\cos(L/\rho) + 4\rho(-3\rho(L^2+2\rho^2) + L(L^2+6\rho^2)\sin(L/\rho)).\end{aligned}$$

In summary, the change in slope $\delta\theta = \delta\theta(\xi\,;\,x_1,x_2)$ is approximated in (7.11), where the constants κ and λ are evaluated in (7.14) and (7.13) for a prescribed tip position $\{x_1,x_2\}$. The corresponding reaction forces V and F acting on the fiber tip are evaluated in (7.16) and (7.17).

7.4.2 Slip Phase

During slip, it is convenient to assume negligible sliding resistance, i.e. $V = 0$. As before, $\delta\theta = \delta\theta(\xi)$ has the form given in (7.11). Substituting this expression into (7.2) and noting from (7.4) and (7.6) that $\theta_0(0) = \delta\theta(0) = 0$, it follows that $\kappa = 0$. Thus $\delta\theta$ becomes

$$\delta\theta = \lambda(\xi^3 - 3\xi L^2). \tag{7.18}$$

Substituting this expression into $(7.7)_1$ and solving for λ yields

$$\lambda = \frac{x_1 - \rho\sin\left(\frac{L}{\rho}\right)}{6\rho^4\sin\left(\frac{L}{\rho}\right) - 2L\rho\,(L^2+3\rho^2)\cos\left(\frac{L}{\rho}\right)}. \tag{7.19}$$

Since $\kappa = 0$, the elastic strain energy reduces to

$$U_{el} = \frac{12}{5}EIL^5\lambda^2 \tag{7.20}$$

and so

$$F = \frac{6EIL^5\left(x_1 - \rho\sin\left(\frac{L}{\rho}\right)\right)}{5\left(L\rho\,(L^2+3\rho^2)\cos\left(\frac{L}{\rho}\right) - 3\rho^4\sin\left(\frac{L}{\rho}\right)\right)^2}. \tag{7.21}$$

The corresponding horizontal position of the tip is

$$x_2 = X_2 + (X_1 - x_1)\frac{6\cos\left(\frac{L}{\rho}\right)\rho^3 - 3\left(L^2+2\rho^2\right)\rho + 2L\left(L^2+3\rho^2\right)\sin\left(\frac{L}{\rho}\right)}{6\rho^3\sin\left(\frac{L}{\rho}\right) - 2L\,(L^2+3\rho^2)\cos\left(\frac{L}{\rho}\right)}. \tag{7.22}$$

7.4.3 Analysis

Because of the non-conservative nature of stick-slip contact, it is necessary to keep a history of fiber configuration when studying the mechanical response over the course of loading. For the experiments of interest, loading is composed of two stages: compressive preload and retraction, which includes fiber detachment. During loading, the tip height x_1 is prescribed and parameterized by a non-dimensional time variable t. That is, $x_1 = \hat{x}_1(t)$. The true horizontal position of the fiber tip is given by the function $x_2 = \hat{x}_2(t)$, which is not known *a priori*.

Let $t = 0$ at the start of preload and prescribe t_p as the duration of the preload stage. Thus,

$$x_1 = \hat{x}_1(0) = X_1 \qquad \text{and} \qquad x_2 = \hat{x}_2(0) = X_2 \tag{7.23}$$

where X_1 and X_2 are evaluated in (7.8). Define

$$x_2^s = \hat{x}_2^s(t) = \lim_{\tau \to t^-} \hat{x}_2(\tau) \tag{7.24}$$

as the horizontal position of the fiber tip associated with sticking. At the start of preload $x_2^s = \hat{x}_2^s(0) = X_2$. If the magnitude of $V_{\text{el}} := V(x_1, x_2^s)$ evaluated in (7.17) is less than V_{cr}, then $\hat{x}_2(t) = x_2^s$; otherwise, $\hat{x}_2(t)$ is equal to the value $x_2 =: x_2^f$ obtained from (7.22). Mathematically, $\hat{x}_2$ may be expressed as

$$\hat{x}_2(t) = \begin{cases} x_2^s & \text{if } |V_{\text{el}}| < |V(x_1, x_2^s)| \\ x_2^f & \text{otherwise} \end{cases} \tag{7.25}$$

Here it is assumed that the fiber tip is rounded and its mechanics are governed by JKR theory. Hence, the interfacial shear strength may be approximated as

$$V_{\text{cr}} = \tau A_{\text{JKR}} \tag{7.26}$$

where, as before, τ is the shear strength per unit area of contact and the real area of contact A_{JKR} is calculated as

$$A_{\mathrm{JKR}}(F) = \pi\Big[\frac{3(1-\nu^2)R_t}{4E}\Big(-F+3\pi W_{ad}R_t + \sqrt{-6\pi W_{ad}FR_t+(3\pi W_{ad}R_t)^2}\Big)\Big]^{2/3}, \tag{7.27}$$

where $F = F(x_1, x_2^s)$ is evaluated in (7.16).

7.5 Slip Model

An alternative to the stick-slip model is the slip model, in which interfacial sliding resistance is neglected. In the case of vertical fibers, this corresponds to clamped-free buckling. As demonstrated in Figure 6.5, the clamped-free model best predicts stiffness during indentation with a spherical probe. This suggests that the slip model is a viable theory for describing the tip-substrate interactions with curved fibers.

The relationship between force F and tip height X_1 is established by solving the boundary value problem (7.2,7.3) for $V = 0$ and substituting the solution for θ into (7.7). This is performed in Matlab R2006a (The Mathworks, Inc.) using a finite difference package. The solution $F = F(X_1)$ will be slightly different than (7.21), since (7.21) was derived from (7.7), which assumes a small change in angle, i.e. $|\delta\theta| < \pi/12$. In general, the slip model, which is based on elastica theory, will be valid for a larger range of deformations than the stick-slip model, which employs a small-angle approximation.

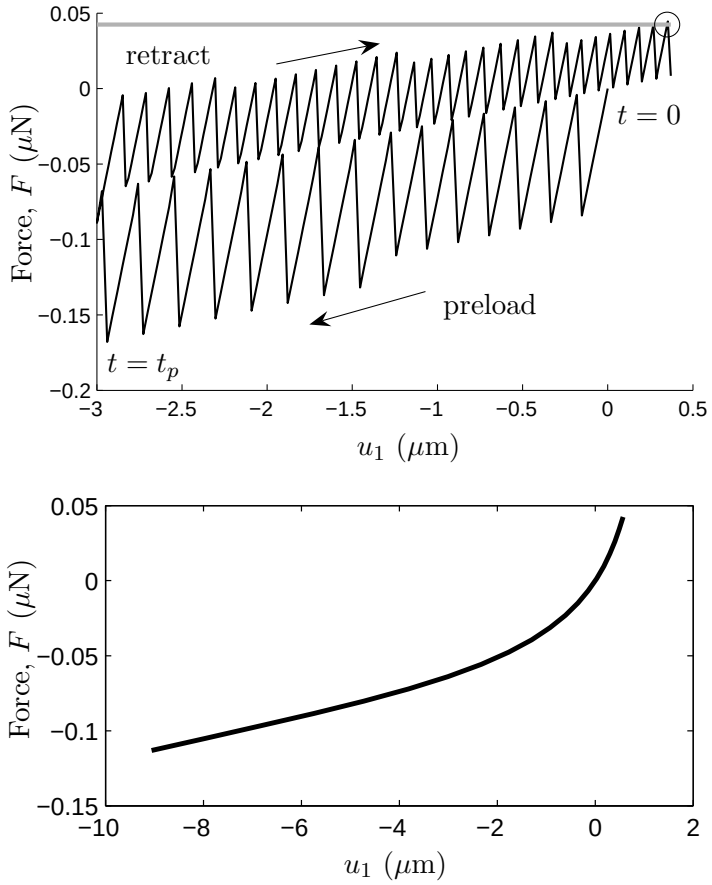

Figure 7.5. Force response during loading; gray line represents the detachment strength during slip, αp; $F > 0$ corresponds to tension; (top) stick-slip model, detachment occurs in circled region; (bottom) elastica model with slip only; $R = 0.4$ μm, $R_t = R$, $L = 20$ μm, $\rho = L$, E = 1 GPa, $\nu = 0.4$, $W_{ad} = 30$ mJ m^{-2}, $\tau = 10$ MPa and $\alpha = 0.75$.

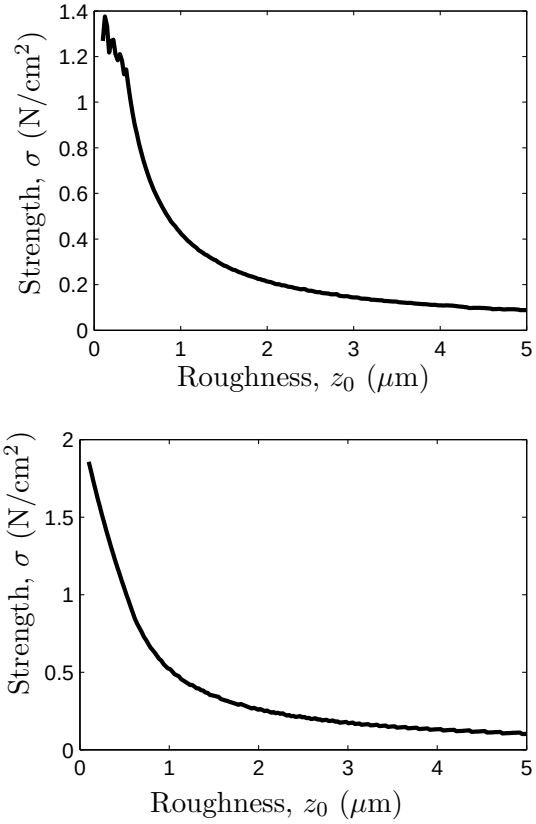

Figure 7.6. Detachment resistance of an array as a function of substrate roughness; (top) stick-slip model; (bottom) elastica model with slip only; $R = 0.4$ μm, $R_t = R$, $L = 20$ μm, $\rho = L$, E = 1 GPa, $\nu = 0.4$, $W_{ad} = 30$ mJ m^{-2}, $\tau = 10$ MPa and $\alpha = 0.75$, $D = 50{\times}10^6$ cm^2.

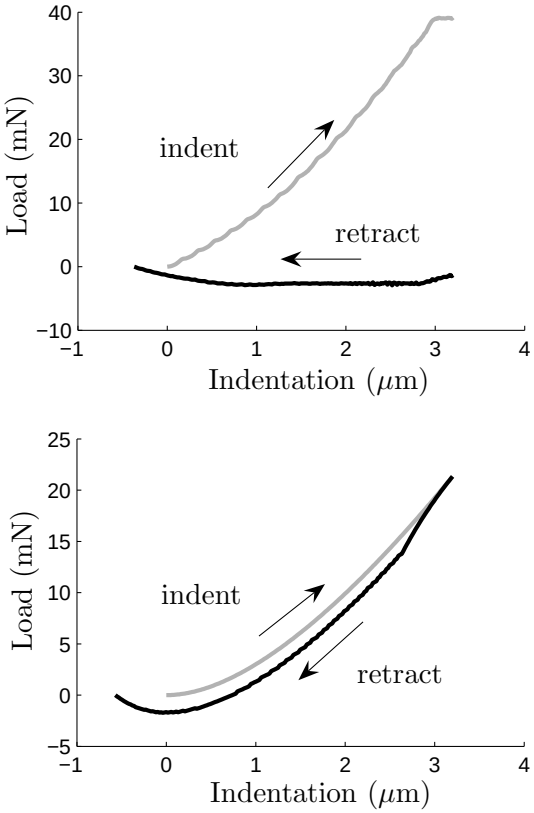

Figure 7.7. Force response to indentation of 5.17 cm sphere; positive load corresponds to compression; (top) stick-slip model, discontinuity caused by hysteresis in force-displacement relationship (see Figure 7.5(a)); (bottom) elastica model with slip only; $R = 0.4$ μm, $R_t = R$, $L = 20$ μm, $\rho = L$, E = 1 GPa, $\nu = 0.4$, $W_{ad} = 30$ mJ m^{-2}, $\tau = 10$ MPa and $\alpha = 0.75$, $D = 50{\times}10^6$ cm^2.

7.6 Results

Consider a fiber for which $R = 0.4$ μm, $R_t = R$, $L = 20$ μm, $\rho = L$, E = 1 GPa, $\nu = 0.4$, $W_{ad} = 30$ mJ m^{-2}, $\tau = 10$ MPa and $\alpha = 0.75$. The mechanical response during preload and substrate retraction are plotted in Figure 7.5. Note that for the stick-slip model, slip is immediately followed by a stick phase, resulting in a sawtooth force-displacement relationship. Interestingly, this result resembles the shear-displacement response for stick-slip motion. The gray line represents the normal bond strength $f_0 = \alpha p = 42$ nN in the presence of sliding. While the tip-substrate interface can withstand a tensile force greater than f_0, detachment is expected to spontaneously happen when slip occurs above this threshold. For the fiber considered here, detachment occurs at the upper right most peak in Fig. 7.5, where f = 44 nN and $u_1 = 0.35$ μm. Hence, the pull-off strength is slightly greater than f_0.

A tensile displacement of 0.35 μm suggests that an array of such fibers would be tolerant to roughness on the order of several hundred nanometers. Estimates for pull-off strength versus roughness are plotted in Figure 7.6. These results are based on the force-displacement relationship presented in Figure 7.5 and assume a fiber density of 50×10^6cm^{-2} and uniform roughness with a prescribed amplitude, z_0.

A standard technique for evaluating adhesion through tensile compliance is to study contact with a smooth hemisphere. As with a rough surface, adhesion with a hemisphere depends upon tensile displacement of the fiber tips during normal pull-off. Figure 7.7 presents a plot of estimated reaction force versus hemisphere indentation. Qualitatively, the elastica slip model more accurately resembles the experimental measurement plotted

in Figure 7.3. Quantitatively, the measured pull-off strength of 1.5 mN is close to the prediction of 1.7 mN made by the slip model.

It should be noted, that the compressive stiffness predicted by the slip model is several times greater than what is measured experimentally. This discrepancy may have to do with the mounting of the polypropylene sample. Unlike for the indentation test in Chapter 6, the sample of curved fibers was placed on GelPak 8 and it is possible that a bubble of air could have been present between the membrane and GelPak. Hence, the high compliance measured during indentation may be governed by membrane deformation rather than fiber bending. This condition should not effect the pull-off force.

It is also interesting to note that the bond strength predicted by the stick-slip model is almost a factor of two greater than the slip model. This result is counter-intuitive since the added stiffness introduced by the stick phase is expected to reduce tensile compliance. The large pull-off strength predicted by the stick-slip model is an artifact of the linearization used in deriving (7.7). If the same linearization were applied to the slip model, i.e. if (7.21) were used in place of the elastica solution discussed in Section 7.5, then the slip model would have predicted a pull-off strength of 4.5 mN, three times that predicted by the more accurate elastica model.

7.7 Design Maps

The preliminary results presented here demonstrate that adhesion is indeed possible with an array of curved fibers. A comparison of the experimental and theoretical results suggests that the tip-substrate interaction is best represented by the slip model. In this

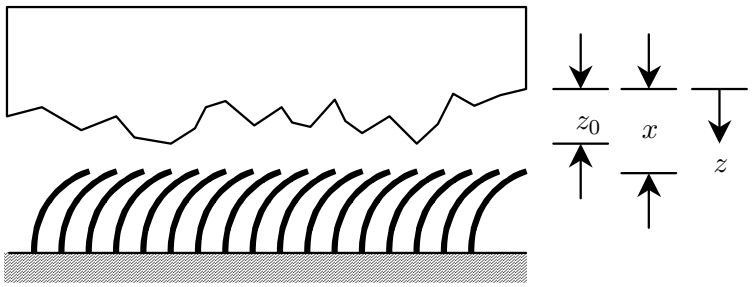

Figure 7.8. Fiber array in contact with a nominally flat surface with uniform roughness.

section, the slip model is computed for a range of other geometries in order to determine the optimal length, radius and elastic modulus for adhesion.

In general, adhesion will depend on the roughness of the contacting substrate. As shown in Figure 7.6, adhesion is greatest for contact with a smooth substrate but drops significantly when the roughness z_0 is on the order of several microns. For a roughness of $z_0 = 1$ μm, an array of 20 μm long, 0.8 μm radius fibers is expected to exhibit adhesion of 0.5 N/cm^2. This, however, assumes a density of 50×10^6cm^{-2}, which is several times greater than the critical density evaluated in (5.45) for $E = 1$ GPa and $W_{\text{ad}} = 30$ mJ/m^2. Such an array is likely to clump and thus exhibit a bond strength that is significantly less than 0.5 N/cm^2. A more accurate prediction is obtained using the method described in the following subsection.

7.7.1 Analysis

Solving the BVP (7.2,7.3) for $V = 0$ and substituting the solution for θ into (7.7) yields a function $u_1 = \eta(F)$. Such a mapping is homeomorphic on the domain and range of interest and thus invertible: $F = \eta^{-1}(u_1)$.

Define the local coordinate z as the distance from the substrate surface along $-\mathbf{e}_1$. The position $z = z_0$ corresponds to the tip of the tallest surface asperity and $z = x$ corresponds to the tips of the fibers (see Figure 7.8). The distribution of asperity heights is defined by the uniform probability density function

$$\Phi(z) = \{\, 1/z_0 \,\text{if}\, z \in [0, z_0]\,;\, 0 \,\text{otherwise}\}. \tag{7.28}$$

The probability that an asperity has a height between $z = a$ and $z = b$ is given by the integral

$$\mathcal{P}(a, b) = \int_a^b \Phi(z)\, dz. \tag{7.29}$$

The average force acting on a fiber may be expressed as

$$P_a(x) = \int_0^{z_0} \eta^{-1}(x - z)\Phi(z)\, dz. \tag{7.30}$$

Normal Strength

The pull-off strength of an array corresponds to an average tensile force

$$f = \max_x P_a(x). \tag{7.31}$$

Heuristically, this is found to equal

$$f = \int_0^{z_0} \eta^{-1}(x^* - z)\frac{1}{z_0}\, dz, \tag{7.32}$$

where

$$x^* = \max\{z_0, \eta(f_0)\}, \tag{7.33}$$

$f_0 = \alpha p$, and $p = 1.5\pi R_t W_{\rm ad}$. For an unclumped array, the normal strength of adhesion is

$$\sigma = \sigma(L, R; E, W_{\rm ad}, z_0) = D_{\rm cr} f, \tag{7.34}$$

where $D_{\rm cr}$ is the critical density evaluated in (5.45).

Shear Strength

For pure shear, $P_a = 0$, and so the position x corresponds to

$$x^* = x < (z_0 + \eta(f_0)) \,:\, P_a(x) = 0. \tag{7.35}$$

The average shear strength of a fiber is computed as

$$v = \int_0^{z_0} \tau A_{\rm JKR}(\eta^{-1}(x^* - z))\frac{1}{z_0}\, dz \tag{7.36}$$

where the function $A_{\rm JKR} = A_{\rm JKR}(F)$ is defined in (7.27). The shear strength of adhesion is

$$s = s(L, R; E, W_{\rm ad}, z_0) = D_{\rm cr} v. \tag{7.37}$$

7.7.2 Results

Contour plots of σ and s versus fiber length, L, and radius, R, are computed for various values of z_0. Here it is assumed that the material is intrinsically stiff, with an elastic modulus of $E = 1$ GPa. Also, $W_{\rm ad} = 30$ mJ/m^2, which is typical for polymeric materials in contact with a rigid substrate such as glass.

At the top of Figure 7.9 is a plot of normal bond strength σ in units of N/cm^2 for contact with a microrough surface of $z_0 = 1$ μm. Adhesion is largest with fibers that are greater

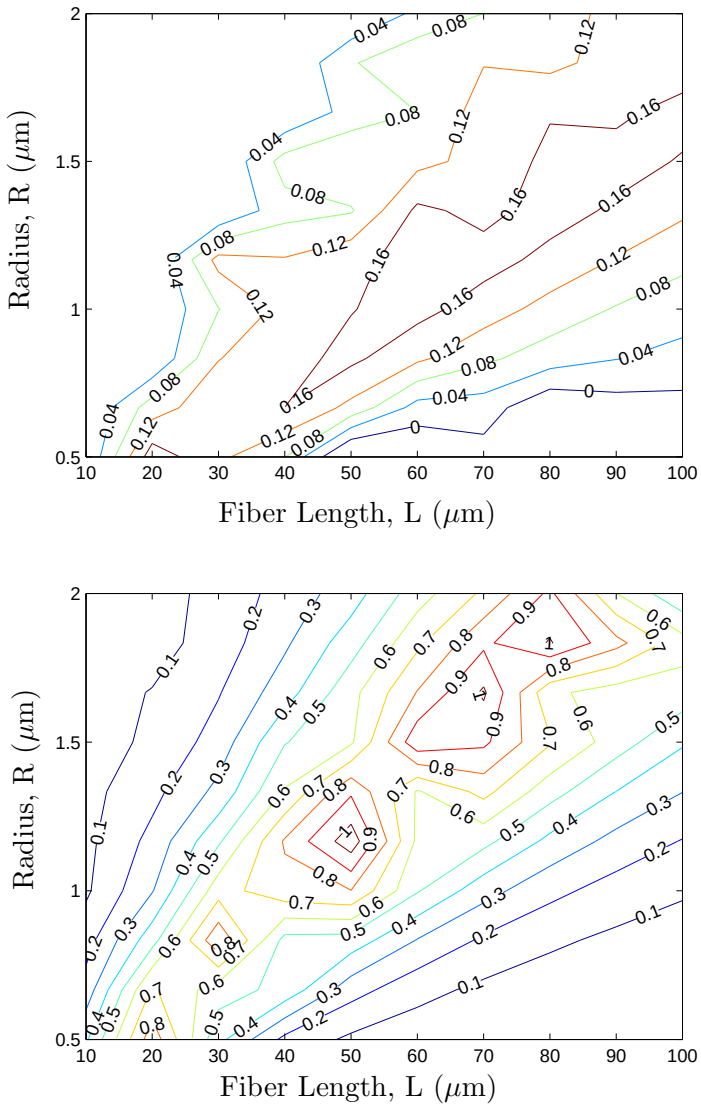

Figure 7.9. Bond strength in N/cm^2 for an array of curved fibers: $E = 1$ GPa, $W_{\text{ad}} = 30$ mJ/m^2, $\nu = 0.3$, $\rho = L$, $R_t = R$. Surface has roughness of $z_0 = 1$ μm. (top) normal pull-off, σ; (bottom) shear, s.

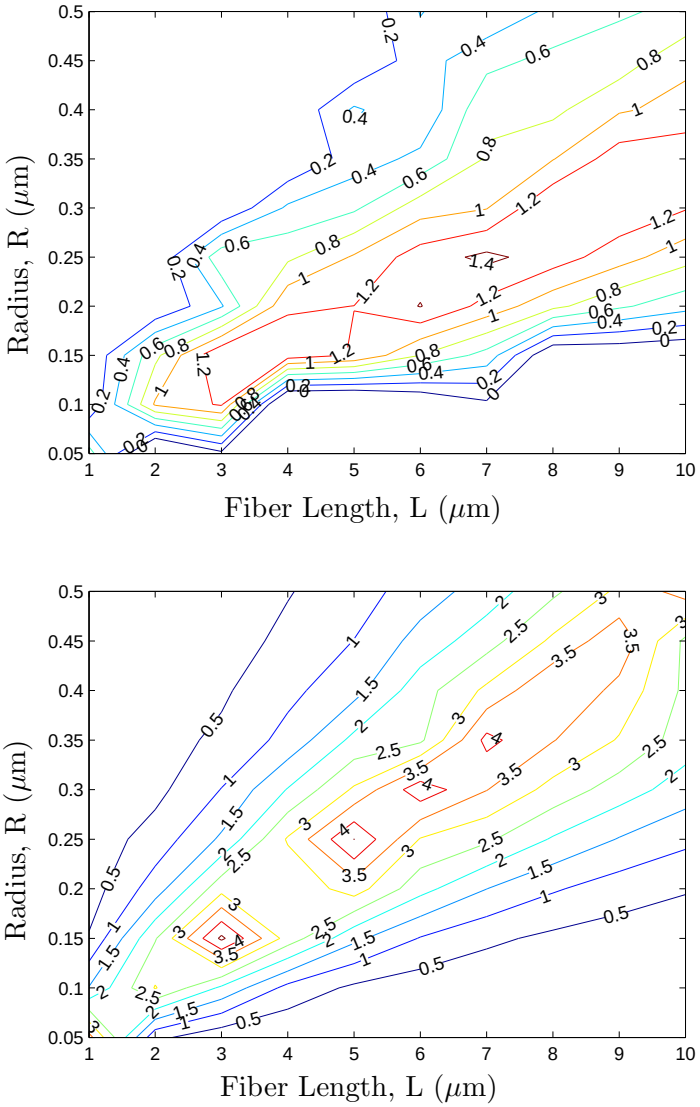

Figure 7.10. Bond strength in N/cm^2 for an array of curved fibers: $E = 1$ GPa, $W_{\text{ad}} = 30$ mJ/m^2, $\nu = 0.3$, $\rho = L$, $R_t = R$. Surface has roughness of $z_0 = 0.1$ μm. (top) normal pull-off, σ; (bottom) shear, s.

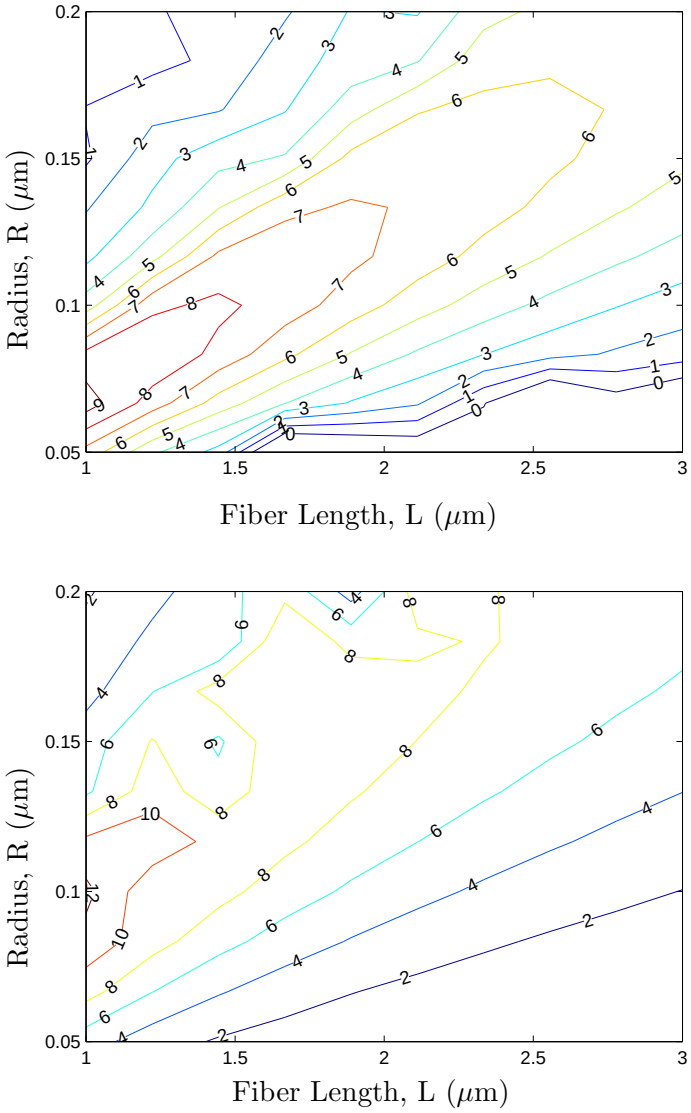

Figure 7.11. Bond strength in N/cm^2 for an array of curved fibers: $E = 1$ GPa, $W_{\text{ad}} = 30$ mJ/m^2, $\nu = 0.3$, $\rho = L$, $R_t = R$. Surface has roughness of $z_0 = 0.01$ μm. (top) normal pull-off, σ; (bottom) shear, s.

than 50 microns in length and that have a radius on the order of 1 micron. Interestingly, such fibers are similar in size to gecko setae. Nonetheless, σ is no greater than 0.2 N/cm^2, an order of magnitude smaller than that predicted for natural geckos.

Adhesion is significantly enhanced for loading in the shear direction. Figure 7.9(bottom) shows regions of the design space in which the shear strength reaches 1 N/cm^2 for contact with a microrough surface of $z_0 = 1$ μm. This region corresponds to geometries that roughly follow the rule $R \approx 0.02L + 0.2\mu$m.

Next, consider Figure 7.10(top), which plots σ (N/cm^2) for $z_0 = 0.1$ μm. Here, σ can exceed 1 N/cm^2 with a fiber of length $L < 10$ μm and radius $R \sim 0.2$ μm. As shown in 7.10(bottom), shear adhesion can be as large as 4 N/cm^2 for geometries such that $R \approx 0.05L$.

For contact with a nanorough surface of $z_0 = 0.01$ μm, σ and s approach 10 N/cm^2 for $L \sim 1$ μm and $R \sim 0.1$ μm (see Figure 7.11). Interestingly, these structures are similar in size to spatular branches. Although the predicted bond strength is on the order of natural gecko adhesion, the contacting surface is assumed to be smooth, with a roughness $z_0 \ll 1$ μm.

7.8 Concluding Remarks

The adhesion predicted in Figures 7.9, 7.10, and 7.11 contrast significantly over roughness and loading direction. Perhaps the most important outcome of this analysis is that for contact with typical microrough surfaces, curved fiber arrays exhibit 10 $\times$ greater adhesion in shear than in normal pull-off. Interestingly, this 10:1 ratio is also observed in natural setal arrays [9].

Adhesion in both shear and normal pull-off is enhanced by adopting a hierarchical

structure. Hierarchy could be achieved by terminating each microfiber into an array of nanofibers, just like in the natural gecko adhesive. Such a structure would adhere well to nominally flat surfaces, which have microroughness on a global length scale but are nanorough locally. Simply put, the microfibers would accommodate the global microroughness of the contacting surface while the nanofibers would adhere the nanorough sides of each surface asperity. For a hierarchical structure, bond strengths would approach the values predicted in Figure 7.11. These values are on the order of the 10 N/cm^2 shear strength measured in natural geckos.

Another solution is to replace the spherical tips of the microfibers with spatular-like plates. Interestingly, this design is adopted by anoles lizards, in which each setal stalk terminates into a flap of nanoscale thickness. A spatular plate design for permanent adhesion is proposed and analyzed in the following chapter.

Chapter 8

Proposed Design for Permanent Adhesion

Wall-climbing lizards adhere through the attachment of millions of nanosized flaps called *spatulae*. Typically, spatulae have a length and width of roughly 300 nm and a thickness in the range of 5-20 nm. During normal pull-off, each spatula produces 10 nN of tensile resistance [36]. This value is consistent with a Kendall peel model, which treats the flap as an elastic membrane with negligible bending stiffness [35], [46].

The pull-off strength can be significantly enhanced if the spatula is connected to the supporting shaft at its center rather than along its edge. While such a geometry is not ideal for gecko wall-climbing, which depends on easy and rapid detachment, it is well suited for permanent adhesion. A center supported spatulae is also expected to resist detachment under high shear loads, which induces shaft rotation. The two detachment modes are illustrated in Figure 8.1. Predictions for normal and shear strength are derived in the sections below using stationary principles and the specialization of finite elasticity to the membrane. Details of the analysis can also be found in [55].

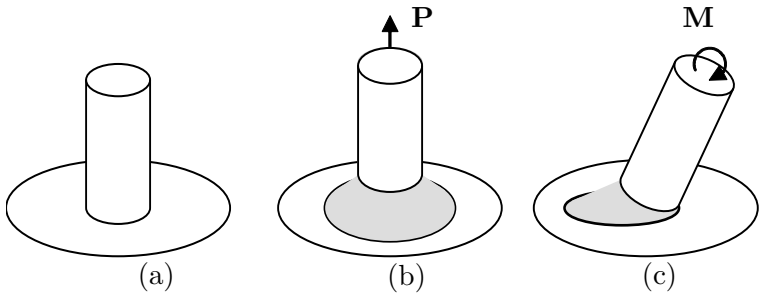

Figure 8.1. Illustration of shaft loaded membrane; (a) reference configuration, (b) delamination under normal translation, (c) delamination under rotation.

8.1 System Overview

This analysis concerns an isotropic elastic membrane sheet that is connected at its center to a rigid cylindrical shaft. For normal pull-off, the delamination zone is axisymmetric and can be parameterized by radius alone, allowing the computation of a strain energy release rate [79]. If delamination is generated by shaft rotation (usually induced by a shear load applied to the other end of the shaft) its shape must be identified by a real-valued function, significantly complicating the analysis. For this loading condition, it is convenient to consider only a restricted set of kinematically admissible deformation fields and statically admissible stress fields. Applying the stationary principles presented in [34] then yields upper and lower bounds for the strain energy functional. This method employs the principle of maximum complementary energy, a technique that has been applied to other problems in non-linear membrane theory, including the study of a clamped circular membrane that sags under its own weight [48] [51], the axial extension of a cylindrical membrane [34], and the puncturing of a thin elastic sheet [74]. For detailed derivation and

discussion of the principle of maximum complementary energy, the interested reader should refer to sections in [58], [77], and [23].

Here we adopt the classical strain-energy function of infinitesimal isotropic elasticity. To allow the theory to be valid for moderately large deformations, the infinitesimal strains are replaced by the Hencky (logarithmic) measure for finite strain [1] [2]. In the case of delamination by shaft rotation, it is demonstrated that for the geometry and loading range of interest, a similar result can be obtained with the Green strain.

An overview of the governing equations and principles for the shaft-loaded membrane are presented in Section 8.2. This includes a summary of the kinematics and constitutive law, as well as a discussion on the stationary principles of minimum potential and maximum complementary energy. Next, these principles are applied to the delamination of the shaft-loaded membrane. An approximate solution is derived for the case of delamination under shaft rotation. Numerical results are presented for both systems in Section 8.5. For delamination under rotation, the solution accuracy is demonstrated by the tightness in the bounds furnished by the two variational methods.

8.2 Governing Equations

Let $\mathcal{S}$ represent the surface of a rigid, infinite half-space and define the right-handed orthonormal triad $\{\mathbf{e}_1, \mathbf{e}_2, \mathbf{e}_3\}$ such that $\mathbf{e}_3$ is normal to the half-space. Next, let $\mathbf{X} = X_1\mathbf{e}_1 + X_2\mathbf{e}_2 + X_3\mathbf{e}_3$ denote the position of any point in $\mathbb{R}^3$ with respect to the origin $O \in \mathcal{S}$. In addition, let $\{s, \theta, X_3\}$ represent a cylindrical coordinate system with origin O and polar axis $\mathbf{e}_1$ and define the right-handed orthonormal triad $\{\mathbf{e}_s, \mathbf{e}_\theta, \mathbf{e}_3\}$ such that

$$\mathbf{e}_s = \cos\theta\mathbf{e}_1 + \sin\theta\mathbf{e}_2 \qquad \text{and} \qquad \mathbf{e}_\theta = \mathbf{e}_3 \times \mathbf{e}_s. \tag{8.1}$$

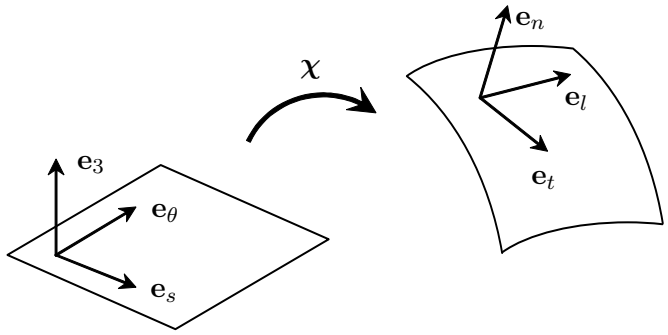

Figure 8.2. Local coordinate system in reference and deformed configurations

The two coordinate systems are related by the equations

$$X_1 = s\cos\theta \qquad \text{and} \qquad X_2 = s\sin\theta. \tag{8.2}$$

Consider an homogeneous, elastic membrane that on one side adheres to the half-space and on the other side is attached to the base $\mathcal{B}_0$ of a rigid cylindrical shaft. Delamination is possible by translating and/or rotating the shaft base to a new configuration $\mathcal{B}$. Let Ω denote the midplane of the delaminated portion of the membrane that is not in contact with the shaft and identify its boundary $\partial\Omega$ with the function $v(\theta) \geq R \ \forall\theta \in [0,\, 2\pi]$ through the representation

$$\partial\Omega = \{\mathbf{X} \in \mathbb{R}^3 \,:\, s \in \{R, v(\theta)\},\, \theta \in [0,\, 2\pi]\}. \tag{8.3}$$

The function $v(\theta)$, which defines the amount of delaminated material, may also be used to define the surface Ω in its natural configuration:

$$\Omega_0 = \{\mathbf{X} \in \mathbb{R}^3 \,:\, s \in [R, v(\theta)],\, \theta \in [0,\, 2\pi],\, X_3 = 0\}. \tag{8.4}$$

8.2.1 Kinematics

Let the function $\boldsymbol{\chi} : \Omega_0 \to \Omega$ map a point $\mathbf{X} \in \Omega_0$ to its position $\mathbf{x}$ in the deformed configuration Ω, i.e.

$$\mathbf{x} = \boldsymbol{\chi}(\mathbf{X}) \qquad \text{for} \qquad \mathbf{X} \in \Omega_0. \tag{8.5}$$

Membrane theory assumes that there is no shearing along the tangent plane, and so the deformation may be expressed as

$$\boldsymbol{\chi}(\mathbf{X}) = \mathbf{X} - X_3\mathbf{e}_3 + \mathbf{u}_0 + (X_3 + q)\mathbf{e}_n \tag{8.6}$$

where $\mathbf{u}_0 = \mathbf{u}_0(s, \theta, X_3)$ is the displacement of a point on the midplane Ω_0, $\mathbf{e}_n$ is the unit normal to the deformed surface Ω and $q = q(s, \theta, X_3)$ is the displacement of points away from the midplane relative to the deformed orientation. By definition of midplane, the function q vanishes identically on the midplane, and thus must satisfy the following conditions:

$$q(X_3 = 0) = \left(\frac{\partial q}{\partial s}\right)_{X_3=0} = \frac{1}{s}\left(\frac{\partial q}{\partial \theta}\right)_{X_3=0} = 0. \tag{8.7}$$

Consider the vectors

$$\mathbf{e}_s{}' = \mathbf{e}_s + \frac{\partial}{\partial s}\mathbf{u}_0 \qquad \text{and} \qquad \mathbf{e}_\theta{}' = \mathbf{e}_\theta + \frac{1}{s}\frac{\partial}{\partial \theta}\mathbf{u}_0, \tag{8.8}$$

which span the plane tangent to Ω. These vectors are, in general, not perpendicular or of unit length but, nonetheless, can be used to evaluate the unit normal in the following way:

$$\mathbf{e}_n = \frac{\mathbf{e}_s{}' \times \mathbf{e}_\theta{}'}{\|\mathbf{e}_s{}' \times \mathbf{e}_\theta{}'\|}, \tag{8.9}$$

where $\| \bullet \|$ is the Euclidean norm.

Define $\mathbf{F} = \bigtriangledown\boldsymbol{\chi}(\mathbf{X})$ to be the gradient of the deformation $\mathbf{X} \mapsto \boldsymbol{\chi}(\mathbf{X})$. This is computed as $\mathbf{F} = \boldsymbol{\chi} \otimes \bigtriangledown$ [11], where

$$\bigtriangledown = \mathbf{e}_s\frac{\partial}{\partial s} + \mathbf{e}_\theta\frac{1}{s}\frac{\partial}{\partial \theta} + \mathbf{e}_3\frac{\partial}{\partial X_3}. \tag{8.10}$$

It is convenient to decompose the deformation gradient with respect to the midplane and its complement:

$$\mathbf{F}(\mathbf{X}) = \mathbf{F}_0 + \hat{\mathbf{F}} \tag{8.11}$$

where

$$\mathbf{F}_0 := \mathbf{F}(\mathbf{X} \,:\, X_3 = 0) = \mathbf{I} - \mathbf{e}_3 \otimes \mathbf{e}_3 + \bigtriangledown \mathbf{u}_0 + \left\{ 1 + \frac{\partial q}{\partial X_3} \right\} \mathbf{e}_n \otimes \mathbf{e}_3 \tag{8.12}$$

and

$$\hat{\mathbf{F}} := \mathbf{F} - \mathbf{F}_0 = (X_3 + q) \left\{ \frac{\partial \mathbf{e}_n}{\partial s} \otimes \mathbf{e}_s + \frac{1}{s} \frac{\partial \mathbf{e}_n}{\partial \theta} \otimes \mathbf{e}_\theta \right\} + \frac{\partial q}{\partial s} \mathbf{e}_n \otimes \mathbf{e}_s + \frac{1}{s} \frac{\partial q}{\partial \theta} \mathbf{e}_n \otimes \mathbf{e}_\theta. \tag{8.13}$$

By the polar decomposition theorem, there exists tensors $\mathbf{R} \in \mathrm{Orth}^+$ and $\mathbf{V} \in \mathrm{Sym}$ such that $\mathbf{F} = \mathbf{VR}$. The tensor $\mathbf{V}$ is known as the left stretch tensor and its natural log is defined as the spatial Hencky strain tensor $\mathbf{E}_H = \ln \mathbf{V}$. The strain tensor may also be expressed as

$$\mathbf{E}_H = \frac{1}{2} \ln \mathbf{B} \tag{8.14}$$

where $\mathbf{B} = \mathbf{F}\mathbf{F}^\top$ is the left Cauchy-Green tensor [11].

8.2.2 Stress Tensors and Constitutive Law

For moderately large deformations, the constitutive response of a material can be accurately characterized by a strain-energy function $W(\mathbf{F})$ of the form

$$W = \mu({\gamma_I}^2 + {\gamma_{II}}^2 + {\gamma_{III}}^2) + \frac{1}{2}\lambda(\gamma_I + \gamma_{II} + \gamma_{III})^2 \tag{8.15}$$

where $\{\gamma_i \,:\, i = I, II, III\}$ are the eigenvalues of $\mathbf{E}_H$ and μ and λ are the Lamé moduli evaluated at small strains [1], [2]. Hencky's constitutive equation is given by

$$s_i = \frac{\partial W}{\partial \gamma_i} = 2\mu\gamma_i + \lambda(\gamma_I + \gamma_{II} + \gamma_{III}) \tag{8.16}$$

where $\{s_i\}$ are the principal components (eigenvalues) of the Kirchhoff stress tensor $\mathbf{S}$. For plane stress problems, (8.15) reduces to

$$W = \frac{2\mu}{\lambda + 2\mu}\left[\lambda\gamma_t\gamma_l + (\lambda+\mu)({\gamma_t}^2 + {\gamma_l}^2)\right] \tag{8.17}$$

where γ_t and γ_l are the principal strains on the tangent plane and

$$\gamma_n = -\frac{\lambda}{\lambda + 2\mu}(\gamma_t + \gamma_l) \tag{8.18}$$

is the principal strain normal to Ω.

In tensorial form,

$$\mathbf{S} = 2\mu\mathbf{E}_H + \lambda(\mathrm{tr}\mathbf{E}_H)\mathbf{1} \tag{8.19}$$

where $\mathbf{1}$ is the unit tensor [1]. Inverting (8.19) yields

$$\mathbf{E}_H = \frac{1}{2\mu}\left[\mathbf{S} - \frac{\lambda}{2\mu + 3\lambda}(\mathrm{tr}\mathbf{S})\mathbf{1}\right], \tag{8.20}$$

which implies

$$\gamma_i = \frac{1}{2\mu}s_i - \frac{\lambda}{(2\mu)(2\mu+3\lambda)}(s_I + s_{II} + s_{III}). \tag{8.21}$$

The inversion is performed by taking the trace of both sides, substituting the solution for $\mathrm{tr}\mathbf{E}$ back into (8.19) and then solving for $\mathbf{E}$. Similarly, the strain energy function can be expressed as

$$\begin{aligned} W &= W(\mathbf{F}) = \frac{1}{2}\mathbf{S}\cdot\mathbf{E}_H && (8.22)\\ &= \hat{W}(\mathbf{E}_H) = \mu\,\mathrm{tr}\left(\mathbf{E}_H^2\right) + \frac{1}{2}\lambda\left(\mathrm{tr}\mathbf{E}_H\right)^2 && (8.23)\\ &= \tilde{W}(\mathbf{S}) = \frac{1}{4\mu}\mathrm{tr}\left(\mathbf{S}^2\right) - \frac{\lambda}{(4\mu)(2\mu+3\lambda)}\left(\mathrm{tr}\mathbf{S}\right)^2. && (8.24) \end{aligned}$$

Another stress tensor that will be relevant to analysis is the Piola tensor $\mathbf{P} = \mathbf{F}^{-1}\mathbf{S}$. Let $\{\eta_i : i = I, II, III\}$ denote the eigenvalues of $\mathbf{P}\mathbf{P}^\top$. Then, the principal components

of $\mathbf{P}$ are $t_i = \sqrt{\eta_i}$, which are known as the Biot stresses. For plane stress,

$$\gamma_t = \frac{1}{2\mu} t_t - \frac{\lambda}{(2\mu)(2\mu + 3\lambda)}(t_t + t_l) \tag{8.25}$$

$$\gamma_l = \frac{1}{2\mu} t_l - \frac{\lambda}{(2\mu)(2\mu + 3\lambda)}(t_t + t_l). \tag{8.26}$$

8.2.3 Membrane Approximation

For the applications presented in Sections 8.3 and 8.4, we consider a membrane of thickness H. For simplicity, it is assumed that H is vanishingly small. Thus, the deformation tensor is approximated by $\mathbf{F}_m$, which is defined as

$$\mathbf{F}_m := \lim_{H \to 0} \mathbf{F} \tag{8.27}$$

for all points in the membrane. Noting that $|X_3| \leq 2H$ and $H \to 0$, it follows from (8.7) that

$$\mathbf{F}_m = \mathbf{F}_0 \equiv \mathbf{I} - \mathbf{e}_3 \otimes \mathbf{e}_3 + \bigtriangledown \mathbf{u}_0 + \left\{ 1 + \frac{\partial q}{\partial X_3} \right\} \mathbf{e}_n \otimes \mathbf{e}_3. \tag{8.28}$$

Based on this assumption of an infinitesimally thin membrane, the Hencky strain tensor becomes

$$\mathbf{E}_m = \frac{1}{2} \ln \left(\mathbf{F}_m \mathbf{F}_m^\top \right). \tag{8.29}$$

Henceforth, $\mathbf{F}_m$ and $\mathbf{E}_m$ will be used in place of the deformation gradient and Hencky strain tensors, respectively.

8.2.4 Variational Principles

For a prescribed shaft configuration $\mathcal{B}$ and delamination zone Ω_0, the total potential energy of the system is [34]

$$U(\chi) = \int_{\Omega_0} W \, H \, dA - \int_{\partial \Omega_0^\sigma} \boldsymbol{\sigma} \cdot \boldsymbol{\chi} \, H \, dS. \tag{8.30}$$

where $\partial\Omega_0^\sigma$ denotes the part of the boundary where traction is prescribed, $\mathbf{N}$ is the unit outward normal to $\partial\Omega_0^\sigma$ lying in the tangent plane to Ω_0, and $\boldsymbol{\sigma} = \mathbf{P}^T\mathbf{N}$ on $\partial\Omega_0^\sigma$. It should be noted that the work of adhesion (or surface energy) is not included in the potential energy, but will be introduced later. The dual to the potential is the complementary energy:

$$\Phi(\mathbf{P}) = \int_{\partial\Omega_0^x} (\mathbf{P}^T\mathbf{N}) \cdot \boldsymbol{\xi}\, H\, dS - \int_{\Omega_0} W_c\, H\, dA, \tag{8.31}$$

where $\partial\Omega_0^x$ is the part of $\partial\Omega_0$ where position is prescribed, $\mathbf{N}$ is the unit outward normal to $\partial\Omega_0^x$ lying in the tangent plane to Ω_0, $\boldsymbol{\xi}$ is the prescribed position of points on $\partial\Omega_0^x$, and

$$W_c = \mathbf{P} \cdot \mathbf{F} - W \tag{8.32}$$

is the complementary energy density [74]. Assuming plane stress, W_c reduces to [34]

$$W_c = e^{\gamma_t} t_t + e^{\gamma_l} t_l - W. \tag{8.33}$$

where e^{γ_t} and e^{γ_l} are the principal stretches associated with eigenvalues of the Hencky strain tensors.

Let $\mathcal{F}$ denote the space of all geometrically admissible deformation fields and define

$$\mathcal{P} := \{\mathbf{P} \,:\, \mathrm{Div}\,\mathbf{P} = \mathbf{0},\, \mathbf{P}^T\mathbf{N} = \boldsymbol{\sigma} \,\mathrm{on}\, \partial\Omega_0^\sigma\} \tag{8.34}$$

where Div is the divergence operation with respect to $\mathbf{X}$. At equilibrium, the potential energy is computed as

$$U^* = \min_{\chi\in\mathcal{F}} U(\chi) = \max_{\mathbf{P}\in\mathcal{P}} \Phi(\mathbf{P}). \tag{8.35}$$

To obtain an analytic solution, it may be convenient to study only a restricted class of deformation and stress fields, denoted by $\mathcal{F}_0 \subset \mathcal{F}$ and $\mathcal{P}_0 \subset \mathcal{P}$, respectively. Extremizing over these restricted spaces will yield upper and lower bounds on U^*:

$$\min_{\chi\in\mathcal{F}_0} U(\chi) \geq U^* \geq \max_{\mathbf{P}\in\mathcal{P}_0} \Phi(\mathbf{P}). \tag{8.36}$$

Next, let W_s denote the work required to create new surface via delamination and define the total energy of the system as $E = U + W_s$. The work W_s may be expressed as

$$W_s = \int_{\Omega_0} W_{ad}\, dA, \tag{8.37}$$

where W_{ad} is the work of adhesion per unit area. By the Griffith energy balance, E is stationary with respect to variations of the form

$$v \mapsto \tilde{v} = v + \delta v, \tag{8.38}$$

where $\delta v = \delta v(\theta)$ is an arbitrarily small but kinematically admissible perturbation of the field $v(\theta)$.

8.3 Application to Normal Pull-off

Suppose that the shaft is pulled from the substrate through a distance Δ such that

$$\mathbf{x} = R\mathbf{e}_s + \Delta\mathbf{e}_3 \tag{8.39}$$

for points on $\partial\mathcal{B}$. The deformation response is assumed to be axisymmetric, and so

$$\mathbf{u}_0 = u_s(s)\mathbf{e}_s + u_3(s)\mathbf{e}_3. \tag{8.40}$$

Following from (8.8) and (8.9),

$$\mathbf{e}_n = \frac{1}{\sqrt{(1+u_{s,s})^2 + u_{3,s}^2}}\{-u_{3,s}\mathbf{e}_s + (1+u_{s,s})\mathbf{e}_3\}, \tag{8.41}$$

where $u_{x,y} = \partial u_x/\partial y$. Substituting these into the deformation gradient tensor (8.28) and then performing an eigen decomposition on the Hencky strain tensor (8.29) for points on the midplane yields

$$\mathbf{E}_m = \gamma_t \mathbf{e}_t \otimes \mathbf{e}_t + \gamma_l \mathbf{e}_l \otimes \mathbf{e}_l + \gamma_n \mathbf{e}_n \otimes \mathbf{e}_n \tag{8.42}$$

where $\mathbf{e}_l = \mathbf{e}_\theta$, $\mathbf{e}_t = \mathbf{e}_l \times \mathbf{e}_n$, and

$$\gamma_t = \frac{1}{2}\ln\left[u_{3,s}^2 + (1+u_{s,s})^2\right], \qquad \gamma_l = \ln\left[1+\frac{u_s}{s}\right], \qquad \gamma_n = \ln\left[1+\frac{\partial q}{\partial X_3}\right]. \tag{8.43}$$

8.3.1 General Solution at Equilibrium

The displacements $u_s = u_s(s)$ and $u_3 = u_3(s)$ are determined by extremizing the potential energy functional. Since there is no part of the boundary where the traction is prescribed, $\partial\Omega_0^\sigma = \oslash$. Hence, substituting (8.17) into (8.30),

$$U = \int_R^v 2\pi s H\left[\frac{2\mu}{\lambda+2\mu}\left\{\lambda\gamma_t\gamma_l + (\lambda+\mu)({\gamma_t}^2 + {\gamma_l}^2)\right\}\right] ds. \tag{8.44}$$

Next, substituting in the eigenvalues (8.43) yields a functional of the form

$$U(u_s, u_3; v) = \int_R^v f(s, u_s(s), u_{s,s}(s), u_3(s), u_{3,s}(s))\, ds. \tag{8.45}$$

As a result of assuming an infinitesimally thin membrane, the function q only arises in γ_n and thus does not enter into the strain energy for plane stress problems.

The Euler-Lagrange differential equations for the functional (8.45) are

$$\frac{\partial f}{\partial u_s} - \frac{\partial}{\partial s}\left(\frac{\partial f}{\partial u_{s,s}}\right) = 0 \qquad \text{and} \qquad \frac{\partial f}{\partial u_3} - \frac{\partial}{\partial s}\left(\frac{\partial f}{\partial u_{3,s}}\right) = 0. \tag{8.46}$$

After some manipulation, the combined differential equations furnish two second-order ordinary differential equations

$$u_{s,ss} - g_s(s, u_s, u_{s,s}, u_3, u_{3,s}) = 0 \qquad \text{and} \qquad u_{3,ss} - g_3(s, u_s, u_{s,s}, u_3, u_{3,s}) = 0, \tag{8.47}$$

where

$$\begin{aligned} g_s \;=\; & \{2\left[\lambda^2\gamma_l^2 + 2\gamma_t(\lambda+\mu)(-\lambda+2\gamma_t(\lambda+\mu)) + \gamma_l\lambda(-\lambda+4\gamma_t(\lambda+\mu))\right]u_s(1+u_{s,s}) \\ & + s\left[\left(4\gamma_l^2\lambda(\lambda+\mu) + 2\gamma_t(-2+2\gamma_t)\lambda(\lambda+\mu) + \gamma_l(-8(\lambda+\mu)^2 + 2\gamma_t(5\lambda^2+8\lambda\mu+4\mu^2))\right)u_{3,s}^2\right. \\ & \left. -(\gamma_l\lambda + 2\gamma_t(\lambda+\mu))(1+u_{s,s})\big((2\gamma_l - 2\gamma_t)(\lambda+2\mu) + ((-2_2\gamma_t)\lambda + 4\gamma_l(\lambda+\mu))u_{s,s}\big)\right]\}/ \\ & \{2s\big(\gamma_l^2\lambda^2 + 2\gamma_l(-1+2\gamma_t)\lambda(\lambda+\mu) + 2\gamma_t(-2+2\gamma_t)(\lambda+\mu)^2\big)(s+u_s)\} \end{aligned}$$

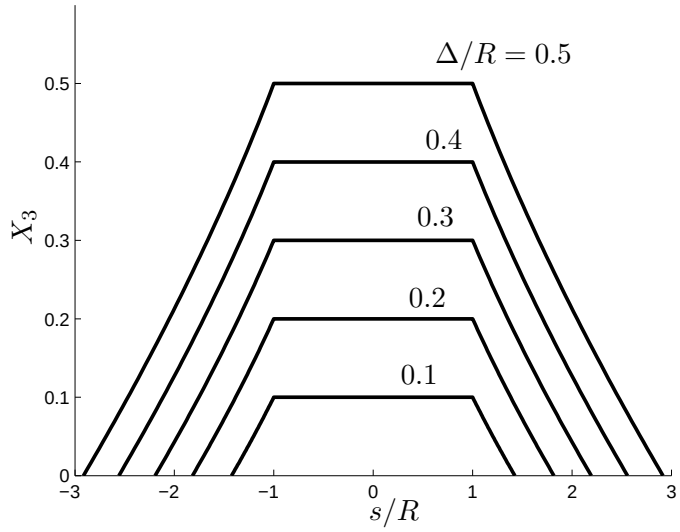

Figure 8.3. Profile of membrane for non-dimensional work of adhesion $W_{ad}/ER = 10^{-5}$, non-dimensional thickness $H/R = 0.01$ and various shaft heights.

and

$$
\begin{aligned}
g_3 \quad = \quad & \{u_{3,s}\big[\big(\lambda^2\gamma_l^2 + 2\gamma_t(\lambda+\mu)(-\lambda+2\gamma_t(\lambda+\mu)) + \gamma_l\lambda(-\lambda+4\gamma_t(\lambda+\mu))\big)u_s \\
& +s\big(-\gamma_l^2\lambda(3\lambda+4\mu) + 2\gamma_t(\lambda+\mu)(\lambda+2\gamma_t\mu) + \gamma_l(4(\lambda+\mu)^2 - 2\gamma_t(3\lambda^2+6\lambda\mu+4\mu^2)) \\
& -(4\gamma_l^2\lambda(\lambda+\mu) + 2\gamma_t(-2+2\gamma_t)\lambda(\lambda+\mu) + \gamma_l(-1+2\gamma_t)(5\lambda^2+8\lambda\mu+4\mu^2))u_{s,s}\big)\big]\}/ \\
& \{s\big(\gamma_l^2\lambda^2 + 2\gamma_l(-1+2\gamma_t)\lambda(\lambda+\mu) + 2\gamma_t(-2+2\gamma_t)(\lambda+\mu)^2\big)(s+u_s)\}.
\end{aligned}
$$

8.3.2 Boundary Conditions

The membrane is subject to the boundary conditions

$$u_s(R) = u_s(v) = u_3(v) = 0 \qquad \text{and} \qquad u_3(R) = \Delta. \tag{8.48}$$

These four boundary conditions are used to solve for the four constants of integration derived from (8.47). The remaining unknown is the radius v of the delaminated zone. From the Griffith energy balance, it follows that $dU/dv = -dW_s/dv$, where W_s is the work required

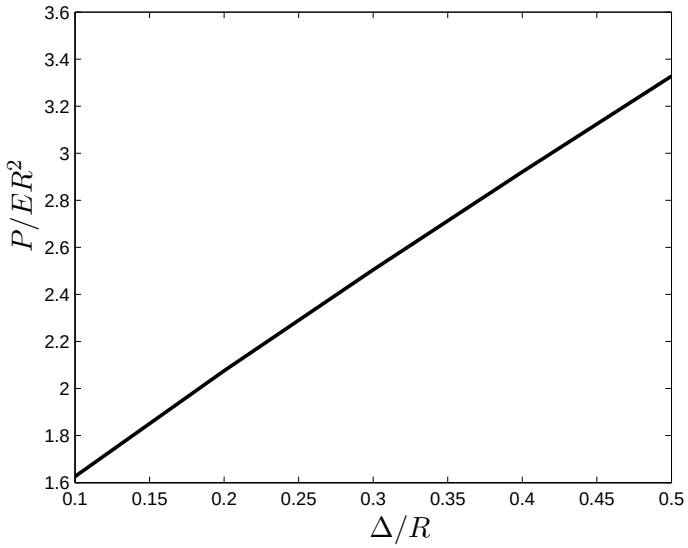

Figure 8.4. Non-dimensional normal load versus normalized shaft height for non-dimensional work of adhesion $W_{ad}/ER = 10^{-5}$ and non-dimensional thickness $H/R = 0.01$.

to create new surface. Following from (8.37), W_s is given by

$$W_s = (\pi v^2 - \pi R^2) W_{ad}. \tag{8.49}$$

The energy release rate dU/dv is determined with the aid of Leibniz' rule:

$$\frac{dU}{dv} = f(v) + \int_R^v \left\{ \frac{\partial f}{\partial u_s}\frac{\partial u_s}{\partial v} + \frac{\partial f}{\partial u_{s,s}}\frac{\partial u_{s,s}}{\partial v} + \frac{\partial f}{\partial u_3}\frac{\partial u_3}{\partial v} + \frac{\partial f}{\partial u_{3,s}}\frac{\partial u_{3,s}}{\partial v} \right\} ds. \tag{8.50}$$

For stationary functions u_s and u_3 satisfying (8.46), the integrand is the derivative of

$$\frac{\partial f}{\partial u_{s,s}}\frac{\partial u_s}{\partial v} + \frac{\partial f}{\partial u_{3,s}}\frac{\partial u_3}{\partial v} \tag{8.51}$$

and so

$$\frac{dU}{dv} = f(v) + \left[\frac{\partial f}{\partial u_{s,s}}\frac{\partial u_s}{\partial v} + \frac{\partial f}{\partial u_{3,s}}\frac{\partial u_3}{\partial v} \right]_R^v. \tag{8.52}$$

Noting that $(\partial u_s/\partial v)_R = (\partial u_3/\partial v)_R = 0$, $(\partial u_s/\partial v)_v = -u_{s,s}(v)$ and $(\partial u_3/\partial v)_v = -u_{3,s}(v)$, the energy release rate reduces to

$$\frac{dU}{dv} = f(v) - \left(\frac{\partial f}{\partial u_{s,s}}\right)_{s=v} u_{s,s}(v) - \left(\frac{\partial f}{\partial u_{3,s}}\right)_{s=v} u_{3,s}(v). \tag{8.53}$$

Thus, the Griffith energy balance yields an additional boundary condition

$$f(v) - \left(\frac{\partial f}{\partial u_{s,s}}\right)_{s=v} u_{s,s}(v) - \left(\frac{\partial f}{\partial u_{3,s}}\right)_{s=v} u_{3,s}(v) = -2\pi v W_{ad}, \tag{8.54}$$

which may be used to solve for v. This boundary condition is related to the 2^{nd} Weierstrass-Erdmann corner condition as well as the material (configurational) force balance at the edge of a delamination zone.

8.4 Shaft Rotation

Now consider a rotation $\psi\mathbf{e}_2$ about the pivot point $\mathbf{p} = R\mathbf{e}_1$, as shown in Figure 8.5. Hence, for $\theta \in [0,\, 2\pi]$,

$$\mathbf{x} = R\mathbf{e}_s + R(1-\cos\theta)(1-\cos\psi)\mathbf{e}_1 + R(1-\cos\theta)\sin\psi\mathbf{e}_3 \tag{8.55}$$

on $\partial\mathcal{B}$.

For this system, Ω is not axisymmetric and the task of determining the deformation at equilibrium is far more difficult than for the previous, axisymmetric system. Instead, approximate upper and lower bounds are obtained by employing the principles of minimum potential and maximum complementary energy, respectively.

8.4.1 Upper Bound

To obtain an approximate expression for the potential energy it is assumed that

$$\mathbf{u}_0(s,\theta) = u_1(s,\theta)\mathbf{e}_1 + u_3(s,\theta)\mathbf{e}_3 \tag{8.56}$$

with

$$\begin{aligned} u_1(s,\theta) &= R(1-\cos\theta)(1-\cos\psi)\frac{v-s}{v-R} \\ u_3(s,\theta) &= R(1-\cos\theta)\sin\psi\frac{v-s}{v-R}. \end{aligned}$$

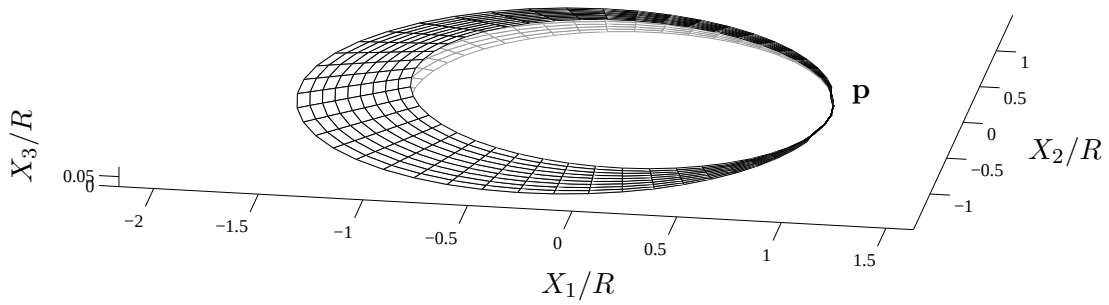

Figure 8.5. Delamination of membrane under shaft rotation of $\psi = 0.05$ radians; non-dimensional work of adhesion $W_{ad}/ER = 10^{-5}$ and non-dimensional thickness $H/R = 0.01$.

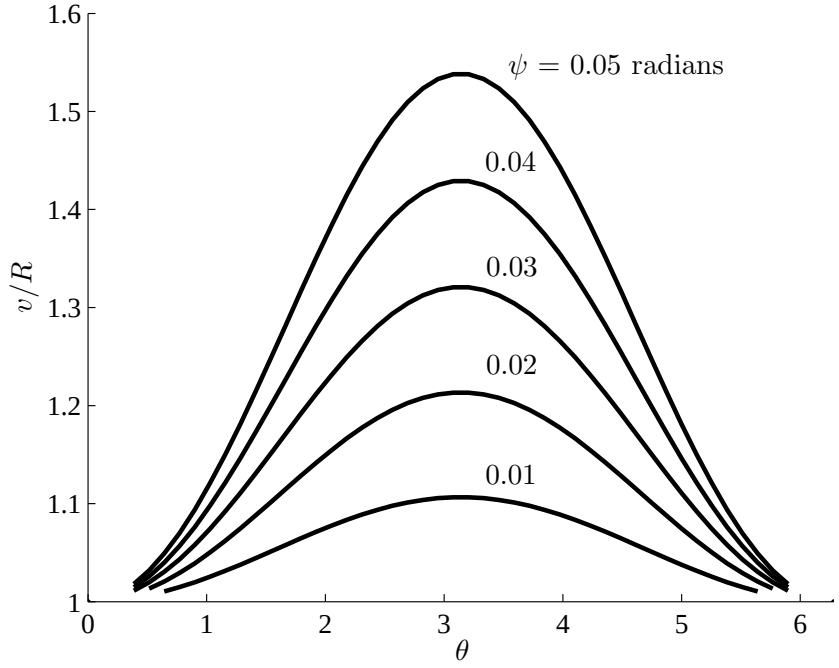

Figure 8.6. Plot of delamination zone for non-dimensional work of adhesion $W_{ad}/ER = 10^{-5}$, non-dimensional thickness $H/R = 0.01$, and various angles of rotation.

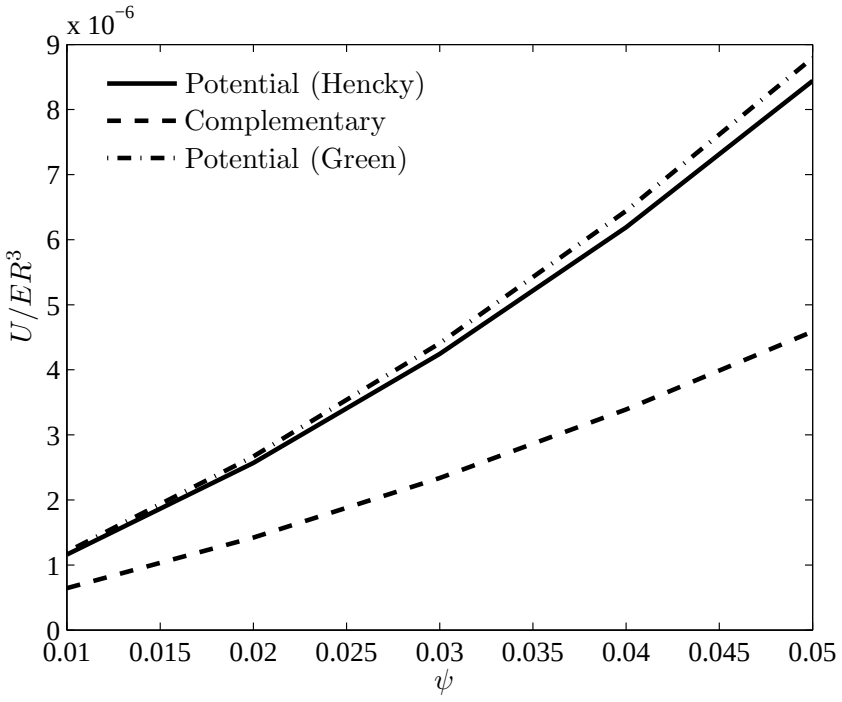

Figure 8.7. Plot of energy versus angle of rotation for non-dimensional work of adhesion $W_{ad}/ER = 10^{-5}$ and non-dimensional thickness $H/R = 0.01$.

Noting that $\mathbf{e}_1 = \cos\theta\mathbf{e}_s - \sin\theta\mathbf{e}_\theta$, $\mathbf{u}_0$ may be expressed as

$$\mathbf{u}_0(s,\theta) = u_1\cos\theta\mathbf{e}_s - u_1\sin\theta\mathbf{e}_\theta + u_3\mathbf{e}_3. \tag{8.57}$$

This implies that Ω is a ruled surface with directrix ∂B. To demonstrate this, consider any line along $\mathbf{e}_s$ that is fixed to Ω_0. Following from the linearity of u_1 and u_3, such a line maps to a ruling on Ω.

Based on the constitutive law and plane stress condition, it should be possible to derive q corresponding to the deformation associated with (8.56). However, for demonstration purposes, it is convenient to prescribe $q = 0$. This additional restriction on $\mathcal{F}$, though kinematically admissible, conflicts with the solution for plane stress and so is likely to reduce the accuracy of the upper bound approximation.

Evaluating $\mathbf{e}_n$ from (8.9) and substituting $\mathbf{u}_0$, $\mathbf{e}_n$, and $q = 0$ into (8.28) yields the

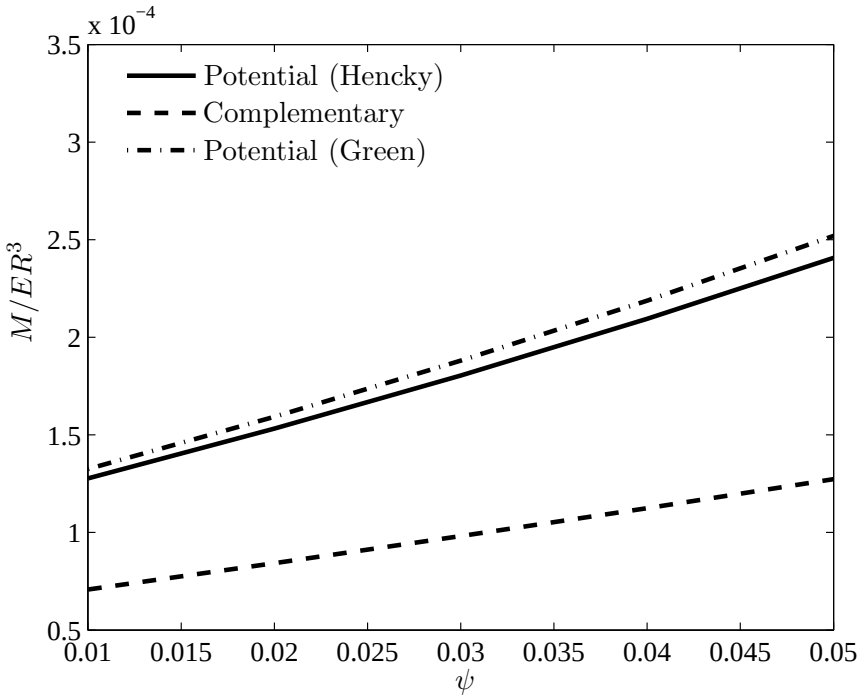

Figure 8.8. Plot of non-dimensional moment M/ER^3 versus angle of rotation for non-dimensional work of adhesion $W_{ad}/ER = 10^{-5}$ and non-dimensional thickness $H/R = 0.01$.

deformation gradient $\mathbf{F}_m$ for points on the midplane. The corresponding strain tensor $\mathbf{E}_m$ is then determined from (8.29) and substituted into (8.23) to determine the strain energy density, W. Lastly, by (8.30),

$$U = \int_0^{2\pi} \int_R^{v(\theta)} W\, H\, s\, ds\, d\theta. \tag{8.58}$$

The potential can also be evaluated for small strains (but large rotations) with Green's strain tensor

$$\mathbf{E}_G = \frac{1}{2}\left(\mathbf{F}^\top \mathbf{F} - \mathbf{I}\right). \tag{8.59}$$

8.4.2 Lower Bound

For the construction of a lower bound, the simplifying assumption of a ruled surface is not needed. Instead, it is assumed that the Piola stress tensor has the form

$$\mathbf{P} = \sigma_s \mathbf{e}_s \otimes \mathbf{e}_s + \sigma_\theta \mathbf{e}_\theta \otimes \mathbf{e}_\theta - \tau \mathbf{e}_s \otimes \mathbf{e}_3. \tag{8.60}$$

The eigenvalues of $\mathbf{P}\mathbf{P}^\top$ are ${\sigma_s}^2 + \tau^2$ and ${\sigma_\theta}^2$. Hence, following the arguments presented in Section 8.2.2, the Biot stresses are

$$t_t = \sqrt{{\sigma_s}^2 + \tau^2} \qquad \text{and} \qquad t_l = \sigma_\theta. \tag{8.61}$$

It is also convenient to let the ratio of t_t to t_l equal Poisson's ratio. Hence, (8.61) implies

$$\sigma_\theta = \frac{\lambda}{2(\lambda+\mu)} \sqrt{{\sigma_s}^2 + \tau^2}. \tag{8.62}$$

As with (8.60), such a condition may conflict with kinematically admissible solutions to the constitutive equations for plane stress. Thus, setting t_t/t_l equal to Poisson's ratio will likely reduce the accuracy of the lower bound approximation for U^*.

At equilibrium, $\operatorname{Div} \mathbf{P} = \mathbf{0}$ (computed as $\operatorname{Div} \mathbf{P} = \bigtriangledown \cdot \mathbf{P}$), which implies

$$\frac{\partial \sigma_s}{\partial s} = \frac{1}{s}(\sigma_\theta - \sigma_s) \qquad \text{and} \qquad \frac{\partial \tau}{\partial s} = -\frac{\tau}{s}. \tag{8.63}$$

Substituting σ_θ with (8.62) and solving,

$$\sigma_s = \frac{1}{4} C_1 s^{-\frac{\lambda+2\mu}{2(\lambda+\mu)}} - \frac{C_2^2}{C_1} s^{-\frac{3\lambda+2\mu}{2(\lambda+\mu)}} \qquad \text{and} \qquad \tau = \frac{C_2}{s}, \tag{8.64}$$

where C_1 and C_2 are constants of integration. These are used to evaluate the Biot stresses, which are then substituted into (8.25) and (8.26) to obtain γ_t and γ_l, respectively. Noting that $\gamma_l = 0$, the expression for strain energy reduces to

$$W = \frac{\lambda + 2\mu}{8\mu(\lambda+\mu)} t_t^2. \tag{8.65}$$

The complementary density is evaluated by substituting t_t, $t_l = \lambda t_t/2(\lambda+\mu)$, γ_t, $\gamma_l = 0$ and W into (8.33), which yields $W_c = w_c(s\,;\,C_1, C_2)$.

For $\theta \in [0, 2\pi]$, the prescribed vectors in (8.31) are $\boldsymbol{N}(v) = \mathbf{e}_s$, $\boldsymbol{\xi}(v) = v\mathbf{e}_s$ $\boldsymbol{N}(R) = -\mathbf{e}_s$, and $\boldsymbol{\xi}(R) \in \mathcal{B}$ such that

$$\boldsymbol{\xi}(R) = R\mathbf{e}_s + R(1-\cos\theta)(1-\cos\psi)\mathbf{e}_1 + R(1-\cos\theta)\sin\psi\mathbf{e}_3. \tag{8.66}$$

Hence, the total complementary energy is

$$\Phi = \int_0^{2\pi} \eta(\theta\,;\,C_1, C_2)\, H\, d\theta, \tag{8.67}$$

where

$$\eta = R^2(1-\cos\theta)[(\tau)_R \sin\psi - (\sigma_s)_R(1-\cos\psi)\cos\theta] + \int_R^v \left[\frac{d}{ds}\left(s^2\sigma_s\right) - sw_c\right] ds. \tag{8.68}$$

A lower bound on the strain energy is obtained by integrating the supremum of ηH over $C_1 \in \mathbb{R}$ and $C_2 \in \mathbb{R}$ at each $\theta \in [0, 2\pi]$:

$$\Phi^{**} = \int_0^{2\pi} \max_{C_1, C_2} \eta H\, d\theta. \tag{8.69}$$

8.4.3 Approximate Solution at Equilibrium

The strain energy density W is approximated by (8.23) evaluated with Green's strain tensor. Integrating WHs over $s \in [R, v]$ in (8.58) yields a functional of the form

$$U = \int_0^{2\pi} h(\theta, v(\theta))\, d\theta, \tag{8.70}$$

where

$$\begin{aligned} h \;=\; & \{H\,R^2\,(-10\,v^4\,\lambda - 24\,v^4\,\mu + 16\,v^3\,\mu\,R + 14\,v^2\,\lambda\,R^2 + 4\,v^2\,\mu\,R^2 + 16\,v\,\mu\,R^3 - 4\,\lambda\,R^4 - 12\,\mu\,R^4 + \\ & 3\,v^4\,\lambda\,\cos(3\,\theta) + 6\,v^4\,\mu\,\cos(3\,\theta) - 3\,v^2\,\lambda\,R^2\,\cos(3\,\theta) - 6\,v^2\,\mu\,R^2\,\cos(3\,\theta) + 4\,v^4\,\lambda\,\ln(v) + \\ & 12\,v^4\,\mu\,\ln(v) + 16\,v^3\,\lambda\,R\,\ln(v) + 24\,v^3\,\mu\,R\,\ln(v) + 12\,v^2\,\lambda\,R^2\,\ln(v) + 28\,v^2\,\mu\,R^2\,\ln(v) - \\ & 2\,v^4\,\lambda\,\cos(3\,\theta)\,\ln(v) - 2\,v^4\,\mu\,\cos(3\,\theta)\,\ln(v) - 4\,v^3\,\lambda\,R\,\cos(3\,\theta)\,\ln(v) - 12\,v^3\,\mu\,R\,\cos(3\,\theta)\,\ln(v) - \end{aligned}$$

$$2\,v^2\,\lambda\,R^2\,\cos(3\,\theta)\,\ln(v) - 2\,v^2\,\mu\,R^2\,\cos(3\,\theta)\,\ln(v) - 4\,v^4\,\lambda\,\ln(R) - 12\,v^4\,\mu\,\ln(R) -$$
$$16\,v^3\,\lambda\,R\,\ln(R) - 24\,v^3\,\mu\,R\,\ln(R) - 12\,v^2\,\lambda\,R^2\,\ln(R) - 28\,v^2\,\mu\,R^2\,\log(R) + 2\,v^4\,\lambda\,\cos(3\,\theta)\,\log(R) +$$
$$2\,v^4\,\mu\,\cos(3\,\theta)\,\ln(R) + 4\,v^3\,\lambda\,R\,\cos(3\,\theta)\,\ln(R) + 12\,v^3\,\mu\,R\,\cos(3\,\theta)\,\ln(R) + 2\,v^2\,\lambda\,R^2\,\cos(3\,\theta)\,\ln(R) +$$
$$2\,v^2\,\mu\,R^2\,\cos(3\,\theta)\,\ln(R) + \cos(\theta)\,(-((v-R)\,(v^3\,(7\,\lambda+26\,\mu) + v^2\,(15\,\lambda+2\,\mu)\,R + 4\,v\,(3\,\lambda+11\,\mu)\,R^2 +$$
$$4\,(\lambda+\mu)\,R^3)) + 2\,v^2\,(v^2\,(\lambda+5\,\mu) + 2\,v\,(\lambda-\mu)\,R + (\lambda+5\,\mu)\,R^2)\,\ln(v) - 2\,v^2\,(v^2\,(\lambda+5\,\mu) +$$
$$2\,v\,(\lambda-\mu)\,R + (\lambda+5\,\mu)\,R^2)\,\ln(R)) - 2\,v\,\cos(2\,\theta)\,(-((v-R)\,(v^2\,(7\,\lambda+10\,\mu) + v\,(11\,\lambda+30\,\mu)\,R +$$
$$4\,(\lambda+\mu)\,R^2)) + 2\,v\,(v^2\,(\lambda+\mu) + 2\,v\,(2\,\lambda+5\,\mu)\,R + (3\,\lambda+5\,\mu)\,R^2)\,\log(v) - 2\,v\,(v^2\,(\lambda+\mu) +$$
$$2\,v\,(2\,\lambda+5\,\mu)\,R + (3\,\lambda+5\,\mu)\,R^2)\,\ln(R)))\,\sin(\theta/2)^2\,\sin(\psi/2)^4\}/\{2\,(v-R)^4\}.$$

The work required to create new surface is given by

$$W_s = \int_0^{2\pi}\int_R^{v(\theta)} W_{ad}\,s\,ds\,d\theta. \tag{8.71}$$

Thus, the total energy of the system is

$$E = U + W_s = \int_0^{2\pi}\left\{h + \frac{v^2-R^2}{2}W_{ad}\right\}\,d\theta. \tag{8.72}$$

By the Griffith energy balance, E is stationary at equilibrium. Hence the integrand of E satisfies the Euler-Lagrange differential equation, which implies

$$\frac{\partial h}{\partial v} + vW_{ad} = 0. \tag{8.73}$$

Substituting the expression for h, (8.73) may be expressed as

$$\begin{aligned}
0 \;=\;& v\,W_{\mathrm{ad}}\,(v-R)^5 + H\,R^2\,(2\,v^4\,\lambda + 6\,v^4\,\mu + 26\,v^3\,\lambda\,R + 46\,v^3\,\mu\,R - 16\,v^2\,\lambda\,R^2 - 26\,v^2\,\mu\,R^2 - 20\,v\,\lambda\,R^3 - \\
& 42\,v\,\mu\,R^3 + 8\,\lambda\,R^4 + 16\,\mu\,R^4 - v^4\,\lambda\,\cos(3\,\theta) - v^4\,\mu\,\cos(3\,\theta) - 7\,v^3\,\lambda\,R\,\cos(3\,\theta) - 17\,v^3\,\mu\,R\,\cos(3\,\theta) + \\
& 4\,v^2\,\lambda\,R^2\,\cos(3\,\theta) + 11\,v^2\,\mu\,R^2\,\cos(3\,\theta) + 4\,v\,\lambda\,R^3\,\cos(3\,\theta) + 7\,v\,\mu\,R^3\,\cos(3\,\theta) - 16\,v^3\,\lambda\,R\,\ln(v) - \\
& 36\,v^3\,\mu\,R\,\ln(v) - 36\,v^2\,\lambda\,R^2\,\ln(v) - 64\,v^2\,\mu\,R^2\,\ln(v) - 12\,v\,\lambda\,R^3\,\ln(v) - 28\,v\,\mu\,R^3\,\ln(v) + \\
& 6\,v^3\,\lambda\,R\,\cos(3\,\theta)\,\ln(v) + 10\,v^3\,\mu\,R\,\cos(3\,\theta)\,\ln(v) + 8\,v^2\,\lambda\,R^2\,\cos(3\,\theta)\,\ln(v) + 20\,v^2\,\mu\,R^2\,\cos(3\,\theta)\,\ln(v) + \\
& 2\,v\,\lambda\,R^3\,\cos(3\,\theta)\,\ln(v) + 2\,v\,\mu\,R^3\,\cos(3\,\theta)\,\ln(v) + 16\,v^3\,\lambda\,R\,\ln(R) + 36\,v^3\,\mu\,R\,\ln(R) + 36\,v^2\,\lambda\,R^2\,\ln(R) + \\
& 64\,v^2\,\mu\,R^2\,\ln(R) + 12\,v\,\lambda\,R^3\,\ln(R) + 28\,v\,\mu\,R^3\,\ln(R) - 6\,v^3\,\lambda\,R\,\cos(3\,\theta)\,\ln(R) - 10\,v^3\,\mu\,R\,\cos(3\,\theta)\,\ln(R) - \\
& 8\,v^2\,\lambda\,R^2\,\cos(3\,\theta)\,\ln(R) - 20\,v^2\,\mu\,R^2\,\cos(3\,\theta)\,\ln(R) - 2\,v\,\lambda\,R^3\,\cos(3\,\theta)\,\ln(R) - 2\,v\,\mu\,R^3\,\cos(3\,\theta)\,\ln(R) + \\
& \cos(\theta)\,((v-R)\,(v^3\,(\lambda+5\,\mu) + v\,(28\,\lambda+51\,\mu)\,R^2 + 4\,(3\,\lambda+7\,\mu)\,R^3 + v^2\,(20\,\lambda\,R+38\,\mu\,R)) - \\
& 2\,v\,R\,(3\,v^2\,(\lambda+3\,\mu) + 2\,v\,(2\,\lambda+\mu)\,R + (\lambda+5\,\mu)\,R^2)\,\ln(v) + 2\,v\,R\,(3\,v^2\,(\lambda+3\,\mu) + 2\,v\,(2\,\lambda+\mu)\,R +
\end{aligned}$$

$(\lambda + 5\,\mu)\,R^2)\,\ln(R)) - 2\,\cos(2\,\theta)\,((v - R)\,(v^3\,(\lambda + \mu) + 20\,v^2\,(\lambda + 2\,\mu)\,R + 3\,v\,(6\,\lambda + 13\,\mu)\,R^2 + 2\,(\lambda + \mu)\,R^3) - 2\,v\,R\,(v^2\,(4\,\lambda + 7\,\mu) + v\,(9\,\lambda + 20\,\mu)\,R + (3\,\lambda + 5\,\mu)\,R^2)\,\ln(v) + 2\,v\,R\,(v^2\,(4\,\lambda + 7\,\mu) + v\,(9\,\lambda + 20\,\mu)\,R + (3\,\lambda + 5\,\mu)\,R^2)\,\ln(R)))\,\sin(\theta/2)^2\,\sin(\psi/2)^4.$

Solving (8.73) yields the approximate shape $v^{**} = v^{**}(\theta)$ of the delamination zone at equilibrium. Substituting this solution into (8.56) leads to the deformed configuration of the membrane for a prescribed angle of rotation, ψ. The corresponding strain energy is

$$U^{**} = \int_0^{2\pi} h(\theta, v^{**}(\theta))\,d\theta. \tag{8.74}$$

Following the arguments in Section 8.2.4, U^{**} is an upper bound approximation of the strain energy U^* at equilibrium.

8.5 Numerical Results and Discussion

The boundary value problem formed by the differential equations (8.47) and boundary conditions (8.48, 8.54) are solved in Matlab 7.0 (The Mathworks, Inc. 2004) using a finite difference method. The initial guess for functions $u_s(s)$ and $u_3(s)$ are

$$(u_s)_{init} = 0 \qquad \text{and} \qquad (u_3)_{init} = \Delta(v - s). \tag{8.75}$$

Figure 8.3 is a side-view (not to scale) of the membrane for $W_{ad}/ER = 10^{-5}$, where $E = (3\lambda\mu+2\mu^2)/(\lambda+\mu)$ is the elastic modulus, $H/R = 0.01$, and Poisson's ratio $\lambda/2(\lambda+\mu) = 0.4$. The difference between the shaft and delamination zone radii is observed to increase nearly linearly with shaft height. The load necessary to achieve a prescribed height is obtained by evaluating

$$P = \frac{dU}{d\Delta}. \tag{8.76}$$

(see Figure 8.4).

Numerical results for the case of shaft rotation are presented in Figures 8.6-8.8. Again, $W_{ad}/ER = 10^{-5}$, $H/R = 0.01$, and $\lambda/2(\lambda + \mu) = 0.4$. An algebraic expression for (8.73) is obtained with the aid of Mathematica 4 (Wolfram Research, Inc. 2000) and is solved for $v = v(\theta)$ by using a scalar root finder in Matlab (see Figure 8.6). Equation (8.73) is derived from Green's strain tensor (8.59), which is a small strain approximation of the Hencky strain (8.14). For the geometries considered here, both strain tensors yield similar upper bounds for the elastic strain energies, as demonstrated in Figure 8.7. Hencky strain is also used to approximate the maximum complementary energy, which furnishes a lower bound on the elastic energy. The tightness of these bounds indicate the accuracy of the solution for $v(\theta)$. Evaluating the derivative of the energy approximations with respect to ψ yields the moment necessary to achieve a prescribed angle of rotation, i.e.

$$M = \frac{dU}{d\psi}. \tag{8.77}$$

(see Figure 8.8).

8.5.1 Examples

Consider a synthetic setal stalk of length $L = 100$ μm and radius $R = 3$ μm supporting a membrane of thickness $H = 30$ nm. Assume an elastic modulus $E = 1$ GPa, a work of adhesion $W_{\text{ad}} = 30$ mJ/m^2, and Poisson's ratio $\nu = 0.4$. Following from (5.12) and (5.46), such fibers must be spaced at least 1.6 microns apart in order to avoid clumping. Hence, for an array with maximal fiber density, the membrane radius is limited to

$$R_m := R + \frac{1.6\mu m}{2} = 3.8\mu m \approx 1.3R. \tag{8.78}$$

The non-dimensional thickness and work of adhesion are $H/R = 0.01$ and $W_{\rm ad}/ER = 10^{-5}$, respectively.

From Figure 8.4 it follows that the normal resistance is approximately

$$P \approx 4.255ER\Delta + 1.2ER^2. \tag{8.79}$$

However, Figure 8.3 implies that Δ/R cannot exceed 0.1, since $R_m = 1.3$ R and the radius of the delamination zone is limited by the membrane radius. Therefore, each membrane will have a bond strength of roughly $1.6ER^2 = 14$ mN and a tensile compliance of $\Delta = 0.1$R $=$ 300 nm. This bond strength far exceeds the estimate $1.5\pi W_{\rm ad}R = 420$ nN obtained from JKR theory for a rounded tip. Moreover, it exceeds the shear strength of the membrane, which is calculated as the cross-sectional area $2\pi RH$ multiplied by the bulk shear strength $\gamma \sim 0.1E$. For $R = 3$ μm, $H = 30$ nm, and $E = 1$ GPa, the maximum pull-off force before shear failure in the membrane is approximately 60 μN. According to (5.45), an outerwall spacing of 1.6 μm implies a density $D = 1.7 \times 10^6$ cm^{-2}. Hence, the estimated bond strength will be close to 100 N/cm^2 for contact with a surface of roughness on the order of several hundred nanometers.

The detachment resistance under a shear load V will also be significant. Assuming clamped-clamped loading on each fiber, the moment acting on the membrane-substrate interface will be approximately $M = VL/2$. Solving for V yields $V = 2M/L$. According to the results plotted in Figure 8.8, M is on the order of ER^3. Thus,

$$V \approx \frac{2ER^3}{L} = 0.54mN \tag{8.80}$$

This estimate is well below the bulk shear strength of the fiber, which would be $\pi R^2\gamma \approx 3mN$, suggesting that bond failure would be caused by membrane delamination For a density $D = 0.7 \times 10^6$, the shear resistance will be close to 400 N/cm^2.

8.6 Concluding Remarks

As demonstrated with the examples presented in Section 8.5.1, terminal membranes increase bond strength by several orders of magnitude. Such a design is attractive for applications requiring permanent normal and shear adhesion.

Membrane-controlled adhesion requires thin spatulae of nanoscale thickness. Such spatulae have negligible bending stiffness and thus can easily conform to microrough surfaces. Microfiber arrays with larger, microscale membranes have been successfully fabricated by [31]. In this embodiment, the larger thickness (2 μm) is compensated for by a larger membrane radius (20 μm) and smaller elastic modulus (3 MPa). The bond strength was measured to be 1 N/cm^2, a little over twice as large as the unstructured control.

New fabrication methods must be developed in order to realize the structures presented in Section 8.5.1. One technique is to intentionally "overfill" a polycarbonate array during casting. Currently, this results in a layer of polymer that is several hundred nanometers thick. Preliminary measurements show significant shear strength, on the order of 1 kPa, but far from the large values predicted above for an array of independent membranes. The bond strength can be enhanced by reducing the thickness of the overfill layer or by slicing the layer into individual spatulae, each supported by a single fiber.

Part IV

Conclusion

Chapter 9

Conclusion

The purpose of this work is to develop biologically-inspired fiber arrays for enhanced friction and adhesion.

9.1 Overview of Contributions

Design principles are aided by insights into the mechanics of the natural setal array that are introduced in Part II. These design principles are further developed in Part III, which presents theoretical models, fabrication methods, and experimental results for synthetic fiber arrays.

9.1.1 Natural Setal Arrays

In Chapters 3 and 4, elastic rod theory is used to study the bending of natural gecko setae. This yields predictions for fiber and array stiffness that are consistent with experimental measurements performed by colleagues in biology. It is demonstrated that under normal loading, a natural setal array satisfies Dahlquist's criteria for pressure sensitive ad-

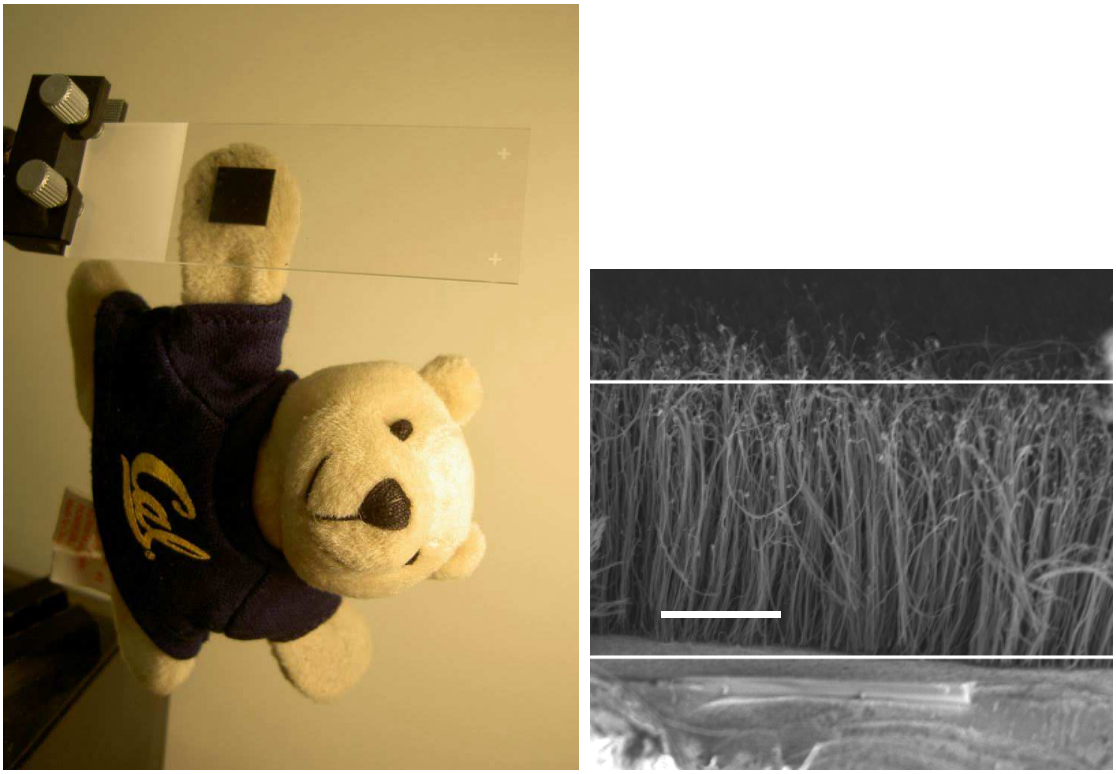

Figure 9.1. Shear adhesion with a MWCNT array [83]; scale bar equals 2 μm.

hesion. This is in spite of being composed of stiff, non-tacky materials that have an elastic modulus $E = 1.5$ GPa.

9.1.2 Side Contact with VANF Arrays

Elastic rod theory is extended to synthetic setae to study adhesion through side contact (Chapter 5). Experimentally, the greatest amount of adhesion is obtained with vertically aligned multi-walled carbon nanotubes (Figure 9.1) [83]. However, adhesion through side contact relies on high density, which leads to fiber clumping after several loading cycles. As shown in Figure 5.5, significant adhesion with non-clumping fibers in side contact is only predicted for a restricted part of the design space. While such structures could be reusable, they are limited to nanometer scale geometries and 1 GPa modulus materials.

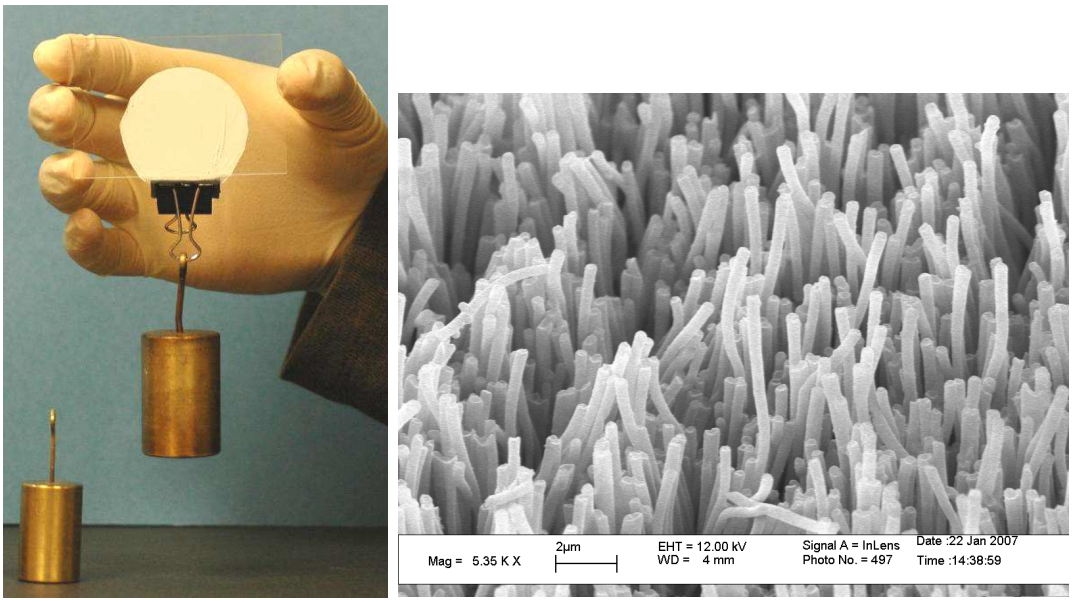

Figure 9.2. An array of 20 μm long, 200 nm diameter polypropylene nanofibers suspending a 200 gram weight in pure shear [69].

9.1.3 Ultrahigh Friction with Microfiber Arrays

A more promising design that admits a wider range of materials and geometries are the microfiber arrays studied in Chapter 6. The coefficient of friction (c.o.f.) increases by over a factor of 30 by molding polypropylene into vertically aligned microfibers. Theory and experiment demonstrate that these microstructured surfaces follow an Amonton's friction law and have a fixed c.o.f. that easily exceeds 10 for certain geometries.

A major barrier to pure shear adhesion is the natural curvature of the array backing. According to Kendall adhesion theory, a thin plate will spontaneously delaminate from a substrate if its natural radius of curvature is below a critical value

$$\rho_{\rm cr} = \sqrt{\frac{Et^3}{24W_{\rm ad}}}, \tag{9.1}$$

where t is the plate thickness, E is the elastic modulus, and $W_{\rm ad}$ is the interfacial work of

adhesion [46] [69]. Hence, in order for the array backing to remain flat, W_{ad} must be large and t should be small.

Empirically, it is found that flattening occurs for $t < 10\mu$m. The contact area is further increased by gently rubbing the sample against this glass, which produces triboelectric charging and thus increases W_{ad}. Triboelectric charging also creates a light electrostatic force that presses the sample into the glass. Because of the high coefficient of friction, this modest pressure is transformed into a large sliding resistance. In this way, a 15 cm^2 array of 20 μm long, 200 nm diameter polypropylene fibers is capable of supporting a 200 gram brass weight in pure shear (Figure 9.2).

9.1.4 Shear Adhesion with Curved Microfibers

While the result presented in Figure 9.2 is impressive, a future aim for synthetic gecko adhesion is to obtain pure shear adhesion through van der Waals forces alone. As demonstrated in Figure 7.9(bottom) this is theoretically possible with an array of curved microfibers. Even for surfaces with roughness on the order of 1 μm, shear adhesion can be as great as 1 N/cm^2.

Fibers may be naturally curved or curved under a shear force. For the latter structures, adhesion would depend on *shear-activation*. This property is an important feature of natural setal arrays and enables the adhesive to be controllable (in order to avoid inadvertent sticking). Shear-activated shear adhesion may also explain the significant bond strength demonstrated with the 200 nm polypropylene fibers, although further testing will be required to determine its role.

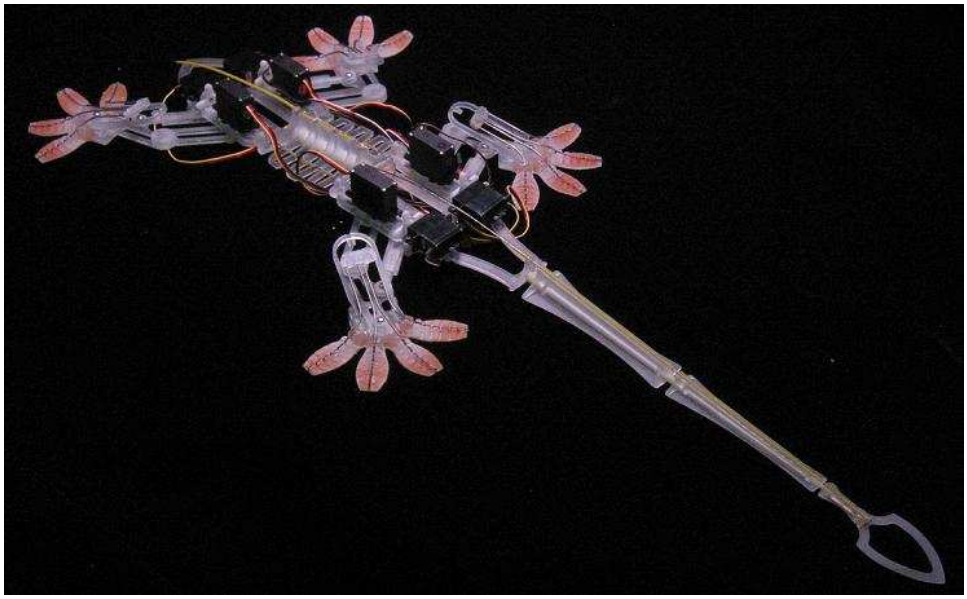

Figure 9.3. Stickybot robot developed at Stanford University [6].

9.1.5 Permanent Adhesion with Spatulae

According to the theory presented in Chapter 8, the greatest amount of adhesion is predicted with an array of axisymmetric nanometer thin membranes. These membranes represent synthetic versions of gecko spatulae. Unlike spatular plates, however, they are supported at their center. Analysis utilizes a novel application of the principles of minimum potential energy and maximum complementary energy in specializing finite elasticity to various modes of membrane delamination.

9.2 Applications

The most immediate application of synthetic setal arrays is for wall climbing robots. Examples include hexapod legged robots developed through the Defense Advanced Research Projects Agency (DARPA) Biodynotics Program. These robots, collectively known as RiSE

(Robots in Scansorial Environments), are designed for robust mobility on both horizontal and vertical terrains [71]. Environments range from smooth surfaces such as glass to curved or rough surfaces like rocks, boulders and trees. Another robot that utilizes synthetic setal arrays for wall climbing is Stickybot, which is being developed by the Biomimetics Dextrous Manipulation Laboratory at Stanford University [6]. Stickybot, shown in Figure 9.3, is designed to achieve *controllable* adhesion through [1]hierarchical compliance, [2]anisotropic friction and adhesion, and [3]distributed force control, similar to the natural gecko [49].

There has been recent interest in synthetic gecko adhesion for manufacturing. Specifically, fiber arrays would form temporary bonds to help mount parts for processing or assembly. Applications range from automobiles to electronic devices. Presently, manufacturers use glues, welding, or soldering to form temporary or weak permanent bonds. These methods consume material and time (for curing or cooling), require high precision (since they do not permit realignment after a bond is formed), and often require multiple tools to execute. By adopting synthetic gecko adhesives, manufacturers hope to avoid these costly issues.

High-friction microfiber arrays could also be used for enhanced traction in shoes, sporting equipment, or automobiles. Unlike rubber, which is naturally sticky, microfiber arrays can be designed to exhibit high friction but negligible adhesion and hence allow for rapid or explosive motions without dissipating energy to overcome inadvertent stiction. In addition to energy losses, adhesion also leads to wear. This is of particular concern in brakes and tires, which otherwise depend on high traction.

Future work in fiber array friction and adhesion will address household and office products as well as biomedical applications. Consider, for example, a residue-free, reusable

sticky tape made with synthetic setal arrays. Such a product might replace pressure sensitive adhesives (PSAs) in applications ranging from stationery to surgical bandages.

9.3 Future Work

Near term work on synthetic setal arrays will continue to focus on adhesion with intrinsically stiff ($E \sim 1$ GPa) materials. Immediate efforts will concentrate on the shear strength of microfibers array with natural or shear-induced curvature. Such structures will be fabricated on a thin ($t < 10\mu$m) backing in order to enhance real contact area.

Future structures will include arrays of hierarchical, synthetic setae supporting either an array of nanofibers or a center-supported spatular membrane. Such structures will exhibit both shear and normal adhesion. In order to achieve these goals, new fabrication techniques will need to be introduced.

Longer term efforts will work towards integrating synthetic gecko adhesives into applications for manufacturing, medicine, and household products. Certain integration processes may preclude array fabrication through polymer casting. In such cases, new materials and fabrication techniques may need to be introduced. These include chemical or fluidic self-assembly, electro-deposition, or chemical vapor deposition.

Future work might also be aimed at establishing new interfacial laws and theoretical models to address the unique and remarkable properties of fiber arrays surfaces. These include modifications to Coulomb's friction law and a reassessment of interfacial work of adhesion. New insights into the friction and adhesion of fiber arrays may indeed be motivated by theoretical work. Such attention, however, will only be generated by early experi-

mental or commercial successes that justify the viability of synthetic gecko adhesives as an important, established technology.

References

[1] L. Anand. Hencky, H. Approximate Strain-Energy Function for Moderate Deformations. *Journal of Applied Mechanics*, 46:78–82, 1979.

[2] L. Anand. Moderate Deformations in Extension Torsion of Incompressible Isotropic Elastic-Materials. *Journal of the Mechanics and Physics of Solids*, 34:293–304, 1986.

[3] S. H. Anastasiadis and S. G. Hatzikiriakos. The work of adhesion of polymer/wall interfaces and its association with the onset of wall slip. *Journal of Rheology*, 42:795–812, 1998.

[4] K. Autumn. Properties, Principles, and Parameters of the Gecko Adhesive System. In A. Smith and J. Callow, editors, *Biological Adhesives*, pages 225–255, Berlin, 2006. Springer-Verlag.

[5] K. Autumn. How Gecko Toes Stick. *American Scientist*, 24:124–132, Mar-Apr 2006.

[6] K. Autumn, A. Dittmore, D. Santos, M. Spenko, and M. Cutkosky. Frictional adhesion: a new angle on gecko attachment. *Journal of Experimental Biology*, 209:3569–3579, 2006.

[7] K. Autumn, Y. A. Liang, S. T. Hsieh, W. Zesch, W. P. Chan, T. W. Kenny, R. Fearing, and R. J. Full. Adhesive force of a single gecko foot-hair. *Nature*, 405:681–684, 2000.

[8] K. Autumn, C. Majidi, R. E. Groff, A. Dittmore, and R. S. Fearing. Effective Elastic Modulus of Isolated Gecko Setal Arrays. *Journal of Experimental Biology*, 209:3558–3568, 2006.

[9] K. Autumn and A. Peattie. Mechanisms of adhesion in geckos. *Integrative and Comparative Biology*, 42:1081–1090, 2002.

[10] K. Autumn, M. Sitti, Y. A. Liang, A. M. Peattie, W. R. Hansen, S. Sponberg, T. W. Kenny, R. Fearing, J. N. Israelachvili, and R. J. Full. Evidence for van der Waals adhesion in gecko setae. *Proceedings of the National Academy of Science*, 99:12252–12256, 2002.

[11] A. Bertram. *Elasticity and Plasticity of Large Deformations*. Springer, 2005.

[12] B. Bhushan. *Introduction to Tribology*. John Wiley & Sons, Inc., 2002.

[13] N. Bloch and D. J. Irschick. Toe-clipping dramatically reduces clinging performance in a pad-bearing lizard (Anolis carolinensis). *Journal of Herpetology*, 37:293–298, 2005.

[14] R. H. C. Bonser. The Young's modulus of ostrich claw keratin. *Journal of Materials Science Letters*, 19:1039–1040, 2000.

[15] R. H. C. Bonser and P. P. Purslow. The Young's Modulus of Feather Keratin. *Journal of Experimental Biology*, 198:1029–1033, 1995.

[16] G. Carbone, L. Mangialardi, and B. N. J. Persson. Adhesion between a thin elastic plate and a hard randomly rough substrate. *Physical Review B*, 70:125407, 2004.

[17] R. W. Carpick, N. Agrait, D. F. Ogletree, and M. Salmeron. Variation of the interfacial shear strength and adhesion of a nanometer-sized contact. *Langmuir*, 12:3334–3340, 1996.

[18] M. K. Chaudhury, T. Weaver, C.-Y. Hui, and E. J. Kramer. Adhesive contact of cylindrical lens and a flat sheet. *J. App. Phys.*, 80:30, 1996.

[19] P. L. Dickrell, S. B. Sinnott, D. W. Hahn, N. R. Raravikar, L. S. Schadler, P. M. Ajayan, and W. G. Sawyer. Frictional anisotropy of oriented carbon nanotube surfaces. *Tribology Letters*, 18:59, 2005.

[20] R. Dubrow. Structures, systems and methods for joining articles and materials and uses therefor. *US Patent 7,056,409 B2*, 2006.

[21] F. M. Fowkes. Attractive Forces at Interfaces. *Industrial and Engineering Chemistry*, 56:40–52, 1964.

[22] R. Frisch-Fay. *Flexible Bars*. Butterworths, Washington, D.C., 1962.

[23] D. Y. Gao. *Duality Principles in Nonconvex Systems*. Kluwer, 2000.

[24] H. J. Gao, X. Wang, H. M. Yao, S. Gorb, and E. Arzt. Mechanics of hierarchical adhesion structures of geckos. *Mechanics of Materials*, 37:275–285, 2005.

[25] H. J. Gao and H. M. Yao. Shape insensitive optimal adhesion of nanoscale fibrillar structures. *Proceedings of the National Academy of Sciences*, 101:7851–7856, 2004.

[26] A. K. Geim, S. V. Dubunos, I. V. Grigorieva, K. S. Novoselov, A. A. Zhukov, and Y. U. Shapoval. Microfabricated adhesive mimicking gecko foot-hair. *Nature Materials*, 2:461–463, 2003.

[27] W. W. Gerberich and M. J. Cordill. Physics of Adhesion. *Reports on Progress in Physics*, 69:2157–2203, 2006.

[28] J. M. Gere and S. P. Timoshenko. *Mechanics of Materials*. PWS-Kent, Boston, second edition, 1984.

[29] A. Ghatak, L. Mahadevan, J. Y. Chung, M. K. Chaudhury, and V. Shenoy. Peeling from a biomimetically patterned thin elastic film. *Proceedings of the Royal Society A*, 460:2725–2735, 2004.

[30] N. J. Glassmaker, A. Jagota, C.-Y. Hui, and J. Kim. Design of biomimetic fibrillar interfaces: 1. Making contact. *Journal of the Royal Society Interface*, 1:1–11, 2004.

[31] S. Gorb, M. Varenberg, A. Peressadko, and J. Tuma. Biomimetic mushroom-shaped fibrillar adhesive microstructure. *Journal of the Royal Society Interface*, 2006.

[32] D. H. Gracias and G. A. Somorgai. Continuum force microscopy study of the elastic modulus, hardness and friction of polyethylene and polypropylene surfaces. *Macromolecules*, 31:1269, 1998.

[33] M. E. Gurtin. The Nature of Configurational Forces. *Archive for Rational Mechanics and Analysis*, 131:67–100, 1995.

[34] J. B. Haddow, L. Favre, and R. W. Ogden. Application of variational principles to the axial extension of a circular cylindrical nonlinearly elastic membrane. *Journal of Engineering Mathematics*, 37:65–84, 2000.

[35] W. R. Hansen and K. Autumn. Evidence for self-cleaning in gecko setae. *Proceedings of the National Academy of Sciences*, 102:385–389, 2005.

[36] G. Huber, S. N. Gorb, R. Spolenak, and E. Arzt. Resolving the nanoscale adhesion of individual gecko spatulae by atomic force microscopy. *Biology Letters*, 1:2–4, 2005.

[37] G. Huber, H. Mantz, R. Spolenak, K. Mecke, K. Jacovs, S. N. Gorb, and E. Arzt. Evidence for capillarity contributions to gecko adhesion from single spatula nanomechanical measurements. *Proceedings of the National Academy of Sciences*, 102:16293–16296, 2005.

[38] C.-Y. Hui, N. J. Glassmaker, T. Tang, and A. Jagota. Design of biomimetic fibrillar interfaces: 2. Mechanics of enhanced adhesion. *Journal of the Royal Society Interface*, 1:12–26, 2004.

[39] D. J. Irschick, C. C. Austin, K. Petren, R. N. Fisher, J. B. Losos, and O. Ellers. A comparative analysis of clinging ability among pad-bearing lizards. *Biological Journal of the Linnean Society*, 59:21–35, 1996.

[40] D. J. Irschick, A. Herrel, and B. Vanhooydonck. Whole-organism studies of adhesion in pad-bearing lizards: creative evolutionary solutions to functional problems. *Journal of Comparative Physiology A*, 192:1169–1177, 2006.

[41] J. N. Israelachvili. *Intermolecular and Surface Forces*. Academic Press, San Diego, California, second edition, 1992.

[42] A. Jagota and S. J. Bennison. Mechanics of adhesion through a fibrillar microstructure. *Integrative and Comparative Biology*, 42:1140–1145, 2002.

[43] K. L. Johnson. Adhesion and friction between a smooth elastic spherical asperity and a plane surface. *Proceedings of the Royal Society of London A*, 453:163–179, 1997.

[44] K. L. Johnson, K. Kendall, and A. D. Roberts. Surface Energy and the Contact of Elastic Solids. *Proceedings of the Royal Society of London A*, 324:301–313, 1971.

[45] J. Kahn. Nano's Big Future. *National Geographic*, 209:98–119, 2006.

[46] K. Kendall. Adhesion and Surface Energy of Elastic Solids. *Journal of Physics D*, 4:1186–1195, 1971.

[47] H. Kinoshita, I. Kumme, M. Tagawa, and N. Ohmae. High friction of a vertically aligned carbon-nanotube film in microtribology. *Applied Physics Letters*, 85:2780, 2004.

[48] W. T. Koiter. On the complementary energy theorem in non-linear elasticity theory. *Trends in Applications of Pure Mathematics to Mechanics*, 1:207–232, 1976.

[49] Biomimetics Dextrous Manipulation Laboratory. Whole Body Adhesion: Hierarchical, Directional & Distributed Control of Climbing Forces. San Antonio, Texas, 2006. SWRI.

[50] C. Lanczos. *The Variational Principles of Mechanics*. Dover, New York, fourth edition, 1970.

[51] S. Liu, J. B. Haddow, and S. Dost. A Variational Approach to a Circular Hyperelastic Membrane Problem. *Acta Mechanica*, 99:191–200, 1993.

[52] C. Majidi. Remarks on formulating an adhesion problem using Euler's elastica. *Mechanics Research Communications*, 34:85–90, 2007.

[53] C. Majidi, R. E. Groff, and R. S. Fearing. Clumping and Packing of Hair Arrays Manufactured by Nanocasting. *Proceedings of the ASME IMECE, Anaheim, California*, page 62142, 2004.

[54] C. Majidi, R. E. Groff, and R. S. Fearing. Attachment of fiber array adhesive through side contact. *Journal of Applied Physics*, 98:103521, 2005.

[55] C. Majidi, R. E. Groff, and R. S. Fearing. Analysis of Shaft-Loaded Membrane Delamination Using Stationary Principles. *Mathematics and Mechanics of Solids*, 2007.

[56] C. Majidi, R. E. Groff, Y. Maeno, B. Schubert, S. Baek, B. Bush, R. Maboudian, N. Gravish, M. Wilkinson, K. Autumn, and R. S. Fearing. High Friction from a Stiff Polymer Using Microfiber Arrays. *Physical Review Letters*, 97:076103, 2006.

[57] M. T. Northen and K. L. Turner. A batch fabricated biomimetic dry adhesive. *Nanotechnology*, 16:1159–1166, 2005.

[58] R. W. Ogden. *Non-linear Elastic Deformations*. Ellis Horwood, 1984.

[59] A. M. Peattie, C. Majidi, A. Corder, and R. J. Full. Ancestrally High Elastic Modulus of Gecko Setal β-keratin. *Journal of the Royal Society Interface*, accepted, 2007.

[60] B. N. J. Persson. On the mechanism of adhesion in biological systems. *Journal of Chemical Physics*, 118:7614–7620, 2003.

[61] B. N. J. Persson and S. Gorb. The effect of surface roughness on the adhesion of elastic plates with application to biological systems. *Journal of Chemical Physics*, 119:11437–11444, 2003.

[62] R. H. Plaut, A. J. Dalrymple, and D. A. Dillard. Effect of work of adhesion on contact of an elastica with a flat surface. *Journal of Adhesion Science and Technology*, 15:565–581, 2001.

[63] R. H. Plaut, N. L. Williams, and D. A. Dillard. Elastic analysis of the loop tack test for pressure sensitive adhesives. *Journal of Adhesion*, 76:37–53, 2001.

[64] A. V. Pocius. *Adhesion and Adhesives Technology*. Hanser, second edition, 2002.

[65] C. M. Pooley and D. Tabor. Friction and Molecular Structure: Behavior of Some Thermoplastics. *Proceedings of the Royal Society of London A*, 329:251, 1972.

[66] E. Rabinowicz. *Friction and Wear of Materials*. John Wiley and Sons, second edition, 1995.

[67] Back Scatter. High-friction microfibers. *Physics Today*, 59:116, 2006.

[68] H. H. Schleich and W. Kastle. Ultrastructure of gekkonid toe pads (Reptilia: Sauria: Gekkonidae). *Amphibia-Reptilia*, 7:141–166, 1986.

[69] B. Schuber, C. Majidi, R. E. Groff, S. Baek, B. Bush, R. Maboudian, and R. S. Fearing. Towards friction and adhesion from high modulus microfiber arrays. *Journal of Adhesion Science and Technology*, submitted, 2007.

[70] M. Sitti and R. S. Fearing. Synthetic gecko foot-hair micro/nano-structures as dry adhesives. *Journal of Adhesion Science and Technology*, 18:1055–1074, 2003.

[71] M. Spenko, M. Cutkosky, C. Majidi, R. S. Fearing, R. E. Groff, and K. Autumn. Foot Design and Integration for Bioinspired Climbing Robots. *Proceedings of SPIE, Unmanned Systems Tech. VIII*, 6230:623019, 2006.

[72] R. Spolenak, S. Gorb, and E. Arzt. Adhesion design maps for bio-inspired attachment systems. *Acta Biomateriala*, 1:5–13, 2005.

[73] R. Spolenak, S. Gorb, H. Gao, and E. Arzt. Effects of contact shape on the scaling of biological attachments. *Proceedings of the Royal Society A*, 461:305–319, 2005.

[74] D. J. Steigmann. Puncturing a thin elastic sheet. *International Journal of Non-linear Mechanics*, 40:255–270, 2005.

[75] S. P. Timoshenko and J. M. Gere. *Theory of Elastic Stability*. McGraw-Hill, New York, second edition, 1961.

[76] Y.-C. Tsai, W.-P. Shih, Y.-M. Wang, L.-S. Huang, and P.-J. Shih. E-Beam Photoresist and Carbon Nanotubes as Biomimetic Dry Adhesives. *Proceedings of IEEE International Conference on MEMS, Istanbul, Turkey*, 2006.

[77] R. Valid. *The Nonlinear Theory of Shells through Variational Principles*. Wiley, 1995.

[78] B. Vanhooydonck, A. Herrel, and D. J. Irschick. Out on a limb: the differential effect of substrate diameter on acceleration capacity in Anolis lizards. *Journal of Experimental Biology*, 209:4515–4523, 2006.

[79] J. G. Williams. Energy release rates for the peeling of flexible membranes and the analysis of blister tests. *International Journal of Fracture*, 87:265–288, 1997.

[80] H. Yao and H. Gao. Mechanics of robust and releasable adhesion in biology: Bottom-up designed hierarchical structures of gecko. *Journal of the Mechanics and Physics of Solids*, 54:1120–1146, 2006.

[81] M. F. Yu, T. Kowaleski, and R. S. Ruoff. Structural analysis of collapsed, and twisted and collapsed, multiwalled carbon nanotubes by atomic force microscopy. *Physical Review Letters*, 86:87, 2001.

[82] B. Yurdumakan, N. R. Raravikar, and P. M. Ajayan. Synthetic gecko foot-hairs from multiwalled carbon nanotubes. *Chemical Communications*, page 3799, 2005.

[83] Y. Zhao, T. Tong, L. Delzet, A. Kashani, and M. Meyyappan. Interfacial energy and strength of multiwalled-carbon-nanotube-based dry adhesive. *Journal of Vacuum Science and Technology B*, 24:331, 2006.